Proton Extraction from a High Energy Beam with Bent Crystals

Jukka Klem

CERN, SL division
CH-1211 Geneva, Switzerland

and

Helsinki Institute of Physics
P.O. Box 9, FIN-00014 University of Helsinki, Finland

Dissertation for the degree of Doctor of Technology to be presented with due permission for public examination and debate in Auditorium F1 at Helsinki University of Technology (Espoo, Finland) on the 24th of August, 1998, at 12 o'clock noon.

Helsinki 1998

Abstract

Extraction with a bent crystal seems to be the only feasible option for providing the possibility for a fixed-target facility at future high-energy hadron colliders such as the LHC. If the extraction set-up is carefully designed and integrated with the beam cleaning system, a crystal could be used in a parasitic mode, i.e. without disturbing the collider experiments and using only particles that would be lost otherwise.

Crystal assisted extraction has been studied at the CERN SPS. Different crystal designs and beam excitation methods have been used. Extraction efficiencies above 15% have been measured. The existence and importance of multi-pass extraction has been demonstrated with a crystal that does not allow single-pass extraction. The energy dependence of crystal extraction has been measured at three beam energies, and found to be in very good agreement with expectations. It has also been shown that the procedure for setting up extraction with a crystal is fast and easy, and that the extracted beam is very stable.

During the measurements at the SPS, significant progress has been made in the understanding of the extraction process.

Preface

The work for this dissertation was carried out at the European Laboratory for Particle Physics (CERN) near Geneva, Switzerland. The author was a CERN doctoral student in the Accelerator Physics group of the SL (SPS/LEP) Division for two and a half years. During this time, the work was supported, in addition to CERN, by the Institute for Particle Physics Technology and by the Helsinki Institute of Physics. During the writing phase of the thesis, the work was supported by the Academy of Finland and The Foundation of Technology from Finland. I would like to thank all these institutions for their support.

The Crystal Extraction collaboration was established to study the feasibility of beam extraction with a bent crystal at the CERN Super Proton Synchrotron (SPS) with a view to using the technique in the future Large Hadron Collider (LHC). The collaboration was initially a rather large group of more than 50 people. At this time, the author was a CERN technical student and prepared a master's thesis on the instrumentation for the experiment.

The studies of crystal assisted extraction were continued from 1994 until 1996 in the framework of the LHC studies in order to gain a more detailed understanding of the extraction process. The work for a doctoral thesis was started in July 1994, from which time there were only a few people actively working on the subject. The work as a technical student provided the author with a thorough knowledge of the data acquisition system of the experiment and provided a good starting point for the doctoral thesis work. Working in a small group gave the author the opportunity to have responsibilities in many different areas such as developing, maintaining and operating the data acquisition system, analysing the measured data and performing computer simulations. The opportunity to prepare experiments and observe the development of ideas to raw data and finally to physics results was invaluable.

The successes of the SPS crystal extraction experiment are based on the careful work of many people in different fields. The work has included, for example, planning and design of the experiment, preparation and installation of the crystals, development and installation of the detectors and data acquisition system, and understanding the measurement results. I would like to thank all of the people who have worked for the experiment. Here I would like to mention a few of them who have been actively involved with the experiment during the doctoral thesis work. Werner Herr was the crystal extraction activity leader at CERN and the supervisor of this thesis. I had the pleasure of working with many colleagues at CERN, most closely with X. Altuna, B. Dehning, K. Elsener, G. Ferioli, A. Ferrari, G.P. Ferri, G. Fidecaro, W. Fischer, R. Guinand, M. Gyr, B. Halvarsson, W. Höfle, H. Jakob, L. Jensen, R. Louwerse, U. Mikkelsen, I. Milstead, F. Schmidt, R. Schmidt, B. Vettermann, G. Vuagnin and E. Weisse. In addition, I am grateful to A. Freund, R. Hustache and A. Paul from ESRF in Grenoble for providing the high-quality crystals. I would also like to thank the SL Division for the opportunity to perform the measurements at the SPS.

I express my gratitude to professors Eero Byckling and Martti Salomaa from the Helsinki University of Technology for supporting my studies and thesis work.

I am very grateful to my parents Saara and Teemu, and my sister Sanna, for the support and encouragement they have given me during my studies.

Lastly, and most importantly, I would like to thank my wife Doreen for her patience, encouragement and continuous support.

Geneva, August 21, 1997

Jukka Klem

Contents

List of Commonly Used Symbols

α	Accelerator alpha function
a_{B}	Bohr radius
a_{TF}	Thomas-Fermi screening length
$\vec{B}$	Magnetic field
b,b'	Impact parameter and impact angle
β	Accelerator beta function or relativistic beta
d_{p}	Planar spacing
e	Elementary charge
E,$E_{\perp}$	Energy, transverse energy
ε	Emittance
ε_{s}	Surface transmission
f	Frequency
F	Dechanneling fraction
γ	Accelerator gamma function or relativistic gamma
I	Ionization potential
k	Kick strength
κ	Curvature
L	Crystal length
L_{B}	Dechanneling length in a bent crystal
L_{D}	Dechanneling length
L_{eff}	Effective crystal length
N	Number of atoms per unit density
p, $p_{\perp}$	Momentum, transverse momentum
ψ	Angle of incidence
ψ_{crit}	Critical channeling angle
Q	Tune
R	Average machine radius
R_{B}	Bending radius
ρ	RMS thermal displacement
s	Path length, longitudinal coordinate
t	Time
τ	Beam lifetime
$U(x)$	Planar potential in crystal
v	Velocity
x,x'	Horizontal coordinate and angle
x_{crit}	Critical horizontal coordinate
y,y'	Vertical coordinate and angle
Z	Atomic number
Z_1,Z_2	Projectile and target atomic numbers

Chapter 1

Introduction

The European Laboratory for Particle Physics (CERN) is located at the French–Swiss border near Geneva, Switzerland. The acronym CERN comes from the earlier French title: 'Conseil Européen pour la Recherche Nucléaire'.

CERN operates a complex of particle accelerators to study fundamental laws of physics in high-energy particle collisions. The largest accelerator at CERN is currently the Large Electron Positron collider (LEP) with its circumference of 27 km. The next major project at CERN is the Large Hadron Collider [1, 2] (LHC) to be built in the existing LEP tunnel. The LHC beam will be supplied by a chain of proton accelerators, shown in Fig. 1.1. The proton beam coming from a linear accelerator (LINAC) goes through the PS Booster (PSB), the CERN Proton Synchrotron (CPS) and finally the Super Proton Synchrotron (SPS) before being injected at 450 GeV into the LHC.

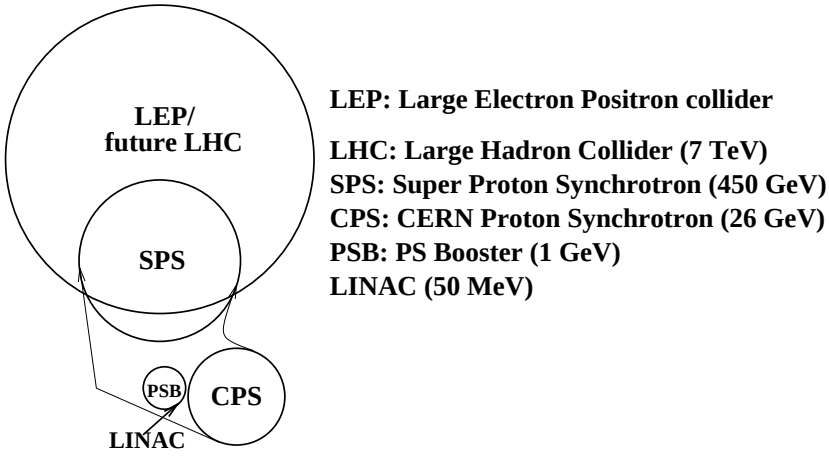

Figure 1.1: Schematic illustration of CERN's proton accelerators.

The LHC will provide proton–proton collisions with a centre-of-mass energy of 14 TeV and a luminosity of 10^{34} cm^{-2} s^{-1}. It will also provide heavy-ion (lead) collisions with a centre-of-mass energy of more than 1000 TeV. Two general-purpose proton–proton experiments will be built at the LHC: CMS [3] and ATLAS [4]. For the study of lead-ion collisions, the ALICE [5] experiment will be constructed.

The LHC will provide the necessary conditions for the study of B particles con-

taining the beauty (b) quark. To complement the B-physics capabilities of the two general-purpose detectors, a dedicated B-physics experiment will be built. Initially, three different experimental approaches were considered: 1) colliding beams at 14 TeV (the COBEX project [6]), 2) an internal gas jet target (the GAJET project [7]) and 3) a beam extracted from the LHC beam halo to a fixed target using a bent crystal (the LHB project [8]). For the third approach, the RD22 collaboration was established to study beam extraction with a bent crystal at the SPS [9]. For the study of B physics at the LHC, the colliding beam approach was chosen [10], but the option to have a fixed-target experimental facility at the LHC had not yet been abandoned and the extraction studies at the SPS were continued.

Classical slow extraction schemes are based on resonant beam excitation which moves the particles across an electrostatic septum. The electrostatic septum gives the particles a kick strong enough to make them hit the field region of magnetic septa. The magnetic septa can give stronger deflection angles that are needed for extraction. At the LHC, the beam energy is 7 TeV. At this high energy, the classical extraction methods become very difficult and expensive, and the only feasible way to extract the beam seems to be with a bent crystal. Furthermore, the classical extraction methods based on resonant beam excitation cannot be used in parasitic mode, i.e. in parallel with colliding beam experiments. A crystal could, however, be used for extraction in parasitic mode without external beam excitation. The crystal would extract particles that arrive in the beam halo because of natural diffusion and would be lost anyway on collimators of the beam cleaning system. The luminosity in the colliding beam experiments would not be reduced, but the crystal set-up would have to be carefully integrated within the beam cleaning system in order not to cause a quench in the superconducting magnets. Thus crystal assisted extraction ('crystal extraction' for short) would open interesting physics prospects by providing high-energy proton or heavy-ion beams to a fixed-target experimental facility. However, extraction with a bent crystal is a new method, and to gain a better understanding of the crystal and accelerator parameters that affect the extraction process, several measurements have been carried out at the SPS.

1.1 Author's contribution

The author of the thesis has been involved in most activities related to the crystal extraction experiment at the SPS. His initial participation concentrated on the work with the data acquisition system. This work is presented in his master's thesis: 'Instrumentation for crystal extraction experiment at the CERN-SPS' [59]. Even at this time the author started analysing the measurement data, and since starting work on a doctoral thesis in July 1994, he has been responsible for the data analysis. After the work described in Ref. [68], i.e. since May 1995, the author has been responsible for the computer simulations. The author's contribution to the crystal extraction experiment can be summarized as follows.

- Developing and maintaining the data acquisition system of the experiment, and operating it during measurements.
- Planning the experiments and designing new installations in the SPS accelerator.
- Being responsible for the data analysis. All experimental results shown in the thesis (besides Table 7.1) have been analysed by the author.
- Being responsible for the simulation of the extraction process (after May 1995). All the simulation results shown in Chapters 7 and 8 have been obtained by the author.

The main results presented in this thesis have been published in the following articles:

- H. Akbari et al., "First results on proton extraction from the CERN-SPS with a bent crystal", Phys. Lett. **B313** (1993) 491.
- X. Altuna et al., "High efficiency multi-pass proton beam extraction with a bent crystal at the SPS", Phys. Lett. **B357** (1995) 671.
- K. Elsener et al., "Proton extraction from the CERN SPS using bent silicon crystals", Nucl. Instrum. Methods **B119** (1996) 215.
- G. Arduini et al., "On the energy dependence of proton beam extraction with a bent crystal", Phys. Lett. **B422** (1998) 325.

In addition, the thesis includes some yet unpublished simulation and experimental results.

Results have also been published in the proceedings of several particle accelerator conferences: Refs. [77, 82, 85, 90, 91, 92] in the bibliography. Further and more detailed information about the measurement results can be found in several CERN MD notes: Refs. [46, 50, 84, 86, 87, 89]. The author of the thesis is co-author in all of the above-mentioned publications and notes.

1.2 Outline of the thesis

The aim of this thesis is to provide a comprehensive description of the crystal assisted proton extraction experiment at the CERN-SPS. However, more emphasis is put on the aspects where the author has been actively involved, i.e. data acquisition, simulations and experimental results. Recent very interesting results on lead-ion extraction [91, 93] are not included in the thesis.

Chapter 2 introduces linear dynamics in particle accelerators. The working principles of modern synchrotrons are shown and some concepts related to particle motion

in synchrotrons are explained. This introduction is restricted to the concepts needed to understand the crystal extraction process and the simulation model.

Chapter 3 describes channeling of high-energy protons in bent silicon crystals. A model for calculating the efficiency of deflection in bent crystals, originating from beam-line experiments, is presented.

Chapter 4 shows how bent crystals can be used in the extraction of protons from high-energy storage rings. Terms such as impact parameter and angle, single- and multi-pass extraction and extraction efficiency are explained.

In Chapter 5 the crystal extraction experiment at the SPS is described. The experimental set-up and the experimental procedures followed during measurements are explained, and the different types of crystals used in the experiments are shown. The different detectors used for the detection of the extracted beam and the data acquisition system are described.

The computer simulation model of the extraction experiment is presented in Chapter 6. Simulation of beam diffusion and the multi-pass extraction process are explained.

The principal chapter of the thesis is Chapter 7 where the experimental results obtained with different crystals, beam energies and beam excitation methods are shown. The experimental results are also compared with the simulation results.

In Chapter 8 possible ways of improving a crystal assisted extraction experiment and possible future applications such as the LHC are discussed.

Chapter 2

Accelerator Physics

The purpose of this chapter is to introduce the principles of modern synchrotrons and some concepts related to particle motion in synchrotrons. The introduction is restricted to the concepts needed to describe the crystal extraction process.

In a circular accelerator, the beam particles are designed to follow a predescribed path, the closed orbit. Since this orbit (also called the design orbit) is curved, bending forces are needed. In addition to this, beam particles may deviate from the ideal path, and therefore focusing forces are required to hold particles close to the design orbit. Electromagnetic fields can produce both the bending and focusing forces, known as Lorentz forces. The Lorentz force is expressed by

$$\vec{F} = e(\vec{E} + \vec{v} \times \vec{B}), \tag{2.1}$$

where e is the elementary charge, $\vec{v}$ is the velocity of the particle, and $\vec{E}$ and $\vec{B}$ are electrical and magnetic field vectors, respectively. For relativistic particles with velocity close to the speed of light ($v \sim c$), a magnetic field of 1 T corresponds to a very large electric field of 3×10^8 V/m. Therefore, in high-energy accelerators magnetic fields are used for beam guidance.

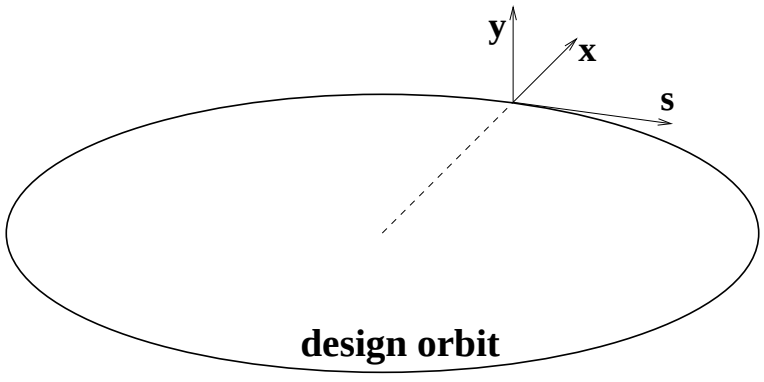

Figure 2.1: Coordinate system for particle motion with respect to the design orbit.

The coordinate system used with respect to the design orbit is shown in Fig. 2.1. The longitudinal coordinate along the design orbit is s. The two transverse coordinates

are x and y. The (x, s)-plane is chosen to be in the horizontal plane, and therefore y is the vertical coordinate. When the particles enter the crystal placed in the beam halo, the coordinate system used is slightly different. For movement inside the crystal, x and y are the horizontal and vertical transverse coordinates, and the longitudinal coordinate along the crystal planes is z.

2.1 Linear beam dynamics

Bending and focusing of beam particles is done by magnetic elements placed along the design orbit. Dipole magnets can be used to bend the trajectory of the particles to follow a circular orbit, and focusing can be achieved by quadrupole magnets. In the presence of only linear magnetic fields, the theory of particle dynamics is referred to as linear beam dynamics [11, 12, 13].

2.1.1 Equation of motion

The horizontal and vertical magnetic fields in dipole and quadrupole magnets can be expressed as

$$B_{\mathrm{x}} = gy, \tag{2.2}$$
$$B_{\mathrm{y}} = B_{\mathrm{y0}} + gx, \tag{2.3}$$

where B_{y0} is the vertical field in a dipole magnet. The gradient of the quadrupole field g is

$$g = \frac{\partial B_{\mathrm{y}}}{\partial x} = \frac{\partial B_{\mathrm{x}}}{\partial y}, \tag{2.4}$$

where B_{x} and B_{y} are the horizontal and vertical field components of a quadrupole magnet.

The equations of motion for a particle moving in linear magnetic fields are

$$x'' + \left(\frac{1}{\rho^2} + k\right) x = 0, \tag{2.5}$$
$$y'' - ky = 0, \tag{2.6}$$

where $\rho = p/eB_{\mathrm{y}}$ is the bending radius for the particle trajectory in a dipole field, and $k = eg/p$ is the focusing strength in a quadrupole.

Equations (2.5) and (2.6) can be expressed in a simplified form

$$u'' + K(s)u = 0, \tag{2.7}$$

where u stands for either of the transverse coordinates x or y, and focusing from bending and quadrupole magnets is combined into

$$K(s) = \frac{1}{\rho(s)^2} + k(s). \tag{2.8}$$

2.1.2 Piecewise method of solution

The focusing parameter $K(s)$ obtains different values in the various elements along a beam transport line. Along each element i.e. within a drift space, a bending magnet or a quadrupole magnet the value of $K(s)$ can be regarded as constant. In this case, the equation of motion can be solved by using a piecewise method of solution. The solutions can be expressed in transport matrix formulation by

$$\begin{pmatrix} u(s_2) \\ u'(s_2) \end{pmatrix} = \begin{pmatrix} m_{11} & m_{12} \\ m_{21} & m_{22} \end{pmatrix} \begin{pmatrix} u(s_1) \\ u'(s_1) \end{pmatrix}, \tag{2.9}$$

where u is the transverse position (either x or y) and $u' = du/ds$ is the transverse angle. The transport matrix shows how the position and angle change from position s_1 to position s_2 along the beam line.

The transport matrices can be derived for a variety of beam-line elements. For example, in a drift space between two magnets the focusing parameter $K = 0$. The same is true in the vertical plane if B_y is constant, and in the horizontal plane for $1/\rho^2 \ll 1$ and $K = 0$. The transport matrix for a drift space is

$$M_\mathrm{D} = \begin{pmatrix} 1 & s_2 - s_1 \\ 0 & 1 \end{pmatrix} = \begin{pmatrix} 1 & L \\ 0 & 1 \end{pmatrix}, \tag{2.10}$$

where $L = s_2 - s_1$ is the length of the drift space.

In a quadrupole magnet there is no bending and therefore $1/\rho^2 = 0$. In a quadrupole, the focusing parameter K is positive in one plane and negative in the other. If $K > 0$, the quadrupole is focusing and if $K < 0$, the magnet is defocusing. The transport matrices for a focusing quadrupole (M_QF) and for a defocusing quadrupole (M_QD) in either the horizontal or vertical plane are

$$\begin{aligned} M_\mathrm{QF} &= \begin{pmatrix} \cos(\sqrt{k}L) & \frac{1}{\sqrt{k}}\sin(\sqrt{k}L) \\ -\sqrt{k}\sin(\sqrt{k}L) & \cos(\sqrt{k}L) \end{pmatrix}, \\ M_\mathrm{QD} &= \begin{pmatrix} \cosh(\sqrt{|k|}L) & \frac{1}{\sqrt{|k|}}\sinh(\sqrt{|k|}L) \\ -\sqrt{|k|}\sinh(\sqrt{|k|}L) & \cosh(\sqrt{|k|}L) \end{pmatrix}, \end{aligned} \tag{2.11}$$

where L is the length of the quadrupole.

By combining the transformation matrices of the individual beam-line elements, it is possible to follow the particle trajectories along the beam line. The individual matrices representing drift spaces, dipole and quadrupole magnets, etc. can be multiplied to give a transformation matrix that represents the whole beam line.

2.1.3 Closed-form solution

Another way of solving Eq. (2.7) is based on the fact that the equation of particle motion under the effect of linear magnet elements is a form of Hill's equation. In a circular accelerator the focusing term of equation $u'' + K(s)u = 0$ is periodic, i.e. $K(s) = K(s + C)$. The period length C may be the circumference of the synchrotron or shorter.

A general solution for the equation of motion can be expressed by

$$u(s) = \sqrt{a\beta(s)} \cos\left[\phi(s) + \phi_0\right], \tag{2.12}$$

where a and ϕ_0 are integration constants depending on initial conditions, and $\beta(s)$ and $\phi(s)$ are periodic functions with the periodicity C. The function $\beta(s)$ is called the betatron function, and the oscillatory motion of a particle along the accelerator is called betatron motion. The difference in phase function $\phi(s)$ between two points s_1 and s_2 can be expressed as

$$\phi(s_2) - \phi(s_1) = \int_{s_1}^{s_2} \frac{1}{\beta(s)}\, ds. \tag{2.13}$$

In a circular accelerator, the number of horizontal and vertical betatron oscillations per turn is

$$Q_{\mathrm{x,y}} \equiv \frac{1}{2\pi} \oint \frac{1}{\beta_{\mathrm{x,y}}(s)} ds. \tag{2.14}$$

Q_{x} and Q_{y} are called the horizontal and vertical tunes of the accelerator.

In addition to $\beta(s)$, two more Twiss parameters [14] (also called Courant–Snyder parameters) $\alpha(s)$ and $\gamma(s)$ can be defined:

$$\alpha(s) = -\frac{1}{2}\frac{d\beta(s)}{ds}, \tag{2.15}$$

$$\gamma(s) = \frac{1 + \alpha^2(s)}{\beta(s)}. \tag{2.16}$$

By using the Twiss parameters, the transport matrix M_{12} (Eq. (2.9)) between two points s_1 and s_2 in the accelerator can be expressed as

$$\begin{pmatrix} \sqrt{\frac{\beta_2}{\beta_1}}[\cos(\Delta\phi) + \alpha_1 \sin(\Delta\phi)] & \sqrt{\beta_1\beta_2}\sin(\Delta\phi) \\ \frac{\alpha_1-\alpha_2}{\sqrt{\beta_1\beta_2}}[\cos(\Delta\phi) - \frac{1+\alpha_1\alpha_2}{\sqrt{\beta_1\beta_2}}\sin(\Delta\phi)] & \sqrt{\frac{\beta_1}{\beta_2}}[\cos(\Delta\phi) - \alpha_2\sin(\Delta\phi)] \end{pmatrix}, \tag{2.17}$$

where $\beta_1 = \beta(s_1)$, $\beta_2 = \beta(s_2)$, $\alpha_1 = \alpha(s_1)$, $\alpha_2 = \alpha(s_2)$ and the phase difference between the two points $\Delta\phi = \phi(s_2) - \phi(s_1)$. If the values of the Twiss parameters are known, it is possible to calculate the trajectories of beam particles at any point in the accelerator.

2.1.4 Beam size and emittance

The position and angle of the particle trajectory with respect to the design orbit are given by $u(s)$ and $u'(s)$:

$$u(s) = \sqrt{a\beta}\cos(\phi + \phi_0) \tag{2.18}$$

$$u'(s) = -\sqrt{a}\frac{\alpha}{\sqrt{\beta}}\cos(\phi + \phi_0) - \frac{\sqrt{a}}{\beta}\sin(\phi + \phi_0). \tag{2.19}$$

If the phase dependence is eliminated from the equations above, a constant of motion called the Courant–Snyder invariant [15, 16]

$$\gamma u^2 + 2\alpha u u' + \beta u'^2 = a \tag{2.20}$$

is obtained. Equation (2.20) defines an ellipse in the transverse (u, u') phase space. The parameters α, β and γ determine the shape and orientation of the ellipse, and the area of the ellipse is defined by the parameter a. Under the influence of conservative forces, the Courant-Snyder invariant of a single particle does not change, and the particle stays in the contour of the same phase-space ellipse. The Twiss parameters depend on the coordinate s, and therefore the form of the ellipse changes along the accelerator as a function of s.

The phase-space area populated by a group of particles is called the emittance. The beam size $\sigma(s)$ at a certain location s in the accelerator depends on the value of the β-function at point s and on the beam emittance:

$$\sigma(s) = \sqrt{\beta(s)\varepsilon}. \tag{2.21}$$

In proton accelerators such as the SPS, the normalized (2σ) emittance

$$\varepsilon^* = \frac{(2\sigma)^2\gamma}{\beta} = \frac{4\sigma^2\gamma}{\beta} \tag{2.22}$$

is often used. The relativistic factor γ makes this definition of emittance invariant at different beam energies.

2.1.5 Momentum dispersion

The motion of a particle with the momentum p different from the design momentum p_0 is given by the inhomogeneous Hill equation

$$u'' + K(s)u = \frac{1}{\rho}\frac{\Delta p}{p}, \tag{2.23}$$

where $\Delta p = p - p_0$ is the momentum deviation. The change in particle amplitude due to momentum deviation can be expressed as

$$u(s) = u_\beta(s) + u_\mathrm{D}(s) = u_\beta(s) + D(s)\frac{\Delta p}{p}, \tag{2.24}$$

where $D(s)$ is the dispersion function. The dispersion function $D(s)$ is determined by the bending properties around the accelerator, whereas, for example, the β-function is determined by the focusing properties.

2.1.6 Motion due to angular deflection

If a particle is travelling along the design orbit and it experiences an angular deflection (kick) k, its motion is thereafter given by

$$u(s) = k\sqrt{\beta_\mathrm{k}\beta(s)}\sin[\phi(s) - \phi_\mathrm{k}], \tag{2.25}$$

$$u'(s) = k\sqrt{\frac{\beta_\mathrm{k}}{\beta(s)}}[\cos(\phi(s) - \phi_\mathrm{k}) - \alpha(s)\sin(\phi(s) - \phi_\mathrm{k})], \tag{2.26}$$

where β_k and ϕ_k are the values of betatron function and phase function at the point of deflection, respectively. For example, small deflections can be given by electrostatic deflector plates, or the kick can be due to scattering in the crystal material. The change in the transverse amplitude of the particle motion depends, in addition to the kick strength, on the values of the β-function at the point of deflection and at the point of observation.

Chapter 3

Crystal channeling

The purpose of this chapter is to introduce some concepts related to charged particle channeling in crystals that are needed later in the thesis and especially in the description of the computer simulations. The emphasis is on describing channeling as it is used in the beam extraction experiment at the SPS, i.e. high-energy planar channeling of protons in bent silicon crystals [17, 18, 19, 20, 21].

3.1 Principle of channeling

A crystal is a regular arrangement of atoms located on lattice positions. Depending on the angle of observation, the atoms in a crystal are arranged in strings or in planes. Between the strings and the planes one can find 'channels' of empty space. In 1912, Stark predicted [22] that along these 'channel' directions, a crystal can be more transparent to the passage of charged particles than an amorphous material. In effect, when a positively charged particle hits a crystal at a small angle with respect to a crystallographic direction, its motion is not determined by scatterings from single atoms as in amorphous material, but by coherent scatterings on atomic strings or planes. With a small impact angle the particle may be trapped in the potential wells formed by atomic strings or planes, i.e. the particle may be channeled in the crystal. The motion of a channeled particle is restricted to part of the lattice where there are no atoms and where the electron density is reduced. Therefore, a channeled particle experiences less scattering and energy loss than a particle hitting the crystal in a so-called 'random' direction.

The channeling effect was first discovered in the early 1960s when unexpectedly long ions ranges were observed in crystals [23, 24].

3.2 Continuum model

A theoretical description for channeling was given by Lindhard [25] using the continuum model of crystal potentials. The particles that move in a crystal at a small angle to a crystallographic axis or plane, change their direction of motion only by a small amount in each binary collision with lattice atoms, and the successive collisions are correlated

so that one can consider a particle to interact with an atomic string or plane instead of individual lattice atoms. In the continuum model, the charges of individual atoms can be replaced by a continuum charge obtained by smearing and averaging the individual atomic charges in a string or a plane. The principle of continuum charge is shown in Fig. 3.1. In the planar channeling case, the atomic planes can be regarded as flat planes of charge, between which the motion of the channeled particles is confined.

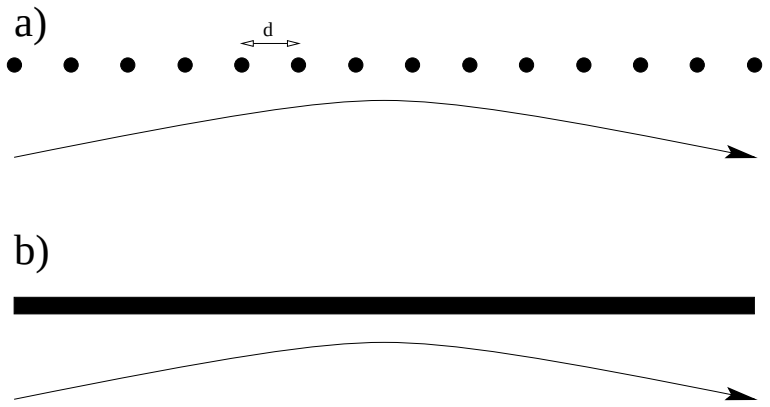

Figure 3.1: In the continuum model the interaction of a particle with an atomic string (case a) can be replaced by an interaction with a continuum charge (case b).

The planar continuum potential can be calculated by averaging atomic potentials over two coordinates (e.g. Ref. [17]):

$$U(x) = N d_{\mathrm{p}} \int_{-\infty}^{\infty} \int_{-\infty}^{\infty} V\left(\sqrt{x^2 + y^2 + z^2}\right) \, dy \, dz, \tag{3.1}$$

where N is the number of atoms per unit density, d_{p} the distance between crystal planes, V the atomic potential and x the transverse coordinate with respect to the atomic plane.

For the atomic potential the so-called standard potential by Lindhard can be used:

$$V(r) = \frac{Z_1 Z_2 e^2}{r} \left(1 - \frac{r}{\sqrt{r^2 + C^2 {a_{\mathrm{TF}}}^2}}\right), \tag{3.2}$$

where Z_1 and Z_2 are the projectile and target atomic numbers, e the elementary charge and $C^2 \approx 3$ is a constant. $a_{\mathrm{TF}} = 0.8853\, a_{\mathrm{B}} ({Z_1}^{2/3} + {Z_2}^{2/3})^{-1/2}$ is the Thomas-Fermi screening length, where $a_{\mathrm{B}} = 0.529$ Å is the Bohr radius.

By using Eqs. (3.1) and (3.2), one can obtain the planar continuum potential for a single plane in a crystal:

$$U(x) = 2\pi Z_1 Z_2 e^2 N d_{\mathrm{p}} \left(\sqrt{x^2 + C^2 {a_{\mathrm{TF}}}^2} - x\right) \tag{3.3}$$

The thermal motion of lattice atoms causes smearing of the continuum potentials. Owing to thermal motion, the atoms have a Gaussian probability distribution around their mean position. The RMS thermal displacement $\rho = 0.075$ Å in silicon at 300 K [17].

For more quantitative calculations of the planar potentials, one can use the thermally averaged Doyle–Turner potential [17, 26]:

$$U(x) = 2\sqrt{\pi} Z_1 e^2 a_\mathrm{B} N d_\mathrm{p} \sum_{i=1}^{4} \frac{a_\mathrm{i}}{\sqrt{B_\mathrm{i} + \rho^2}} \exp\left(-\frac{x^2}{B_\mathrm{i} + \rho^2}\right), \tag{3.4}$$

where $B_\mathrm{i} = b_\mathrm{i}/4\pi^2$, and the constants a_i and b_i are given in Table 3.1.

Table 3.1: Parameters for Doyle–Turner potential for silicon [26].

a_1 [Å]	a_2 [Å]	a_3 [Å]	a_4 [Å]	b_1 [Å^2]	b_2 [Å^2]	b_3 [Å^2]	b_4 [Å^2]
2.1293	2.5333	0.8349	0.3216	57.7748	16.4756	2.8796	0.3860

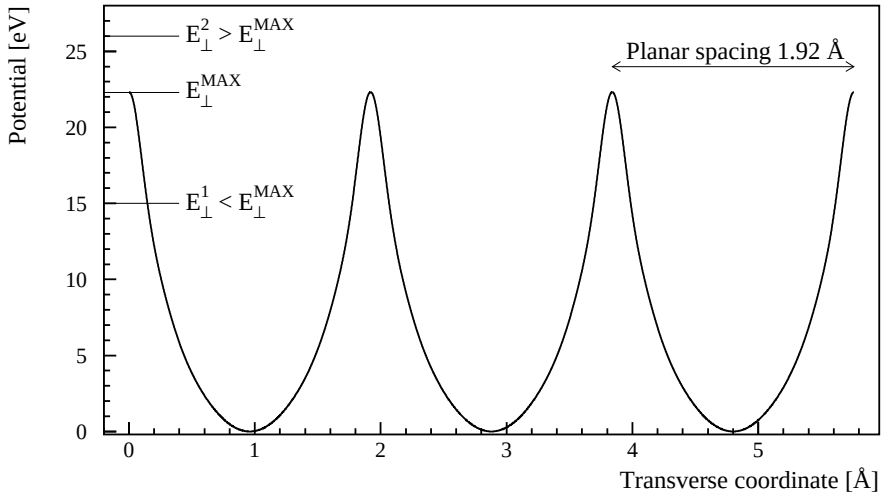

Figure 3.2: The planar potential for (110) plane in silicon calculated by using the Doyle-Turner potential (Eq. (3.4)).

When a particle hits a crystal, depending on the position and angle of the hit the particle acquires transverse energy:

$$E_\perp = \frac{{p_\perp}^2}{2m} + U(x) = \frac{1}{2}\, p\, v\, \psi^2 + U(x), \tag{3.5}$$

where $p_\perp$ and m are the transverse momentum and mass of the particle, and ψ is the angle of incidence. Since the continuum potential $U(x)$ does not depend on the coordinates y and z over which the charge averaging is done, the energy is conserved in motion along these directions. Therefore the transverse energy $E_\perp$ is also a conserved quantity in the continuum model.

The height of the planar potential can be related to the maximum transverse energy that a particle can have in the channeling mode. For the particle to be channeled, the following condition has to be fulfilled:

$$E_\perp = \frac{1}{2}\, p\, v\, \psi^2 + U(x) < U^{\max}. \tag{3.6}$$

The largest angle of incidence that allows channeling, called the critical channeling angle ψ_{crit}, corresponds to the case where the particle enters the crystal exactly between two planes, and the transverse kinetic energy equals the potential height:

$$E_\perp^{\max} = U^{\max} = \frac{1}{2}\, p\, v\, \psi_{\text{crit}}^2 \Rightarrow \psi_{\text{crit}} = \sqrt{\frac{2U^{\max}}{pv}}. \tag{3.7}$$

If the transverse energy of a particle is lower than the potential height ($E_\perp^1 < E_\perp^{\max}$ in Fig. 3.2), channeling is possible. On the other hand, if the transverse energy is much higher than the potential height ($E_\perp^2 \gg E_\perp^{\max}$ in Fig. 3.2), the particle cannot be channeled and it traverses the crystal as if it were amorphous material.

By using Eqs. (3.3) and (3.7), one can obtain the Lindhard critical angle:

$$\psi_{\text{crit}} = \sqrt{\frac{4Z_1 Z_2\, e^2\, N d_{\text{p}}\, C a_{\text{TF}}}{pv}}. \tag{3.8}$$

For planar channeling along (110) plane in silicon, the critical channeling angle is:

$$\psi_{\text{crit}} = \frac{5\,\mu\text{rad}}{\sqrt{p\,[\text{TeV}/c]}}. \tag{3.9}$$

The values of critical channeling angles at SPS and LHC energies are shown in Table 3.2.

Table 3.2: Critical channeling angles at different beam energies for (110) plane in silicon.

14 GeV	120 GeV	270 GeV	7 TeV
42.3 μrad	14.4 μrad	9.6 μrad	1.9 μrad

A channeled particle performs transverse oscillations in the planar potential created by the atomic planes. The potential is very similar to harmonic potential, especially

for small oscillation amplitudes. The motion of a channeled particle is restricted to a region where there are no atoms and where the electron density is reduced. Therefore, the interactions of the channeled particle with the target material are strongly reduced and the particle can traverse long distances inside the crystal.

The largest transverse oscillation amplitude x_{crit} that a channeled particle can have depends on the thermal vibration amplitude of the lattice atoms. If the particle approaches too close to the atoms, it is soon lost from the channeling state. Experiments [27] have indicated that the critical transverse amplitude is

$$x_{\mathrm{crit}} = \frac{d_{\mathrm{p}}}{2} - 2.5\rho. \tag{3.10}$$

The probability that a particle incident on a crystal will be channeled is called the surface transmission ε_{s}. For a particle with zero impact angle, the (spatial) acceptance of the crystal is $2\,x_{\mathrm{crit}}/d_{\mathrm{p}}$. For silicon (110) plane, this gives $\simeq 80\%$. Consequently, when a parallel beam is incident on a crystal, about 20% of it cannot be channeled because of surface transmission.

In addition to the dependence on the transverse coordinate, the surface transmission depends on the impact angle. For a particle with an impact angle of ψ, the surface transmission becomes

$$\varepsilon_{\mathrm{s}} = 2\frac{x_{\mathrm{crit}}}{d_{\mathrm{p}}}\sqrt{1 - \left(\frac{\psi}{\psi_{\mathrm{crit}}}\right)^2}. \tag{3.11}$$

Here the surface transmission is reduced by the factor $\sqrt{1-(\psi/\psi_{\mathrm{crit}})^2}$, which gives in harmonic approximation the reduction in channeling probability as a function of impact angle [28].

3.3 Dechanneling

In a real crystal, the transverse energy is not strictly conserved but changes because of scattering on electrons and lattice nuclei. Owing to scattering, the transverse energy of a channeled particle typically increases when it traverses a crystal. At some point, the particle may be lost from the channeling state. The reduction of the number of channeled particles as a function of penetration depth can be approximated by exponential decay:

$$N = N_0 \exp\left(-\frac{L}{L_{\mathrm{D}}}\right), \tag{3.12}$$

where L is the length of the crystal and L_{D} the dechanneling length. The value of the dechanneling length can be calculated with [28]

$$L_{\mathrm{D}} = \frac{256}{9\pi^2} \frac{pv}{\ln(2m_{\mathrm{e}}c^2\gamma I) - 1} \frac{a_{\mathrm{TF}} d_{\mathrm{p}}}{Z_1 r_{\mathrm{e}} m_{\mathrm{e}} c^2}, \tag{3.13}$$

where I is the ionization potential, m_{e} is the electron rest mass and r_{e} the classical radius of an electron. Equation (3.13) is in satisfactory agreement with measured dechanneling lengths for crystals at room temperature [28].

Dechanneling lengths at different beam energies for (110) plane in silicon are shown in Table 3.3. In the energy range of the SPS extraction experiments (14–270 GeV), the dechanneling length changes by a large factor. As a result of this, significant effects on the energy dependence of crystal extraction are expected because of dechanneling.

Table 3.3: Dechanneling lengths L_{D} at different beam energies for (110) plane in silicon.

14 GeV	120 GeV	270 GeV	7 TeV
0.92 cm	6.60 cm	13.9 cm	291 cm

The particles that are not channeled when they enter a crystal, may be transferred into the channeling mode inside the crystal. This process, known as 'volume capture' or 'feeding-in' is thus the inverse of dechanneling.

3.4 Channeling in a bent crystal

If the crystal is slightly bent, the channeled particles can still stay trapped between the atomic planes. In a bent crystal, the planar potential is modified by a centrifugal term

$$U_{\mathrm{eff}}(x) = U(x) - \kappa pvx = U(x) - \frac{pvx}{R_{\mathrm{B}}}, \tag{3.14}$$

where R_{B} is the radius of curvature of the crystal and $\kappa = 1/R_{\mathrm{B}}$ is the curvature. $U_{\mathrm{eff}}(x)$ is the effective planar potential inside the crystal.

The effect of bending on the planar potential is shown in Fig. 3.3. In a bent crystal, the centre of the potential is shifted towards the outer plane and the potential-well depth is reduced on the side of the outer plane.

It has been shown [29] that when the crystal curvature increases, at some critical radius of curvature there is no longer a potential well and channeling is not possible. This happens when the minimum of the effective planar potential is shifted to the critical transverse amplitude x_{crit}. The critical radius of curvature is

$$R_{\mathrm{B}}^{\mathrm{crit}} = \frac{pv}{\pi Z_1 Z_2 e^2 N d_{\mathrm{p}}}. \tag{3.15}$$

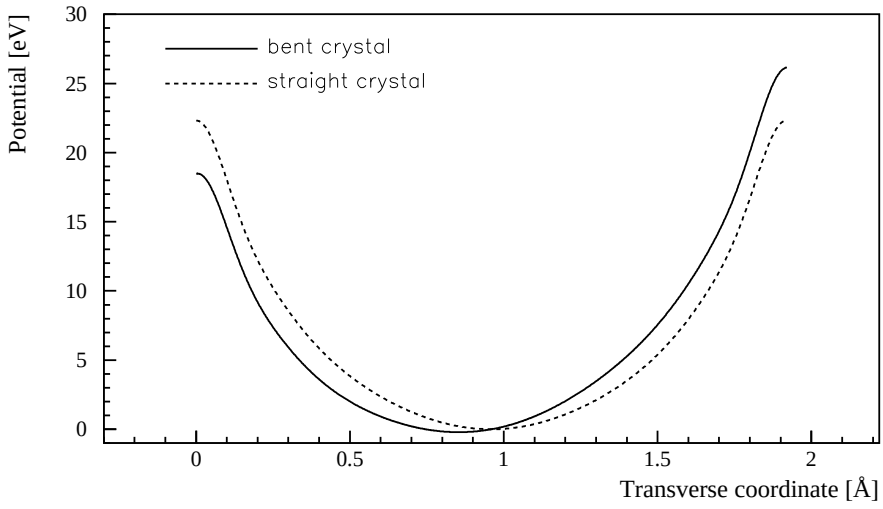

Figure 3.3: The effective planar potential ($R_{\rm B} = 3$ m, $pv = 120$ GeV) in a bent silicon crystal ((110) plane) compared with the potential in a straight crystal.

For (110) plane in silicon the values of critical radius of curvature in metres can be calculated with $R_{\rm B}^{\rm crit} = 1.64{\rm m}\, p\,[{\rm TeV}/c]$. For example, at 120 GeV/c this gives a low value of $R_{\rm B}^{\rm crit} = 0.20$ m. However, the probability of channeling is low already at larger radii so that in real applications for beam deflection crystals are not bent close to the critical curvature.

In a bent crystal the planar potential is modified and therefore the (x, ψ)-phase space available for the channeled particles is reduced. The reduction of the phase space is given by the dechanneling fraction F.

The dechanneling fraction has been measured for proton and positive pion beams moving within (110) planes in silicon at energies between 60 and 200 GeV/c [27]. The measurements were made with a beam that had a large angular spread compared with the critical channeling angle so that the phase space was uniformly populated. The dechanneling fractions are shown in Fig. 3.4 for a crystal at room temperature as a function of dimensionless momentum and curvature parameter Γ. The Γ-parameter is defined as

$$\Gamma = \frac{pv}{2\pi\, R\, Z_1 Z_2\, e^2\, N d_{\rm p}} = \frac{1}{2}\kappa R_{\rm B}^{\rm crit} = \frac{1}{2}\frac{R_{\rm B}^{\rm crit}}{R}. \tag{3.16}$$

The points in Fig. 3.4 are the measurements from Ref. [27], and the line is a fit: $F = 1.08\tanh(6\,\Gamma)$ [30].

In addition to the reduction of phase space, in a bent crystal the dechanneling length is shorter. The dechanneling length in a straight crystal $L_{\rm D}$ is replaced by a

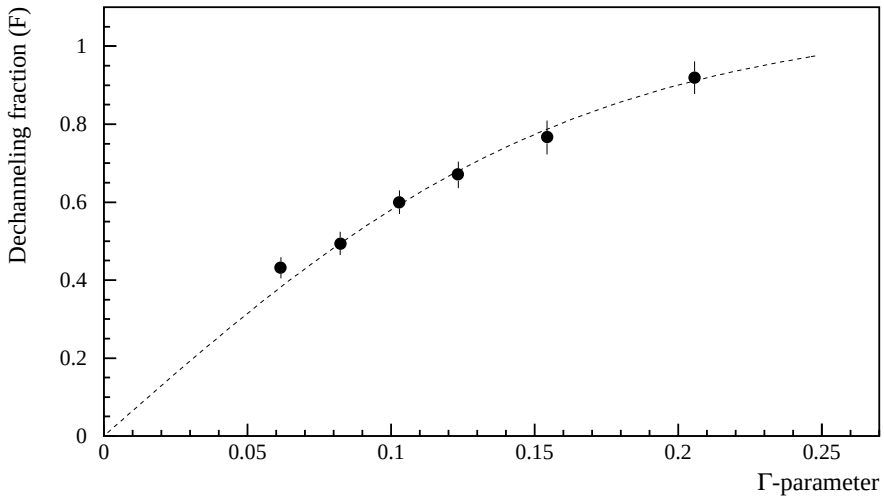

Figure 3.4: Measured values of dechanneling fraction (F) [27].

dechanneling length in a bent crystal L_{B}. The change of dechanneling length can be approximated with

$$L_{\mathrm{D}} \rightarrow L_{\mathrm{B}} = L_{\mathrm{D}}(1 - F)^2. \tag{3.17}$$

Table 3.4: Channeling parameters at different beam energies for bent crystals (silicon (110)-plane).

Beam energy [GeV]	Dechanneling fraction (F)	Modif. dechanneling length (L_{B}) [cm]
14	0.02	0.89
120	0.18	4.45
270	0.39	5.22

3.5 Beam deflection with a bent crystal

The possibility of bending charged particle beams by bent crystal was predicted in 1976 [29]. Soon after, the first beam deflection experiments were carried out at JINR,

Dubna [31] and at CERN [32]. Since then, several experiments have been carried out, e.g. at CERN, Fermilab, JINR and IHEP. Especially interesting are recent deflection experiments at CERN [33, 34, 35, 36] where high deflection efficiencies, above 50%, have been achieved.

3.5.1 Deflection efficiency

The deflection efficiency, i.e. the probability of channeling through the whole length of a crystal, can be expressed as

$$P = \varepsilon_{\mathrm{s}} \exp\left(-\frac{L_{\mathrm{str}}}{L_{\mathrm{D}}}\right) \exp\left(-\frac{L_{\mathrm{bent}}}{L_{\mathrm{D}}(1-F)^2}\right) (1-F), \tag{3.18}$$

where ε_{s} is the surface transmission, and L_{str} and L_{bent} are the lengths of the straight and bent parts of the crystal, respectively. This model for calculating the deflection efficiency has been tested in beam-lines for different bending angles and beam energies in silicon and germanium crystals, and good agreement has been found [33, 34, 35, 36].

The deflection efficiency of a crystal can be reduced because of radiation damage. As a result of strong irradiation, defects are introduced in the crystal lattice, which may lead to increased dechanneling. The modest radiation doses at the SPS crystal extraction experiment do not allow the decrease in extraction efficiency because of radiation damage to be studied. However, another recent experiment has shown that the deflection efficiency in an irradiated silicon crystal is reduced by $6 \pm 2\%$ per 10^{20} protons/cm^2 owing to radiation damage [34, 36, 37]. The small reduction at high fluence gives confidence that it is possible to extract intense proton beams with a crystal.

Chapter 4

Beam extraction with a bent crystal

The purpose of this chapter is to present general issues concerning beam extraction with a bent crystal. The extraction experiment at the CERN SPS and matters closely related to it are explained in Chapter 5.

Extraction is the mechanism that is used to remove beam particles from an accelerator or a storage ring. Classical extraction methods are based on using electrostatic and magnetic septum devices. For example, the first element in the SPS extraction set-up is an electrostatic septum consisting of an array of 50-μm-thick wires. Beam particles are first moved by resonant beam excitation across the electrostatic septum that gives the particles a kick strong enough to make them enter the field region of a magnetic septum. The magnetic septa can give the strong deflection angles needed for extraction. However, at high energies extraction with these classical methods becomes more and more expensive and difficult to operate.

The strong bending power of crystals can be exploited in beam extraction by replacing the classical extraction septa with a bent crystal placed in the beam halo. The principle of beam extraction with a crystal is shown in Fig. 4.1. The particles diffusing out of the beam core arrive at the crystal and can be extracted if they are channeled through the whole length of the crystal.

As the crystal is placed in the beam halo, it does not disturb the beam core. The protons arriving at the crystal diffuse away from the beam core, i.e. these particles do not contribute to the luminosity in a collider but would be lost on collimators. Thus it has been envisaged to use a crystal in a parasitic mode so that the particles which would otherwise be lost can be used for fixed-target experiments through crystal assisted extraction.

4.1 Impact parameters and angles

When a proton hits the crystal, the distance from the crystal surface to the position of the hit is called the impact parameter (b). Similarly, the angle between the crystal planes and the direction of the motion of protons is called the impact angle (b'). The impact parameter and angle of a particle impinging on a crystal determine whether the particle can be channeled (Fig. 4.2). Channeling is possible only if the particle has

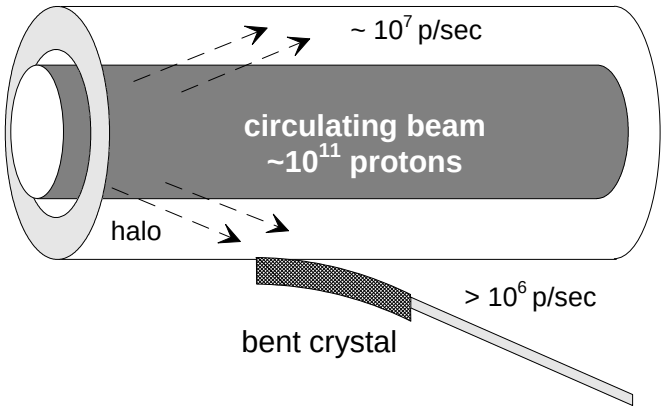

Figure 4.1: Principle of beam extraction with a bent crystal.

a large enough impact parameter to overcome the surface imperfections of the crystal, and if the impact angle is smaller than the critical angle for channeling.

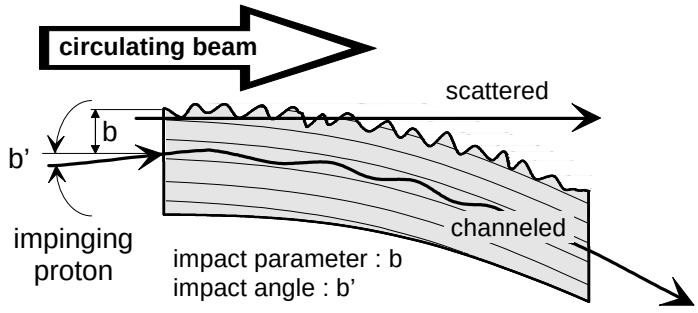

Figure 4.2: A particle impinging in the crystal with impact parameter b and impact angle b'.

4.2 Single- and multi-pass extraction

When a particle arrives at the crystal, it may be channeled and extracted depending on its impact parameter and angle. If this happens when the particle hits the crystal for the first time, i.e. the particle traverses the crystal only once before being extracted, it is referred to as single-pass extraction (or first-pass extraction).

On the other hand, the particles that hit the crystal but are not channeled and

extracted, experience scattering in the crystal material. After the scattering, these particles may still stay within the acceptance of the accelerator. After one or more turns, the scattered particles may again hit the crystal and be extracted. This case is known as multi-pass extraction because the particles pass through (a part of) the crystal more than once.

When particles hit the crystal for the first time, the impact parameters are typically small, less than 1 μm, depending on the diffusion process. If the crystal has an inefficient surface layer whose thickness is large compared to the impact parameters, single-pass extraction may not be possible and one has to rely on multi-pass extraction. At later hits, the impact parameters are larger (see Chapter 6), but the impact-angle distribution is larger as well. This means that even in the case of an imperfect crystal surface, extraction is still possible through a multi-pass process, although possibly with reduced efficiency.

It is difficult to accurately estimate the initial impact parameter distributions that will be obtained in a colliding beam machine. The impact parameters also depend on the operating conditions of the collider. Consequently, relying only on single-pass extraction may be insecure. However, for multi-pass extraction the initial impact parameters are less important, and one can expect multi-pass to work with different initial impact parameter distributions. Multi-pass extraction is also less susceptible to possible crystal surface imperfections, and it provides a larger angular acceptance than single-pass extraction. However, in multi-pass extraction the crystal set-up has to be carefully integrated as a part of the beam cleaning system. To ensure high efficiency extraction in multi-pass mode, the collimators have to be positioned in such a way that the particles can make multiple passes through the crystal and have a chance of being extracted before they are absorbed by the collimator blocks.

4.3 Reasons and methods for beam diffusion

When a beam circulates in a collider, there are several reasons that cause natural diffusion of particles from the beam core to the tails. For example, scattering on the residual gas particles of the vacuum system causes diffusion and losses. In the future, high-energy hadron colliders will be built using superconducting magnets. In these magnets, the field types (dipole, quadrupole, etc.) have to be produced by the coil geometry, which means that nonlinear field errors cannot be avoided. In addition to this, in colliders where two counter-rotating beams are brought into collision, the particles in one beam are influenced by the nonlinear forces of the other beam (beam-beam effect). The magnet field errors and beam-beam effect are another source of diffusion especially for large transverse amplitude particles. All these reasons together cause the formation of a beam halo into which there is a continuous supply of particles. These particles are absorbed by the collimator blocks of the beam cleaning system.

In the dedicated studies of beam extraction with a crystal, artificial beam excitation

methods may be used to create more diffusion than what is produced by the natural reasons for diffusion. For example, the SPS magnets are not superconducting and there is no beam-beam induced diffusion. Consequently, some artificial beam excitation is needed to make the beam particles hit the crystal.

The methods used for artificial beam excitation can be divided into two basic modes: kick mode (Fig. 4.3) and diffusion mode (Fig. 4.4). In kick mode, the whole beam is first deflected, and and as a result of the deflection and of the betatron motion the beam can be made to move towards the crystal at the location of the crystal. In diffusion mode, the slow diffusion can be created, for example, by giving transverse kicks to the beam particles, or by introducing artificial nonlinearities and tune ripple in the accelerator. These diffusion methods and the kick mode have been used in the SPS; they are described in more detail in Section 5.3.

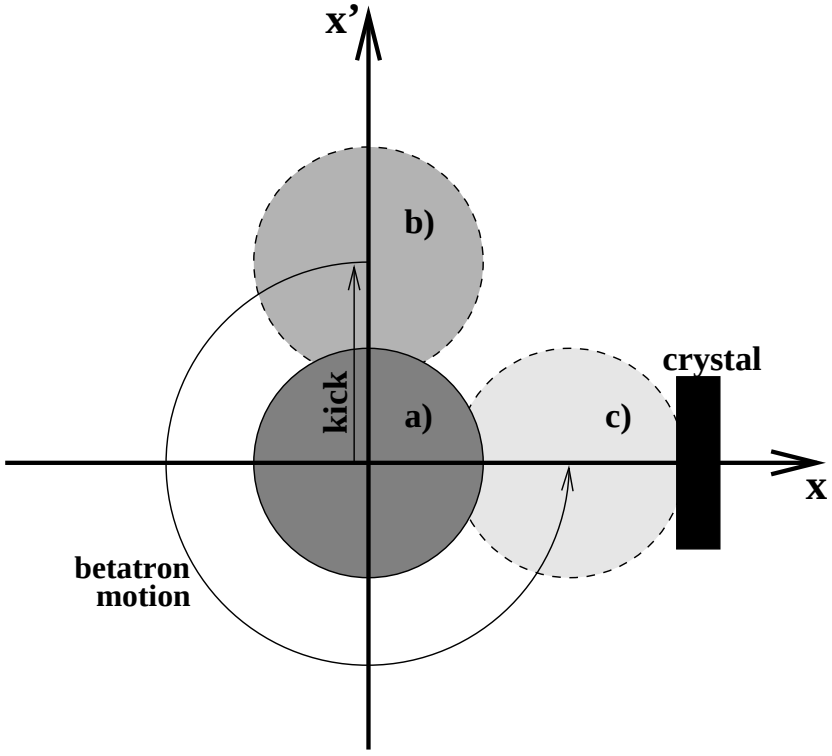

Figure 4.3: Principle of beam excitation in kick mode. The initial beam distribution (a) is deflected. The deflected beam (b) moves as a result of betatron motion towards the crystal (c).

Another method proposed for creating slow and controllable beam diffusion is to introduce noise in the RF system of the accelerator, which creates momentum spread in the longitudinal phase space [38, 39]. The momentum spread is transformed into positional spread in the transverse phase space in a position where dispersion is high.

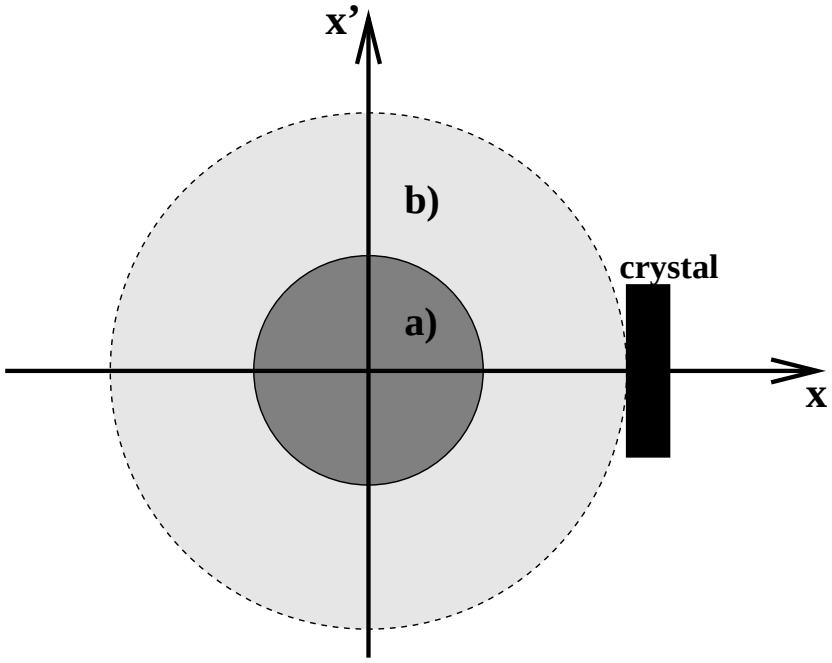

Figure 4.4: Principle of beam excitation in diffusion mode. The transverse size of the initial beam distribution (a) is made to increase slowly. After diffusion the beam occupies a larger region in the phase space (b), and the particles in the halo of the beam can hit the crystal.

4.4 Extraction efficiency

In the extraction with a crystal, one of the most significant measurements is the extraction efficiency ϵ_{ext}, defined as

$$\epsilon_{\text{ext}} = \frac{I_{\text{extracted}}}{I_{\text{lost}}}, \tag{4.1}$$

where $I_{\text{extracted}}$ is the number of particles extracted per second and I_{lost} is the number of particles lost from the accelerator per second because of the crystal.

When a beam is extracted with a bent crystal, the extraction efficiency determines the fraction of the particles lost from the accelerator that can be used in a fixed-target experiment. It is necessary to know the factors affecting the efficiency to be able to optimize an extraction set-up to give a maximal flux of extracted particles. For example, if an external experiment requires more than 10^6 protons per second, and the loss rate from the circulating beam is 10^7 protons per second, an extraction efficiency of more than 10% is needed (see Fig. 4.1). A high extraction efficiency also helps the beam cleaning system: the higher the extraction efficiency, the lower is the number of particles that have to be absorbed by collimators.

Deflection efficiency (Eq. (3.18)) gives the probability for channeling through the whole length of a crystal in a beam line, i.e. when the beam hits the crystal in the centre of the crystal entrance face. The first main difference between deflection efficiency and extraction efficiency is due to the fact that in extraction the particles arrive at the crystal with small impact parameters, which means that in the presence of an inefficient surface layer, channeling may not be possible during the first hit(s). The second difference is that in an accelerator particles may make many passes through the crystal, and be extracted through multi-pass extraction. The first of the differences typically reduces the extraction efficiency relative to deflection efficiency, whereas the second difference increases the efficiency in extraction. As a whole, the extraction efficiency depends, in addition to deflection efficiency, on several factors such as the impact parameter distributions, crystal surface quality, scattering in the crystal material and probability of multiple passes in the crystal.

4.5 Other crystal extraction experiments

The feasibility of beam extraction with a bent crystal was first demonstrated at JINR, Dubna in 1984 [40]. A beam was extracted from the JINR synchrophasotron between energies of 4.2 GeV and 7.5 GeV using a 1.1-cm-long silicon crystal bent by an angle of 35 mrad. However, the extraction efficiency was low, about 0.01%.

Since 1989, protons have been extracted with a bent crystal between energies of 50 GeV and 70 GeV at IHEP, Protvino [41, 42]. Silicon crystals with a length of 6.5 cm and bending angle of 80 mrad have been used. The extraction efficiencies have been below 1%, but the extracted beam has been used for fixed-target physics experiments.

Recently, extraction experiments have been carried out at the Tevatron collider at Fermilab. At the Tevatron, it was possible to study crystal assisted extraction in a superconducting accelerator environment. The beam energy was 900 GeV. The first results from the experiment are shown in Ref. [43]. At the time of writing this thesis, the extraction efficiency from the Tevatron experiment has not been published.

Table 4.1: Crystal extraction experiments.

Location	Energy [GeV]	Deflection angle [mrad]	Crystal length [cm]	Extr. efficiency [%]
JINR, Dubna	4.2–7.5	35	1.1	0.01
IHEP, Protvino	50–70	80	6.5	<1
Fermilab	900	0.6	1.1	not published

Chapter 5

Crystal extraction experiment at the SPS

The Super Proton Synchrotron (SPS) is a 6912-m-long synchrotron that can accelerate protons up to 450 GeV. The principle of crystal extraction experiments at the SPS is shown in Fig. 5.1. During the experiments, the circulating SPS beam is made to grow transversally by random kicks given by an electrostatic deflector. As a result of the beam growth the particles arrive at the crystal placed in the beam halo and can be extracted from the SPS ring in the horizontal plane towards the inside of the SPS ring. The crystals are located in the straight section LSS5 of the SPS.

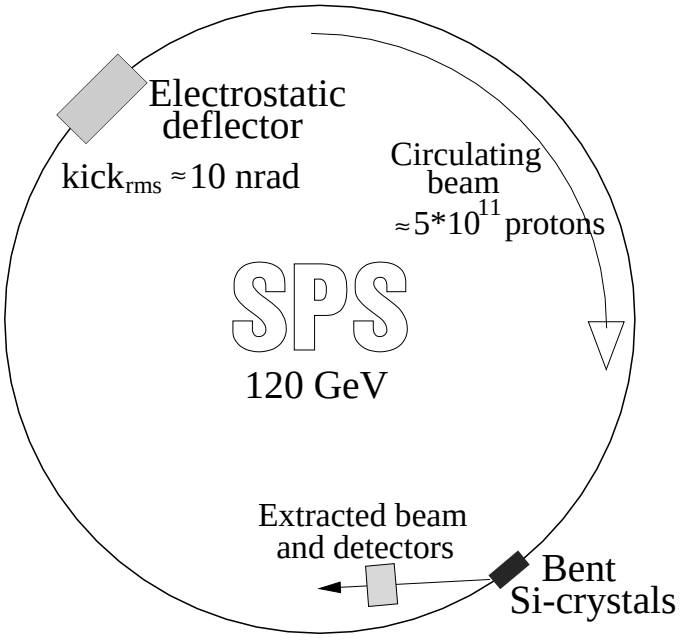

Figure 5.1: Crystal extraction experiment at the SPS.

5.1 Experimental set-up at the SPS

Part of the SPS ring where the crystal extraction experiment is located is shown in Fig. 5.2. In this figure the circulating proton beam comes from the left. Two bent

crystals (C1 and C2) are installed on goniometers and can be used alternately. The protons are extracted in the horizontal plane towards the centre of the SPS ring. The extracted particles come out of the vacuum pipe about 15 m downstream of the crystals through a 0.2-mm-thick stainless-steel window. A set of detectors is located about 22 m downstream of the crystal. A detailed description of the detectors is given in Section 5.5.

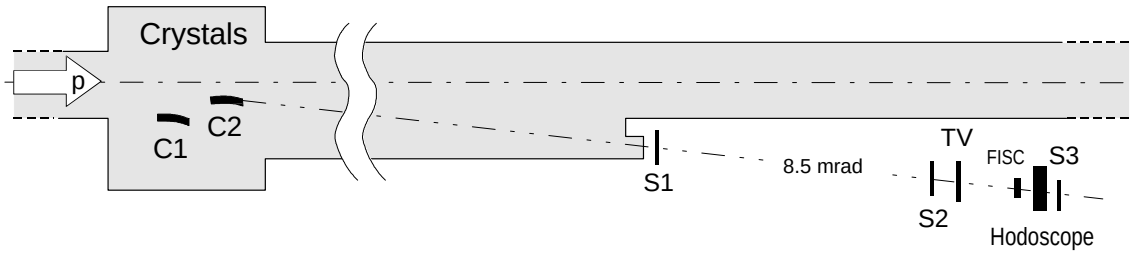

Figure 5.2: The experimental set-up at the SPS.

5.2 Experimental conditions and procedures

For the experiments a beam is injected from the CPS (CERN Proton Synchrotron) accelerator at an energy of 14 GeV into the SPS. The beam is accelerated usually to an energy of 120 GeV for the measurements. At this energy the lifetime of the beam without external excitation can be several hundred hours. The SPS beam is used in coasting (debunched) mode, which means that the RF cavities are switched off and there is a continuous stream of particles in the accelerator.

During most of the experiments the beam energy has been 120 GeV, but to study the energy dependence some measurements have been carried out also at 14 GeV and at 270 GeV.

After injection, the beam intensity is more than 10^{12} protons. To prepare for the measurements, chromaticity is corrected and coupling between horizontal and vertical planes is minimized. The orbit is corrected, and special attention is given to correcting the orbit and orbit angle at the crystal location. After the correction, the residual RMS orbit is less than 0.3 mm in both planes.

The tunes are set to $Q_{\mathrm{x}} = 26.62$ and $Q_{\mathrm{y}} = 26.58$. The horizontal and vertical normalized emittances (2σ values) are $\varepsilon^*_{\mathrm{x}} = 6$–$8$ μm and $\varepsilon^*_{\mathrm{y}} = 6$–$8$ μm in good injection conditions.

Beam intensity and vertical beam size are reduced by scraping with a vertical collimator. After collimation the emittances are $\varepsilon^*_{\mathrm{x}} = 6$–$8$ μm and $\varepsilon^*_{\mathrm{y}} = 3$–$5$ μm and a

typical beam intensity is 5×10^{11} protons.

After the preparation, one of the two crystals is positioned at a horizontal distance of typically 10 mm from the central orbit. This distance corresponds to about 10 times the RMS beam size and only few halo particles are found to hit the crystal. After this, the beam is excited horizontally with random kicks given by electrostatic deflector plates. As a result of the excitation the horizontal beam size increases and the protons diffuse towards the crystal. When the protons first arrive at the crystal, the horizontal emittance is typically $\varepsilon_{\mathrm{x}}^{*} = 60\,\mu$m. The vertical emittance remains almost unchanged. After the beam is blown up measurements are usually started with horizontal alignment scans ('angular scans'), during which the crystal angle is changed once every SPS cycle in order to align the crystal planes with the particles in the beam halo. Beam excitation is continued during measurements to obtain a steady flux of particles to the crystal.

During the measurements, the time unit for synchronizing different actions such as rotating the crystal or reading the detectors is the 14.4-s-long SPS super cycle. The super cycle is used in cycling mode as a time unit during which particles are injected, accelerated and extracted. The timing signals of the super cycle provide the timing framework for the data acquisition.

5.3 Beam excitation at the SPS

Because of the long SPS beam lifetime and slow diffusion rates it is necessary to excite the beam during experiments to make beam particles hit the crystal.

For a precise extraction efficiency measurement a continuous flux of particles on the crystal is needed. For the efficiency measurement one has to count the number of particles lost from the SPS and the number of particles extracted. For a precise measurement of the loss rate the beam lifetime has to be short enough, and for the counting of extracted particles, the extraction rate has to be low enough to avoid saturation of the counters. For these reasons a good beam excitation method has to provide a steady and continuous flux of particles, and it also has to allow control of the number of particles arriving at the crystal.

Different beam excitation methods have been used, each having their advantages and disadvantages.

5.3.1 Kick mode

The first method used to bring the beam towards the crystal was the so-called 'kick mode'. This mode was chosen for the first measurements because of its simplicity, in order to give a signal of extraction and to show that it is possible to align the crystal with the SPS beam.

In the kick mode a fast kicker magnet (rise time ~ 100 ns) is energized in the time taken for one SPS revolution (23 μs) to deflect the whole beam horizontally towards

the crystal by about 100 μm or more at the crystal location (see Fig. 4.3).

The main advantage of the kick mode is that it is easy to obtain large impact parameters and to overcome the inefficient surface layer. After a kick, a time structure in the extracted beam is observable. By using the time structure it is possible to study extraction at different passes in the crystal [43, 76].

However, there are also disadvantages with this method. When a sizeable fraction of the circulating beam hits the crystal, there can be very high instantaneous rates in the detectors measuring the extracted beam intensity. Owing to saturation of the detectors it is difficult to count the extracted particles. Also, it is not easy to determine the number of particles lost from the SPS because the lifetime measurement system needs several turns in the accelerator to be able to make a precise measurement of the SPS beam intensity. These problems make it difficult to perform a reliable extraction efficiency measurement in the kick mode. Furthermore, the kick mode cannot be considered as a parasitic method of extraction and thus is less interesting for future applications.

5.3.2 Excitation with transverse noise

The most commonly used beam excitation method in the crystal assisted extraction experiments has been random horizontal kicks [44] given by the electrostatic deflector plates of the SPS transverse feedback system ('damper' system) [45]. Bandwidth-limited white noise generated by an external noise generator is coupled to the power amplifiers of the damper plates. The noise applied to the beam can be considered as a series of uncorrelated random kicks that make the beam particles diffuse towards the crystal.

Theoretical emittance growth

The transverse kick given to the circulating protons at each passage through the damper plates is

$$k = \frac{l\,U}{d\,\gamma\,E_0}, \tag{5.1}$$

where l is the length of the plates, U the voltage between the plates, d the distance between the plates, γ the relativistic Lorentz factor and E_0 the proton rest energy.

In the SPS the damper plates are 2.4 m long and there is a gap of 14.2 cm between them. The noise generated by the noise source has been studied and the results are shown in Ref. [46]. The amplification of the noise signal when it is connected to the power amplifiers of the damper plates has also been measured [46] making it possible to calculate kick strengths corresponding to different noise generator settings.

The emittance growth owing to a series of random independent kicks can be calculated using the formula [47]

$$\langle \Delta\epsilon \rangle = \frac{1}{2}\,\beta_{\mathrm{d}}\,\langle k^2 \rangle, \tag{5.2}$$

where β_{d} is the value of the beta function at the damper location (about 72 m in the SPS experiment) and k is the kick strength. The rate of emittance growth as a function of kick strength is

$$\frac{\langle \Delta\varepsilon \rangle}{\Delta t} = \frac{1}{2}\,\beta_{\mathrm{d}} \langle k^2 \rangle f_{\mathrm{rev}}, \tag{5.3}$$

where f_{rev} is the revolution frequency of the protons in the SPS (43 375 Hz). By combining Eqs. (5.1) to (5.3), the emittance growth can be expressed as

$$\frac{\langle \Delta\epsilon \rangle}{\Delta t} = \frac{\beta_{\mathrm{d}}\, f_{\mathrm{rev}}\, l^2}{2d^2}\,\frac{\langle U^2 \rangle}{\gamma^2 E_0^2}. \tag{5.4}$$

When the beam is excited with transverse noise the diffusion speed of the particles is constant and can be adjusted by changing the noise amplitude. With transverse noise the diffusion speed is also independent of particle amplitude. This is different from the case when the particle moves under the effect of nonlinear fields. With nonlinear fields, the diffusion speed depends on the particle amplitude and typically the diffusion speed is much higher for large amplitude particles than for small amplitude particles.

Emittance growth measurements in the SPS

The rate of emittance growth was measured in the SPS for two different noise amplitudes (kick strengths) [86]. The beam emittance was measured with wire scanners during the diffusion process and results are shown in Fig. 5.3. It can be seen that during beam blow-up a steady equilibrium state is reached where the emittance grows linearly as a function of time, as expected from Eq. (5.3).

The emittance growth measurements are compared with predictions in Fig. 5.4. The two points are the measurements shown above and the solid line is the prediction obtained from Eq. (5.3). A very good agreement is obtained between the measurements and the prediction, which gives confidence that the method of beam excitation with white noise is well understood and well under control.

Kick strengths used in the SPS are typically between 1 nrad and 10 nrad. Some frequently used noise attenuation values together with the RMS voltages between the deflector plates and the kick strengths are shown in Table 5.1.

Advantages and disadvantages with transverse noise excitation

Beam excitation with transverse noise has several advantages compared with other methods. The diffusion of the particles can be well controlled and by changing the noise amplitude the diffusion speed and the resulting impact parameters can be changed. The

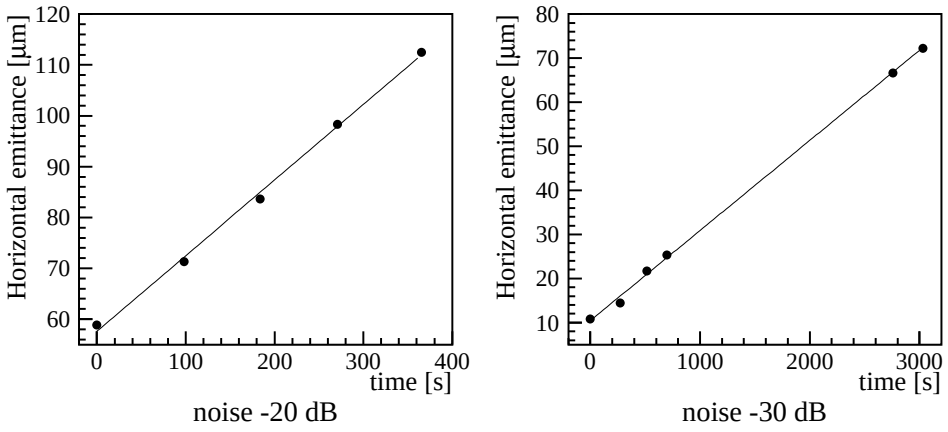

Figure 5.3: Emittance growth as a function of time for two different noise amplitudes.

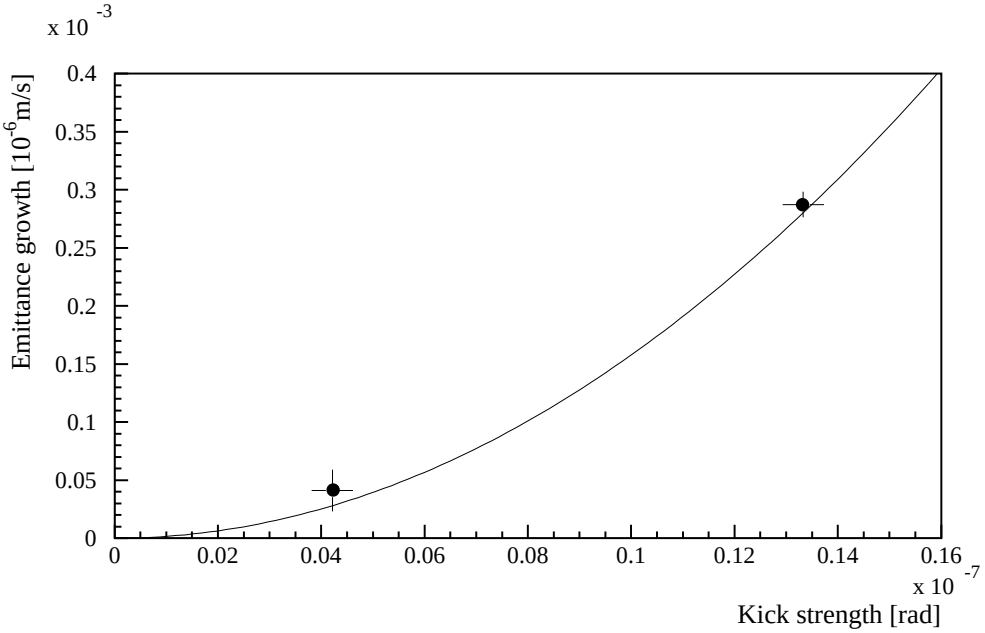

Figure 5.4: Two emittance growth measurements compared with the prediction (solid line).

diffusion is continuous and steady which makes it suitable for detailed measurements in well defined conditions. Also the instantaneous rates can be kept low so that saturation of the detectors is not a serious problem. A further, important advantage is that the diffusion process can be easily simulated when the kick strength is known, which makes it possible to estimate the impact parameter distribution.

Table 5.1: Typical noise attenuation values used with a 'Wavetek' noise generator, corresponding RMS voltages between damper plates and resulting RMS kick strengths used for beam excitation in the SPS.

Noise attenuation [dB]	Voltage U_{plates} [V]	Kick strength [nrad]
-25	53.2	7.5
-30	29.9	4.2
-35	16.8	2.4
-40	9.5	1.3

The main disadvantage of the method is that the impact parameters are small, typically less than 1 μm. In principle, larger impact parameters could be obtained with larger kick strengths, but this is limited by very short beam lifetimes.

5.3.3 Beam excitation with nonlinearities and tune ripple

A beam excitation method that can create large impact parameters on the crystal is introducing a strong nonlinearity in the accelerator by using, for example, sextupole magnets. If at the same time the tune is modulated this may lead to chaotic motion for particles at large betatron amplitudes. In the presence of nonlinearities and tune modulation, the diffusion speed in the beam tail and the resulting impact parameters can be much larger than with transverse noise excitation. However, the behaviour of the particles in the beam tail is not well understood and it is difficult to reliably simulate extraction under these conditions.

5.4 The bent crystals

Several different crystals have been used in the extraction experiments at the SPS (Table 5.2). The crystals used can be divided into two groups depending on the way they are bent: first crystals (ST1–ST3 in Table 5.2) and U-shaped crystals (GR1–GR5). The differences between these crystals are explained in later sections.

All the crystals are made of silicon and are cut parallel to the (110) plane. Silicon crystals are used because of their high quality, mechanical properties and easy availability. The total bending angle of all the crystals is 8.5 mrad over their lengths of 30 or 40 mm.

Table 5.2: The crystals used in the SPS.

Crystal label	Position in the SPS	Date of installation	Date of removal	Further information
ST1	1	5 Feb. 1992	24 Feb. 1994	Stuttgart Nr.412
ST2	2	5 Feb. 1992	3 March 1993	Stuttgart Nr.413
GR1	2	3 March 1993	22 June 1993	'bridge'-type bender
GR2	2	22 June 1993	–	U-shaped (1.5 mm thick)
ST3	1	24 Feb. 1994	2 March 1995	ST2 with amorphous layer
GR3	1	2 March 1995	28 June 1995	U-shaped (3.5 mm, round edges)
GR4	1	28 June 1995	3 June 1996	U-shaped (3.5 mm, sharp edges)
GR5	1	3 June 1996	–	U-shaped (1.5 mm, known miscut)

5.4.1 Crystal preparation and quality

The quality of the crystal lattice is very important in high-energy channeling. Bending experiments in external beams [34, 35] have shown that silicon crystals can have a very high deflection efficiency.

In beam extraction with a crystal, the surface quality of the crystals has to be very good. The crystals have to be cut parallel to the (110) plane as precisely as possible. However, a small angle between the surface and the crystal planes cannot be avoided. This angle, called the miscut angle, can have two directions as shown in Fig. 5.5. In the first case (positive miscut angle), the particles that arrive from the left can propagate the whole length of the crystal trapped between crystal planes for any impact parameter. However, in the second case (negative miscut angle) the particles that arrive at the crystal very close to the crystal surface are led out of the crystal before they have passed through the whole crystal length. With a negative miscut angle, part of the beam may experience a smaller bending angle and be lost from the deflected beam. For this reason negative miscut angles should be avoided by cutting the crystal with a deliberately positive small miscut angle.

After the cutting, the crystal surface is etched and polished to obtain a very small surface roughness and to make the surface reflective for laser measurements.

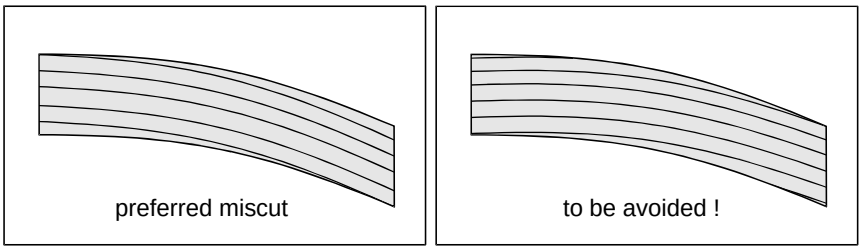

Figure 5.5: Two types of crystal miscut. The crystal on the left has a preferred positive miscut angle and the one on the right a negative miscut angle that should be avoided.

5.4.2 The first crystals

The first crystals (ST1–ST2 in Table 5.2) used in the SPS experiments were made at the Max Planck Institut für Metallforschung in Stuttgart, Germany. The dimensions of these crystals are 30 mm × 18 mm × 1.5 mm (length × height × thickness). An example of such a crystal is shown in its bending device in Fig. 5.6. This type of bending device is known as a 'bridge'-type bender. The central 10 mm of the crystal height are left free from the bender material (stainless steel). The crystal is clamped in the bender and the bending angle is adjusted by turning a differential screw.

When the crystal slab is bent in the beam direction, it also experiences torsion in the transverse (vertical) direction: the direction of the planes at the ends of the crystal varies as a function of vertical position. This unwanted twist is called 'anticlastic bending' [48, 49].

The bending of these crystals was studied by laser light reflection and the results are shown in the lower part of Fig. 5.6. The first plot shows that the bending along the beam direction is fairly uniform, but the second plot clearly indicates the anticlastic bending. The direction of the crystal planes varies by about 200 μrad over a distance of 3 mm. This variation is significant when compared to the expected angular divergence (RMS less than 5 μrad, see Fig. 6.1) of the incoming beam at its first hit in the crystal.

The fact that the direction of the planes changes with the vertical coordinate means that the optimal alignment of the crystal with respect to the beam depends on the vertical position where the particles hit the crystal. A direct measurement was obtained by moving the SPS beam vertically at the crystal entrance (see Section 7.1.2).

The miscut angles of these crystals are smaller than 200 μrad and were measured with a precision of about 100 μrad. The crystals were cut with a deliberately positive miscut angle.

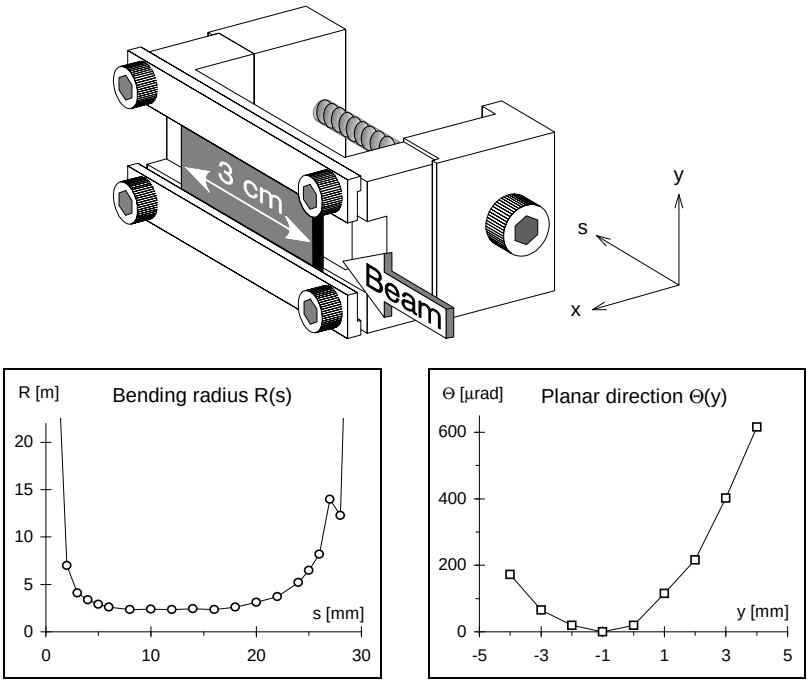

Figure 5.6: An example of the first crystals in its bending device (bridge-type bender). The lower part of the figure shows the bending of the crystal along the beam direction and the change of planar direction along the vertical coordinate (anticlastic bending).

5.4.3 U-shaped crystals

In order to overcome the unwanted transverse bending of the first crystals, the U-shaped crystals were introduced. A U-shaped crystal (Fig. 5.7) is not just a silicon slab but is cut as one piece including its legs. The differential screws that bend the crystal are attached to the legs. The legs of the U-shaped crystal prevent it from twisting at the ends of the crystal, thus almost completely eliminating the anticlastic bending.

The primary and anticlastic bending for a 1.5-mm-thick U-shaped crystal can be seen in the lower part of Fig. 5.7. The measurements with reflected laser light show that the anticlastic bending is much smaller than with the first crystals. Measurements with a 3.5-mm-thick U-shaped crystal [50] show slightly more anticlastic bending, but still the effect is very small compared to the first crystals.

The U-shaped crystals were made at the European Synchrotron Radiation Facility (ESRF) in Grenoble, France [51, 52]. Different U-shaped crystals have been used in the SPS experiments (GR2–GR5 in Table 5.2). All these crystals have a length of 40 mm and a height of 20 mm. Two different thicknesses (1.5 mm and 3.5 mm) have been

used. Most measurements have been performed with a 1.5-mm-thick crystal (GR2), but to study the effect of crystal thickness, a 3.5-mm-thick crystal (GR3) was prepared. This crystal had rounded (broken) edges and therefore was later replaced with a crystal (GR4) with sharp edges.

These crystals were cut with miscut angles smaller than 100 μrad. However, the direction of the miscut was not known. To study the effect of the miscut, a crystal (GR5) was prepared with a known positive miscut angle of about 1 mrad [52].

After the cutting, these crystals undergo a series of surface etching and polishing phases. The final surface quality is obtained by mechano-chemical polishing known as the Syton technique [53], which is done with a chemical on a nylon cloth pressed and rubbed against the crystal surface. In this way an optically flat surface is obtained, which makes it possible to use laser light reflection for measuring the bending and alignment of the crystals.

After the surface treatment the roughness of the surface was measured and found to be less than 50 Å [52]. However, as a side-effect of the polishing the crystal surface is not completely flat but has a round shape. The surface non-flatness amounts to a 'bump' with a height of about 2.5 μm over the 40-mm-long crystal [52].

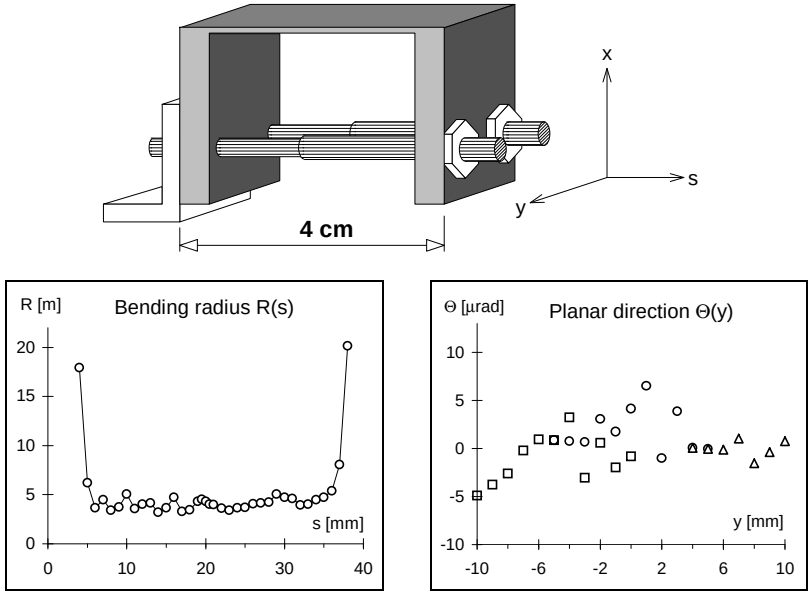

Figure 5.7: U-shaped crystal. The lower part of the figure shows the bending of the crystal along the beam direction and the change of planar direction along the vertical coordinate.

5.4.4 Installation of the crystals at the SPS

A schematic drawing of the SPS vacuum tank at the crystal location is shown in Fig. 5.8. Two bent crystals in their bending devices are installed on goniometers that can both move the crystals horizontally in and out of the beam and rotate the crystals in the horizontal plane to align them with the beam particles. The minimum possible step size for crystal movement is 0.05 mm and for the angular alignment 2 μrad. The available range for movement is 90 mm and for rotation about 8 mrad. The movement and rotation of the crystals are controlled with stepping motors, which means that the expected reproducibility is very good.

The crystals can be prealigned with the SPS beam by means of laser beams reflected from the crystal surface [54, 55]. The principle of the alignment system is shown in Figs. 5.8 and 5.9. A laser table equipped with mirrors (M) and beam splitters (BS) brings two laser beams to the upstream and downstream ends of the crystal. The laser light reflected by the crystal surface is measured with two position sensitive detectors (PSD_u for upstream and PSD_d for downstream laser beams). The upstream laser beam is used to prealign the crystal with the SPS beam and to monitor the crystal alignment during experiments. The downstream laser beam can be used to monitor a change in the bending angle of the crystal.

The crystals that were prealigned with the laser system were found to be well aligned within the angular range of the goniometers (8 mrad). This allows the final alignment of the crystals to be carried out during the measurements by rotating the crystals and observing the intensity of the extracted beam.

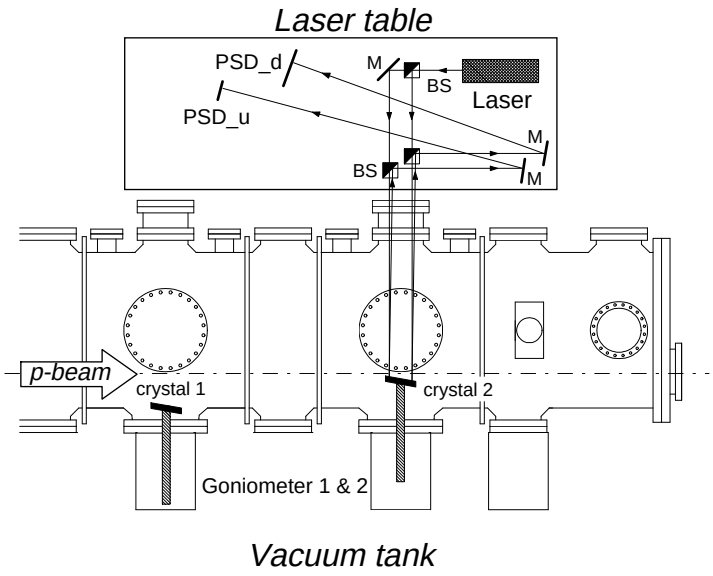

Figure 5.8: The SPS vacuum tank at the crystal location (for details see text).

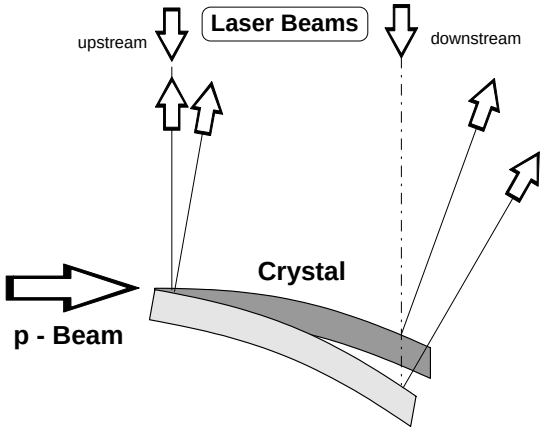

Figure 5.9: The principle of crystal alignment using reflected laser beams.

5.5 Detection of extracted beam

The characteristics of the extracted beam are measured with a set of detectors placed along the extracted beam line downstream of the crystals (Fig. 5.2). Three scintillators (S1, S2 and S3) are used in coincidence for triggering the hodoscope and the FInger SCintillator (FISC). A scintillating screen gives an image of the extracted beam. The hodoscope, FISC and scintillator S3 are mounted on a table that can be moved horizontally and vertically to the position of the extracted beam. The properties of these detectors are explained in more detail in the following sections.

In addition, there are two 10 cm^2 scintillators positioned 5 m downstream of the exit window. One of these scintillators is in the extracted beam line and the other outside the SPS ring to measure the background rates. The two scintillators are called internal and external, respectively.

During the first experiments there were two pairs of Micro-Strip Gas Chambers (MSGCs) but they were later replaced by the FISC. The MSGCs had a spatial resolution better than 100 μm and were used to measure the extracted beam profiles and divergences with high precision.

5.5.1 Scintillating screen

A scintillating screen (TV in Fig. 5.2) is used to provide an online image of the extracted beam. The scintillating CsI (Cesium Iodide) screen is read by a CCD camera giving a two-dimensional picture of the extracted beam [56]. The picture is shown on a TV screen in the SPS control room. The information on the scintillating screen can also be digitized into, for example, 0.2×0.2 mm^2 pixels and stored for offline analysis.

The screen has been very useful during the experiments because it makes it possible to continuously monitor the position, size and shape of the extracted beam. With the screen the fluctuations in the extracted beam intensity can be seen clearly and it has proven to be a valuable beam diagnostic device in the setting up of the accelerator for the experiments.

5.5.2 Hodoscope

The hodoscope consists of 32 horizontal and 32 vertical adjacent scintillator strips in two planes [57]. Each strip is 1 mm wide and 32 mm long and thus the total area of each hodoscope plane is 32×32 mm^2. The horizontal and vertical strips give the vertical and horizontal beam profiles, respectively. The two hodoscope profiles are displayed online on a workstation screen in the SPS control room. Each of the scintillator strips can count the traversing protons with a maximum rate of the order of 10 MHz, i.e. a profile can be precisely measured in one second.

The detection efficiency ϵ_{H} of the hodoscope has been studied (see Refs. [58, 81]). The results indicate that the efficiency is rather high, $\epsilon_{\mathrm{H}} \simeq 98\%$.

5.5.3 Finger scintillator

The FInger SCintillator (FISC) is a 5-mm-long vertical finger-shaped scintillator. It is moved with a stepping motor in the horizontal direction so that it measures the horizontal profile of the extracted beam. In the beginning, the thickness of the FISC scintillator was 1 mm and it was moved by the stepping motor in steps of 1 mm. In this mode, the FISC was mainly used to check the calibration of the vertical hodoscope strips. Later the scintillator was replaced by a 0.2-mm-thick one, and the movement of the stepping motor was also reduced to steps of 0.2 mm. The reduction of the scintillator thickness and step size made it possible to measure the horizontal beam profiles with better precision.

The FISC profiles are shown in the SPS control room on the same display as the hodoscope profiles. The motor moving the FISC can be programmed to make scans of variable length and step size so it offers more flexibility than the fixed hodoscope. Usually the FISC movement and read-out are programmed in such a way that it gives a beam profile every 14.4 s, i.e. at the same rate as all other data is recorded.

5.5.4 Trigger scintillators

Three scintillation counters (S1, S2 and S3) are used in coincidence as a trigger for the hodoscope and FISC. The triple coincidence rate can also be used to measure the flux of particles coming from the crystal. The scintillator S1 is round and has a diameter of 5 cm. The sizes of S2 and S3 are 10×10 cm^2 and 5×5 cm^2, respectively.

The three scintillators give clean peaks in pulse height for minimum ionizing particles. This makes it possible to reject multi-particle events by using the coincidence $\mathrm{S1} \times \mathrm{S2} \times \mathrm{S3} \times \overline{\mathrm{S3}}$ as the trigger instead of $\mathrm{S1} \times \mathrm{S2} \times \mathrm{S3}$, where $\overline{\mathrm{S3}}$ denotes veto with large S3 signals. The anti-coincidence $\overline{\mathrm{S3}}$ makes it possible to reject multi-particle events that are mainly due to interactions in the crystal.

The detection efficiencies ϵ_d of the individual trigger scintillators have been studied and found to be high, $\epsilon_d > 99\%$ (see for example Refs. [58, 81]). However, when the anti-coincidence is used, the estimation of detector efficiencies is more difficult. The efficiency of the anti-coincidence $\epsilon_{\overline{\mathrm{S3}}}$ depends on the pulse height of the S3 scintillator and on the setting of the high discrimination threshold. The highest value for $\epsilon_{\overline{\mathrm{S3}}}$ has been $\simeq 93\%$. It was sometimes estimated to be lower when, for example, the pulse height of S3 had changed [81]. Because of the difficulty in measuring $\epsilon_{\overline{\mathrm{S3}}}$ precisely, the anti-coincidence was used only during some of the early experiments and most of the measurements have been performed without it.

5.6 The data acquisition system

The data acquisition system provides measurement data both for online monitoring and for offline analysis. Some data read out by the system is shown online in the SPS main control room during measurements. This data is updated every SPS cycle (14.4 s), which makes it possible to inspect some results immediately and to decide how to proceed with the measurements. All the data is written in data structures that are saved for offline analysis.

The experiment is controlled from the SPS main control room. It is located at a distance of about 2 km from the data acquisition hardware. Therefore it is necessary to have a system that allows easy connection between the microprocessors of the read-out hardware and the workstations in the control room.

The timing of the data acquisition is synchronized with the operation of the SPS accelerator by using the 14.4-s-long SPS super cycles. The SPS is usually operated in coast mode during measurements, which means that there is a continuous beam of particles in the machine. Nevertheless, the SPS super cycles provide a useful timing framework to synchronize different actions and all the data is measured and saved once every super cycle. The gate length for data reading is usually 5 s at the beginning of the super cycle, after which the data is sent to the SPS control room. During the data sending and before the start of the next super cycle other actions can be taken such as changing the crystal angle during an angular scan.

A logical description of the data acquisition system is given here. A more detailed and technical description can be found in Ref. [59]. Information about the hardware and VME software can also be found in Ref. [60].

5.6.1 Data acquisition hardware

The detectors are installed in the SPS beam tunnel about 80 m below ground level. To avoid exposure to radiation during SPS operation and to allow easy access most of the electronics are in the former UA1 control room at ground level. The electronics consist of four racks with VME, CAMAC and NIM modules [60]. There are also high-voltage sources, high-voltage dividers, patch panels and the detector table control in the same racks. The choice of the three electronics standards was dictated by the availability of previously used CAMAC and NIM modules.

By using a processor module in a VME crate it is possible to have an independent real-time computer running a UNIX-like operating system. The operating system used is OS9. The modules in the CAMAC crate are discriminators, prescalers and scalers. From a program running in a VME processor module it is possible to control CAMAC modules and read data from CAMAC scalers. In NIM crates there are coincidence units, signal converters and delay modules. The main purpose of the NIM modules is to provide coincidences between scintillator signals.

The signals from photomultipliers are discriminated, prescaled and counted in the

CAMAC modules. The working principle of the scintillator read-out electronics is shown in Fig. 5.10.

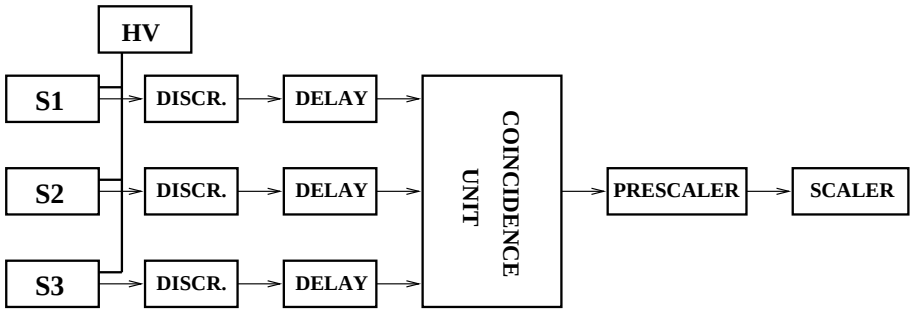

Figure 5.10: The working principle of the scintillator electronics.

5.6.2 Data acquisition software

The general structure of the data acquisition software is shown in Fig. 5.11. It consists of programs running in the VME crate that control measurements, read data and send the measured data in MOPS data structures across Ethernet and token ring networks to workstations in the SPS control room. In the workstations the data is displayed online and saved for offline analysis.

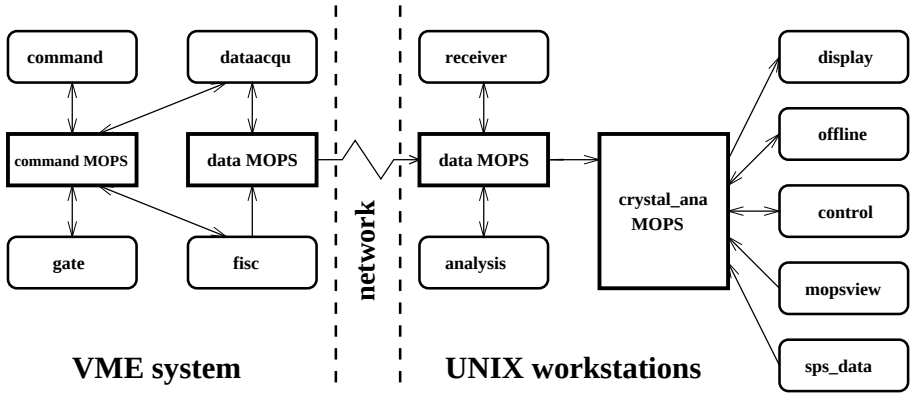

Figure 5.11: Structure of data acquisition software.

5.6.3 MOPS data structures

The data collected during crystal extraction experiments is saved in data structures called MOPS (Multiple Object Partitioned Structure) [61, 62]. The MOPS data structure management system is a set of service routines which make it possible for the users

to organize and manage their data in a structured way. MOPS was developed at CERN and it has been used in many applications running in different computer systems. It is possible to use MOPS from both FORTRAN 77 and C programs and the underlying data structures are the same so it is possible to share data between programs written in these languages. A MOPS data structure can also be sent across a network using sockets with TCP/IP communications protocol.

In MOPS terminology a data structure is a collection of data, a description of the data and the logical relations between data items [61]. The data structures are physically located in a contiguous part of the memory called the 'dynamic store'. A MOPS data structure is mapped onto this dynamic store.

The MOPS data structures consist of objects. An object is a collection of similar data elements that are grouped together and stored in contiguous memory locations in the dynamic store. The elements can be simple data items like integers or more complicated collections of data like C structures or other MOPS data structures.

The MOPS system provides a number of routines and tools to create, access and manipulate the data structures. The possibility of accessing the MOPS objects via a keyword instead of variable or array names makes it easier to write simple, maintainable and portable programs at the expense of a small time overhead.

The data acquisition system uses three MOPS structures: *commandMOPS*, *dataMOPS* and *crystal_ana*.

commandMOPS contains measurement parameters like gate length and prescaler factor, and commands given to the data acquisition system.

dataMOPS contains the measured data coming from scintillators, the hodoscope and the FISC. Parameters concerning the measurement and the state of the SPS are also saved in *dataMOPS*.

crystal_ana is made by combining data from 200 *dataMOPS* structures in one larger MOPS. The measurement data is saved on the disk and analysed offline by using *crystal_ana* structures.

A detailed description of the crystal extraction MOPS structures is given in Ref. [63].

5.6.4 VME software

The software used in the VME system can be seen on the left side of Fig. 5.11. The software is run under the UNIX-like real-time operating system OS9.

The purpose of VME programs is to make one measurement during each SPS cycle. At the beginning, the programs set the measurement parameters, such as voltage thresholds, for the discriminators and prescaler factors. Then the programs control the timing of the read-out and read data from the scalers. After that the data and the

measurement parameters are saved in a MOPS data structure which is sent across the network to a workstation.

command program

The *command* program allows the user to set different measurement parameters and give commands to the data acquisition system. The program presents a menu from which the user can select a parameter to be changed. After the change, the parameters are written into the *commandMOPS*-data structure. Other programs read parameters from *commandMOPS* and perform a measurement according to these parameters. The command program also issues a warning if one of the other programs has stopped or if an error has occurred in the data acquisition system.

dataacqu program

The *dataacqu* program is a central part of the data acquisition software. At the start of the measurements, it creates the two MOPS data structures (*commandMOPS* and *dataMOPS*) if they do not already exist. It also initializes the CAMAC scalers and sets threshold voltages and prescaler factors. After that the program reads measurement parameters from the *commandMOPS* and, depending on the parameters, starts a measurement. When the measurement is finished *dataacqu* reads the scalers and saves the data in *dataMOPS*. After that the *dataMOPS* is sent across the network to a workstation.

gate program

The scalers in CAMAC crates are used to count the signals from photomultipliers during a time interval whose length is given in the *command* program. This time interval, i.e. the gate, is defined by the *gate* program.

FISC program

The FISC is a scintillator moved by a stepping motor and read by a scaler in the VME crate. The *FISC* program has to control the movement of the stepping motor, read the counting rate from the scaler and save data in *dataMOPS*.

5.6.5 Workstation software

The programs that are run on HP workstations are shown on the right side of Fig. 5.11. These programs receive data from the VME system and save the data in a MOPS data structure (*crystal_ana*) that is stored for offline analysis. The incoming data is also displayed online.

receiver program

The *receiver* program waits for the *dataacqu* program in the VME system to send measurement data. When the *receiver* program receives a new *dataMOPS* from the VME it creates a *dataMOPS* structure in the workstation memory if one does not already exist. After that the *dataMOPS* is copied to the workstation or an existing *dataMOPS* is overwritten. The receiver program also shows whether errors have occurred during data transfer.

analyse program

The *analyse* program reads the *dataMOPS* written by the *receiver* and saves the data in a bigger MOPS structure called *crystal_ana*. Each *dataMOPS* contains one event, i.e. data from one SPS cycle lasting 14.4 s. The *analyse* program collects data from two hundred events in *crystal_ana*, after which it saves the MOPS on a workstation disk as one file.

Display program

The *display* program shows the data coming from the VME system online in the SPS control room.

An example of such a display can be seen in Fig. 5.12. In the top part of the display horizontal and vertical extracted beam profiles measured with the hodoscope are shown. Below that, there are two horizontal profiles measured with the 0.2-mm-thick FISC scintillator. In the first FISC profile, background correction is made using the trigger counting rate, whereas the second case shows the raw data. In the display in Fig. 5.12 the FISC was moved in 0.2 mm steps over a distance of 10 mm. In the lower part of the display, the extracted beam intensity measured with scintillator coincidence is shown as a function of time. The two peaks in the extracted beam intensity correspond to two angular scans made with two different step sizes. The angular scans indicate the optimal alignment of the crystal, and after the scans the crystal is put in the optimal alignment for extraction efficiency measurement.

Other programs

The *sps_data* program reads data describing the SPS conditions during the experiment. The data that is read includes positions of four scrapers, positions and angles of the two crystals, and the proton beam intensity.

The *mopsview* program can be used during data-taking to extract numbers from the incoming MOPSes. Each time a new *dataMOPS* is received, *mopsview* reads and prints counting rates of all the scintillators and coincidences. Also the sums of the hodoscope horizontal and vertical strips can be shown.

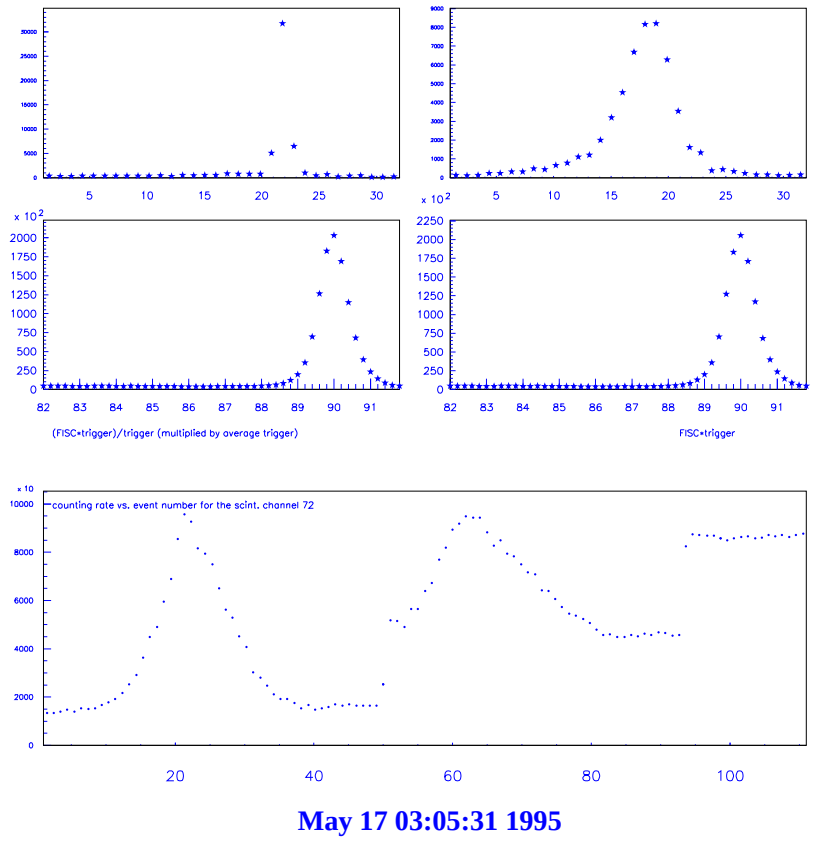

Figure 5.12: Online display. Horizontal and vertical profiles measured with the hodoscope are shown in the top part. Below that, there are two horizontal profiles measured with the FISC. In the lower part, the extracted beam intensity is shown as a function of time. For more details see text.

control and *offline* programs read the data saved in *crystal_ana* and provide tools for controlling the quality of measurements, viewing the data and perfoming simple data analysis.

5.7 Beam lifetime measurement

In our experiment it is necessary to know the beam lifetime and beam intensity which are used to determine the number of protons lost from the SPS beam per time unit in order to calculate the extraction efficiency.

Beam intensity measurement system

The SPS beam intensity is measured with a Beam Current Transformer (BCT). A BCT is a transformer that can be used to determine the electric current that a beam constitutes. A BCT signal is read by using the BOSC system [64, 65]. A medium- or high-sensitivity BCT is used depending on the SPS beam intensity.

The programs and data structures used in beam intensity measurement are shown in Fig. 5.13. A program called *lifetime* sends a measurement request across the network to the BOSC system using sockets with TCP/IP protocol. The server process in the BOSC system receives the request and passes it to a measurement process. After the measurement is complete, the data is sent back to the *boscd* server process running in a workstation. The *boscd* process receives the data and signals the *lifetime* program that new data has been received. After this, the *lifetime* program reads the data from *lifet_meas*-MOPS, saves it in a bigger *life_history*-MOPS and starts a new measurement. The lifetime measurement is synchronized with the 14.4-s-long SPS cycles. Each *lifet_meas*-MOPS contains data measured during one SPS cycle. Data from two hundred SPS cycles is collected in a *life_history*-MOPS, after which the MOPS is saved on the workstation disk.

Precision of lifetime measurement

The precision of the SPS beam intensity measurement is very important for an accurate extraction efficiency calculation. A typical measurement is performed by averaging the measured SPS beam intensity over 300 000 turns in the accelerator. The revolution time of the protons in the SPS is 23 μs, which means that one intensity measurement takes about 6.9 s. The measurement time is limited by the length of the SPS cycle (14.4 s), during which a measurement has to be performed, the data has to be sent across the network and a new measurement has to be started.

The working range of the medium-sensitivity BCT is between 2×10^9 and 4×10^{12} protons per beam [66]. A typical beam intensity during experiments is 5×10^{11} protons, which is well inside the working range of the BCT. When the beam lifetime is not very long (less than twenty hours) the fluctuations between measured points are small and the averaging over 300 000 turns gives a small statistical error for the beam lifetime measurement. However, the precision of the beam intensity reading is limited. The beam intensity reading obtained from a BCT is calibrated during every experiment by reading a calibration signal corresponding to 5×10^{11} protons. The calibration gives a BCT offset value (signal without beam) and a peak value corresponding to the calibration peak height. By using the offset and peak values it is possible to calculate from the BCT signal the number of particles in the SPS beam. A rather conservative systematic uncertainty of 10% is taken into account in the beam intensity measurement because of possible inaccuracies in the calibration procedure and slow fluctuations in the BCT offset value.

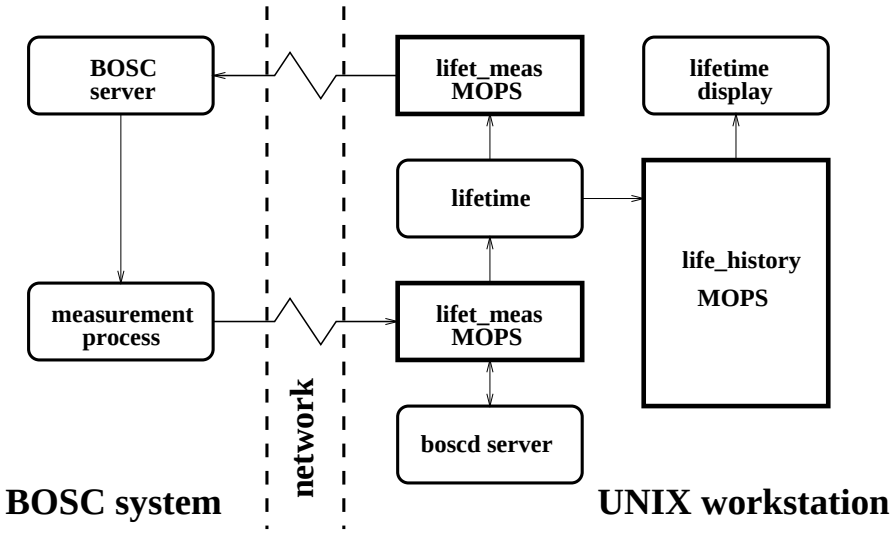

Figure 5.13: Beam intensity measurement system.

Lifetime calculation and display

The beam intensities measured with a BCT and stored in *life_history*-MOPS can be displayed online by the *life_disp* (lifetime display) program. An example of a lifetime display is shown in Fig. 5.14. The beam intensities measured once every SPS cycle, i.e. every 14.4 s, are displayed for the last 50 cycles. The lower part of the figure shows beam lifetimes and loss rates calculated from the intensity measurements, assuming an exponential decay of beam intensity according to

$$I(t) = I_0 e^{-t/\tau}, \tag{5.5}$$

where τ is the lifetime, $I(t)$ is the beam intensity at time t and I_0 is the initial beam intensity.

Equation (5.5) describing intensity decay is not linear but can be linearised by taking the logarithm of both sides of the equation, which gives

$$\ln I(t) = \ln I_0 - t/\tau. \tag{5.6}$$

The beam lifetime τ can be determined from the linearized Eq. (5.6) by making a linear fit using the method of least squares.

The lower part of Fig. 5.14 shows the beam lifetimes in hours obtained by a linear fit using the two, four, six, etc. latest intensity data points. It can be seen that when only a few intensity values are used in the fitting, the lifetime values are not very accurate owing to fluctuations in the intensity measurement. When more data points are used, the fluctuations in the lifetime values decrease.

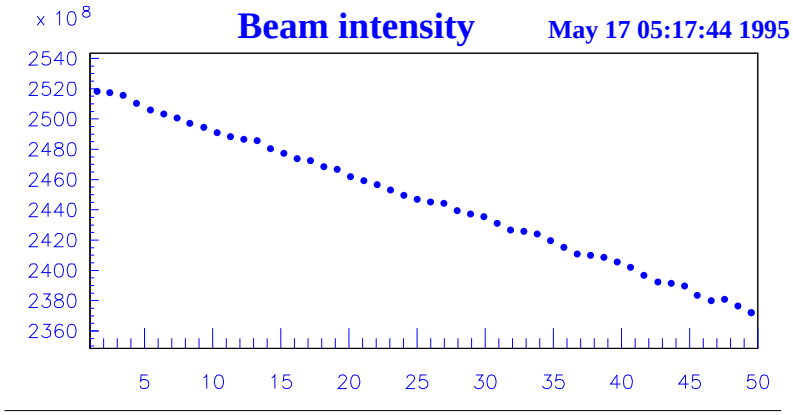

Number of SPS cycles	Beam lifetime (hrs)
2	2.300
4	3.374
6	3.073
8	3.271
10	3.118
12	2.964
14	3.093
16	3.105
18	3.075
20	3.116
22	3.112
24	3.125
26	3.168
28	3.205
30	3.225
32	3.234 +- .06

Loss rates (protons/sec)
16 cycles:
.214E+08 (+-.39E+06)
32 cycles:
.208E+08 (+-.36E+06)

Figure 5.14: Beam lifetime measurement display. SPS beam intensity is displayed as a function of time in the top part. Below that, the calculated SPS beam lifetimes are shown (for more details see text).

Chapter 6

Computer simulation model

The main purpose of the computer simulations is to get a better understanding of the crystal extraction process. By studying simulation results it is possible to obtain information, such as the number of passes that the particles have made through the crystal, which is not readily available from the experimental results. In addition to this, the simulations allow different accelerator and crystal parameters to be tested, which makes it possible to design new experimental installations.

In this chapter, the general structure of computer simulations is described and SPS parameters used in the simulations are shown first. After that, the simulation of beam diffusion is described and typical results are shown. Finally, the multi-pass simulations are explained and the behaviour of particles during multi-pass extraction is discussed. The results from multi-pass simulations such as angular scans and extracted beam profiles are shown together with experimental results in Chapter 7.

6.1 General structure of simulations

The simulation of crystal extraction can be divided into two independent parts:

1. Simulation of beam diffusion.
2. Simulation of interaction with the crystal and multi-pass process.

In the beam diffusion part the motion of the particles is simulated under the influence of some diffusion mechanism (here transverse noise) that makes the particles diffuse outwards in the transverse plane until they hit the crystal. At this moment the impact parameters and angles are recorded. The parameters for the diffusion mechanism (e.g. kick strength) can be varied and their effect on the impact parameter and angle distributions can be studied.

In the second part, the impact parameters and impact angles obtained from the diffusion part are used as initial coordinates for particles that interact with the crystal and are tracked around the accelerator until they are extracted or lost. By changing crystal or accelerator parameters their effect on the multi-pass process can be studied.

This division of the simulations provides a logical structure for the simulation programs and also allows the studies related to the beam diffusion mechanisms and to the

multi-pass process to be separated. The simulation of beam diffusion under realistic conditions is very time consuming; by separating it from the rest of the simulations it is possible to simulate the diffusion once and then re-use the impact parameter and angle distributions in the simulation of the multi-pass process where usually many runs are needed to study parameter dependence.

Earlier simulations of the SPS experiment are shown in Refs. [44, 67]. The simulation model shown here is based on programs described in Refs. [68, 69]. The simulation of beam diffusion in Ref. [68] produced a set of impact parameters and impact angles (Fig. 6.1) with kick strengths close to those used in the experiments. These impact coordinates are used as input for multi-pass simulations. Also the multi-pass simulations are mainly based on the program described in Ref. [68]. One of the changes made here is related to the channeling parameters which are now obtained from the equations in Chapter 3. The program was also changed to allow an easier input of parameters and the possibility of obtaining extracted beam profiles was added.

Other simulation programs have been developed [70, 71] where the particles are tracked through the crystal, and the interactions of the protons with the crystal lattice are treated in detail. The simulation program presented here is based on the channeling model described in Chapter 3 and confirmed in beam-line experiments. The main emphasis of the simulation in this thesis is on the understanding of the extraction process and on the effect of accelerator parameters, not on a detailed description of the channeling process. Another simulation program, in some respects similar to the program described here, has been developed in the context of Fermilab extraction experiments [72].

6.1.1 The SPS parameters

The SPS parameters that are used in the simulations are shown in Table 6.1. During crystal extraction experiments, the usual SPS lattice is used. The SPS lattice model and the MAD (Methodical Accelerator Design) program [73] are used to obtain the values of optical functions at damper and crystal locations.

In the multi-pass simulations, tune spread can be provided by small, random changes to the average tune values shown in Table 6.1. The tune values are modified each turn in the accelerator by $Q \rightarrow Q + \Delta Q$, where ΔQ is evenly distributed between, for example, -0.001 and $+0.001$. These are the values used in the simulation, and the tune spread of this magnitude has clear effects on the multi-pass behaviour of the particles (see Section 6.3.6).

6.2 Simulation of beam diffusion

The most commonly used method of creating beam diffusion during the crystal extraction experiments has been transverse noise (see Section 5.3.1), selected because it is

Table 6.1: SPS parameters that are used in the simulation.

Parameter	Symbol	Value
Particle energies	E	14,**120**,270 GeV
Horizontal tune	Q_{x}	26.62
Vertical tune	Q_{y}	26.58
Horizontal phase difference from damper to crystal	$\Delta\phi_{\mathrm{x}}/2\pi$	17.26
Optical functions at crystal	β_{x}	91.31 m
	β_{y}	23.74 m
	α_{x}	2.184
	α_{y}	-0.706
Optical functions at damper	β_{y}	72.70 m
	α_{x}	1.895
Initial normalized beam emittances (2σ)	$\varepsilon^*_{\mathrm{x}}$	10 μm
	$\varepsilon^*_{\mathrm{y}}$	10 μm

easy to simulate and provides a solid basis for comparing experimental and simulation results.

The simulation is started by creating the horizontal phase space of a beam at the crystal location with typically 10 000 particles and a normalized emittance (2σ value) of about 10 μm. The crystal is located at a distance of 6.2 mm from the closed orbit. With the initial emittance of 10 μm no particles can hit the crystal. The beam is transported to the location of the damper plates by using the matrix in Eq. (2.17). The beam transport is linear and assumes no coupling.

At the damper location, the particles are given a horizontal kick, i.e. the horizontal coordinates are changed according to

$$(x, x') \rightarrow (x, x' + k), \tag{6.1}$$

where k is the strength of the kick. The kick strengths have a Gaussian distribution with zero mean and a width σ_{kick} that determines the emittance growth rate according to Eq. (5.3).

After this, the particles are transported to the crystal location where the transverse coordinates are compared with the crystal position to test whether the particles hit the crystal. In case of a hit, the impact parameter and impact angle of the particle are recorded for later use, e.g. in multi-pass simulation. The particle that hits the

crystal is removed from the beam and replaced by another one from the initial beam distribution. The particles that do not hit the crystal are transported again to the damper where another kick is given. The simulation is continued until enough hits in the crystal are recorded. For further details see Ref. [68]. An example of impact parameter and angle distributions obtained by using a kick strength of $\sigma_{\mathrm{kick}} = 10$ nrad is shown in Fig. 6.1.

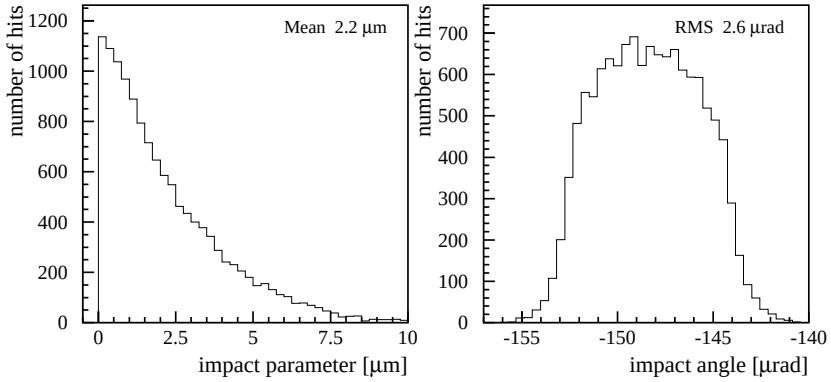

Figure 6.1: Impact parameter and angle distributions obtained from beam diffusion simulation ($\sigma_{\mathrm{kick}} = 10$ nrad.)

6.3 Simulation of multi-pass process

In the simulation of the multi-pass process the impact parameter and angle distributions obtained from diffusion simulation are used as initial coordinates of the particles at the crystal entrance face. In the diffusion simulation only the horizontal coordinate of the beam was affected, but in multi-pass simulation scattering in the crystal can also change the vertical coordinates and therefore the vertical phase space is created as well. During the experiments a coasting beam is used, i.e. the RF is switched off and the energy losses of the particles are not restored. Therefore there is no need to simulate the RF, but for the energy losses one more coordinate is required. Consequently, each particle has five coordinates in the simulation: x and x' for horizontal amplitude and angle, y and y' for vertical amplitude and angle, and ΔE for the energy difference from the nominal beam energy.

One particle at a time is selected from the initial coordinate distribution. Depending on the coordinates, the particle can hit the crystal in the inefficient surface layer or in the crystalline region. If the impact parameter is smaller than the layer thickness, or the impact angle is larger than the critical channeling angle, the particle experiences multiple scattering in the crystal material (Section 6.3.2). On the other hand, with

a large enough impact parameter and small enough impact angle the particle may be channeled in the crystal. In this case, there is a certain probability that the particle is channeled through the whole crystal (see Section 6.3.3). If the particle is channeled and extracted, it is used for the extracted beam profiles (Section 6.3.5).

The particle can be lost from the simulation, e.g. owing to nuclear interactions, and in this case a new particle is selected from the initial coordinate distribution. The possible reasons for particle loss are explained in Section 6.3.4.

If the particle is not extracted or lost, it is transported around the accelerator using the matrix in Eq. (2.17). If the particle arrives again at the crystal entrance face, it has another chance of being channeled or scattered.

6.3.1 Model of the crystal

The model of the crystal used in the simulations is shown in Fig. 6.2. The dimensions of the crystal are chosen to be close to the dimensions of the U-shaped crystals used in the experiments. The length of the crystal is 40 mm, and it has a 5-mm-long straight part. The thickness of the inefficient surface layer is varied in the simulations. The crystal is positioned at a distance of 6.2 mm from the closed orbit.

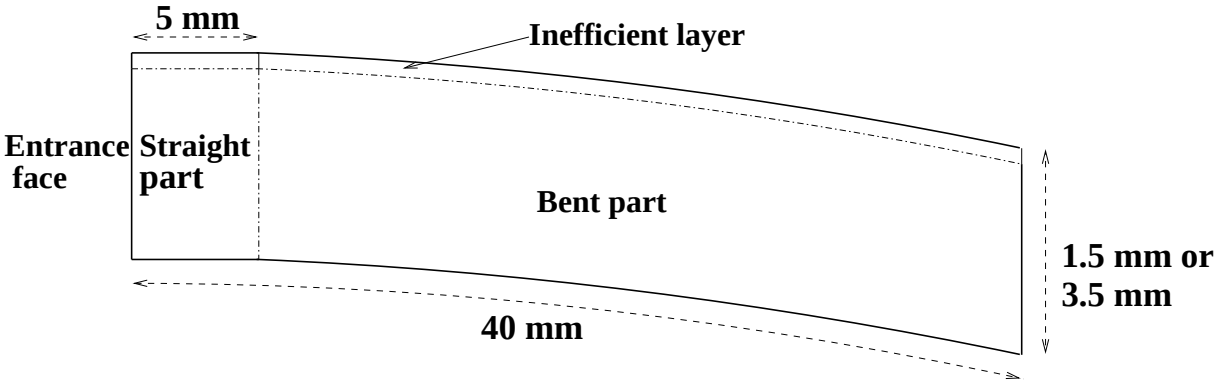

Figure 6.2: Crystal model used in the simulation.

6.3.2 Multiple Coulomb scattering in the crystal material

The particles that hit the crystal but are not channeled, as well as the dechanneled particles, experience multiple Coulomb scattering in the crystal material. The interaction of these particles with the crystal is modelled as interaction with amorphous material.

The distance that the particles traverse in the crystal material is estimated with the effective length L_{eff}. The effective length is calculated using the impact parameter and

Table 6.2: Crystal parameters used in the simulation.

Parameter	Value
Crystal full length	40 mm
Straight part length	5 mm
Crystal thickness	1.5 or 3.5 mm
Bending angle	8.5 mrad
Ineff. layer thickness	0–50 μm
Material	Si

angle of the impinging particle, and the crystal model shown in Fig. 6.2. The formula that is used for the calculation of the effective length is derived in Ref. [68].

The coordinates of a proton are changed as a result of multiple scattering according to the following transformation:

$$(x, x') \rightarrow (x + \Delta x, x' + \theta_0 z), \tag{6.2}$$

where Δx is the displacement (Eq. (6.4)), θ_0 is the multiple scattering angle (Eq. (6.3)) and z is a Gaussian random variable with mean zero and variance one. The transformation due to multiple scattering is made in both horizontal and vertical planes, i.e. the scattering increases particle amplitudes in both planes.

For the calculation of the multiple scattering angle, a Gaussian approximation is used with a width given by [74]

$$\theta_0 = \frac{13.6\,\mathrm{MeV}}{\beta\, c\, p}\sqrt{\frac{L_{\mathrm{eff}}}{X_0}}\,\left[1 + 0.038\,\ln\left(\frac{L_{\mathrm{eff}}}{X_0}\right)\right], \tag{6.3}$$

where p is the momentum, βc the velocity of the incident particle, and X_0 is the radiation length of the crystal material ($X_0 \sim 9.36$ cm for silicon).

For a proton that traverses the whole length of the crystal ($L_{\mathrm{eff}} = 4$ cm), the scattering angle is 71.7 μrad.

The displacement due to multiple scattering is calculated with [74]

$$\Delta x = L_{\mathrm{eff}}(z_1\theta_0/\sqrt{12} + z_2\theta_0/2), \tag{6.4}$$

where z_1 and z_2 are Gaussian random variables with zero mean and unit variance.

6.3.3 Channeling probabilities

The particles that hit the crystal in the effective region (not in the inefficient surface layer) and with an impact parameter smaller than the critical channeling angle, may be channeled through the crystal and extracted. For these particles, the probability of channeling is determined from the equations in Chapter 3.

The surface acceptance is given by Eq. (3.11). The particle may be lost at the crystal surface if the position of the hit x from the middle of two crystal planes is larger than the critical coordinate x_{crit}, i.e. the position of hit is too close to a crystal plane. In addition to this, the surface acceptance depends on the impact angle.

The particles that are channeled at the crystal surface may be lost from the channeling mode through dechanneling. The probabilities of channeling in the crystal are shown in Table 6.3 for three different beam energies. For example, the probability of staying in channeling mode at 120 GeV in the 5-mm-long straight part of the crystal is $P_{\mathrm{sd}} = 0.93$. Similarly, the probabilities for not being dechanneled in the curved part of the crystal or owing to the dechanneling fraction are P_{cd} and P_{df}, respectively. Consequently, the probability of channeling through the whole crystal, i.e. the deflection efficiency, neglecting losses at the surface, is $P = P_{\mathrm{sd}} \times P_{\mathrm{cd}} \times P_{\mathrm{df}} \simeq 39\%$ at 120 GeV.

Table 6.3: Parameters used in the simulation model to describe the probabilities that a particle stays in the channeling mode (for details see text).

Beam energy [GeV]	Dechanneling in straight part P_{sd}	Dechanneling in curved part P_{cd}	Dechanneling fraction P_{df}
14	0.58	0.03	0.98
120	0.93	0.51	0.82
270	0.96	0.56	0.61

6.3.4 Particle loss mechanisms

The particle may be considered lost from the simulation if one of the following conditions becomes true:

- horizontal amplitude is larger than the crystal external edge position;
- inelastic nuclear interaction in the crystal material;
- accumulated energy loss in the crystal exceeds a maximum value;

- number of turns in the accelerator exceeds a maximum value;

- betatron oscillation amplitude in the horizontal or vertical plane is larger than a maximum value.

The first condition means that the x-coordinate of the particle is larger than the distance of the external edge (crystal position + thickness) from the closed orbit. In this case the particle hits the bending device and cannot continue to circulate in the accelerator.

The particle may be lost through a nuclear interaction in the crystal material. The length λ_{I}, over which the beam intensity has been reduced to a fraction 1/e of the initial intensity, is about 45.5 cm in silicon [74].

The energy losses for each pass through the crystal accumulate since the RF was not switched on during the experiments. The particle is considered lost when the accumulated energy loss is more than 0.1% of the nominal beam energy.

The loss due to the number of turns in the accelerator is not a real loss mechanism but is implemented to avoid a particle being scattered to a trajectory in which it circulates forever without hitting the crystal.

An aperture limitation in the accelerator is caused by the limitation in the largest allowed horizontal or vertical betatron oscillation amplitude. The particle is lost if its amplitude becomes larger than 4 cm anywhere in the accelerator.

6.3.5 Extracted beam profiles

The simulation program can reproduce the extracted beam profiles for comparison with the profiles measured during experiments.

In the experiment, the extracted beam leaves the vacuum chamber through a 0.2-mm-thick stainless steel window, and traverses a series of detectors before it arrives at the hodoscope where the extracted beam profiles are measured (see Fig. 5.2). Multiple Coulomb scattering in the extracted beam line increases the size and divergence of the extracted beam.

In the simulation the extracted particles exiting from the crystal are tracked through the objects in the extracted beam line using Eqs. (6.3) and (6.4). A list of the objects in the extracted beam and their radiation lengths can be found in Ref. [75].

The amount of material that the extracted beam has to go through before it reaches the hodoscope is not negligible. A beam with zero size and no divergence obtains a RMS size of about 0.5 mm and a divergence of about 52 μrad owing to multiple scattering.

Simulated extracted beam profiles are shown in Section 7.4.3.

6.3.6 Multi-pass behaviour

In the beam extraction experiments it is not possible to tell how many times each extracted particle hits the crystal before extraction. In the simulations, one can follow each particle through each hit in the crystal and record the impact parameters and angles. For this reason, the simulations are a valuable tool for studying the multi-pass behaviour of the particles.

The impact parameter and angle distributions for the first hit in the crystal are shown in Fig. 6.1. The impact parameters are small: for typical kick strengths used in the experiments the average impact parameter is about 1 μm. The width of the initial impact angle distribution is small as well. The simulated RMS width is about 3 μrad, smaller than the critical channeling angle (14 μrad at 120 GeV).

The impact parameter and angle distributions for the first, second, third and fourth hits in the crystal are shown in Fig. 6.3. For the second and later impacts on the crystal, the situation is different from the first impact since the initial impact coordinates are determined by the beam diffusion process, whereas for the later impact coordinates the dominant process is scattering in the crystal material. For beam diffusion with white noise, the RMS kick strengths are below 10 nrad. For a proton that traverses the whole crystal, the RMS multiple Coulomb scattering angle is 71.7 μrad.

For the second hit in the crystal, the average impact parameter is already 0.21 mm, much larger than for the first hit, and there are particles across the whole thickness (1.5 mm) of the crystal. For later hits the average impact parameter further increases, and the shape of the distribution changes from exponential towards a flat distribution.

The width of the impact angle distribution also increases for later hits in the crystal. For example, for the fourth hit in the crystal, the RMS width is 35.1 μrad, larger than the critical channeling angle. In this way, multi-pass extraction can increase the width of the impact angle distribution and therefore increase the widths of measured angular scans. The widening of the impact angle distribution width beyond the critical channeling angle also means that the extraction efficiency in the pure multi-pass case may be lower than it would be if single-pass extraction were possible.

In the impact angle distribution, especially for the second or third hit in the crystal, there are several peaks. The origin of these peaks can be clearly seen if one inspects the (x,x') phase space of the particles incident on the crystal. The phase space configurations for the first, second and third hits are shown in Fig. 6.4. In the phase space for the second hit the particles are distributed along separate lines. The projection of this phase space configuration on the impact angle coordinate gives an angular distribution with a peak structure.

The reason for the line structure in the phase is shown in Fig. 6.5. The figure is in two parts, both showing in the (x,x') phase space the contour of the circulating SPS beam and the position of the 1.5-mm-thick crystal at 6.2 mm from the beam centre. The ellipse of the SPS beam is tilted because the value of the α-function at the crystal location is not zero. The first part of the figure shows how protons that hit the crystal

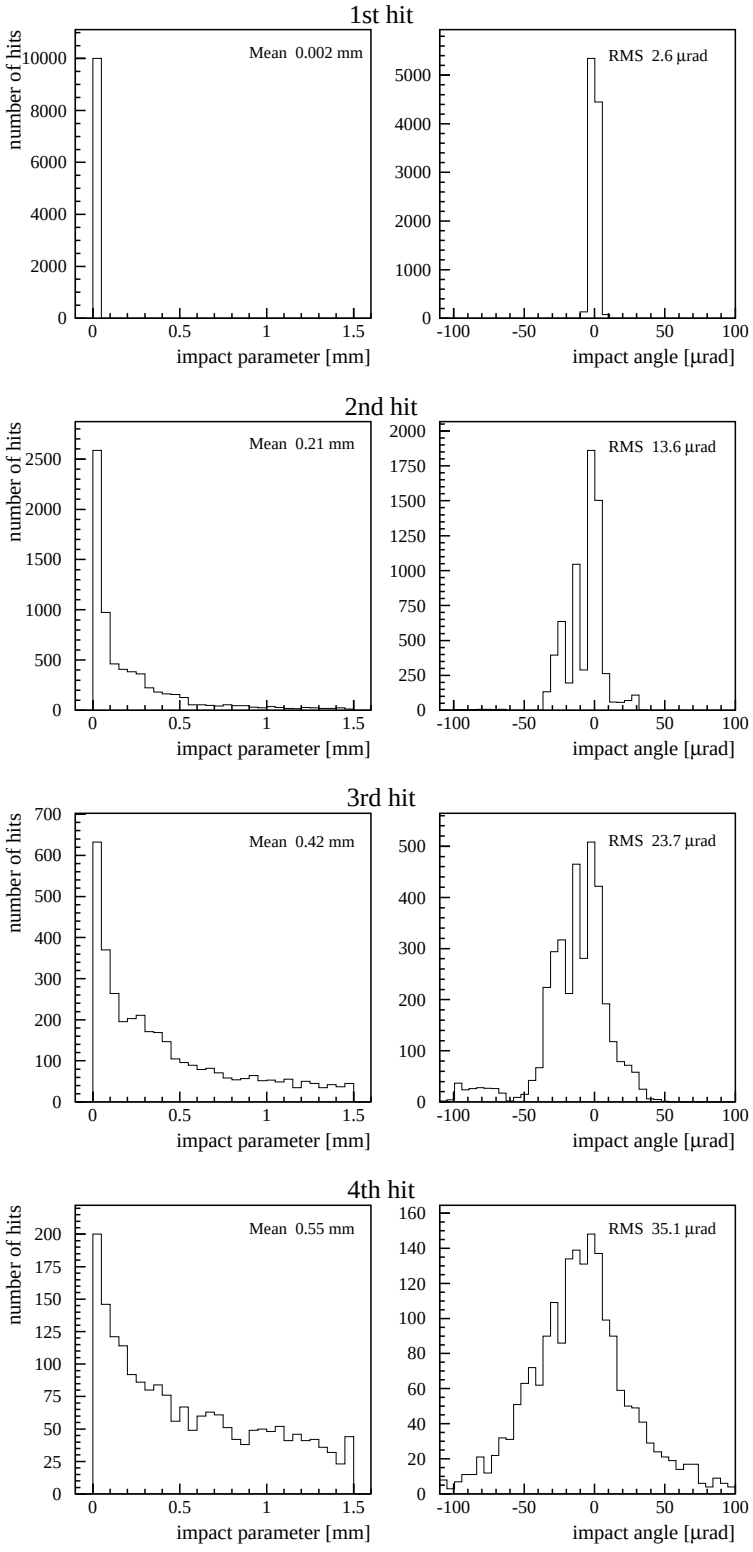

Figure 6.3: Impact parameter and angle distributions for the first, second, third and fourth hits in the crystal.

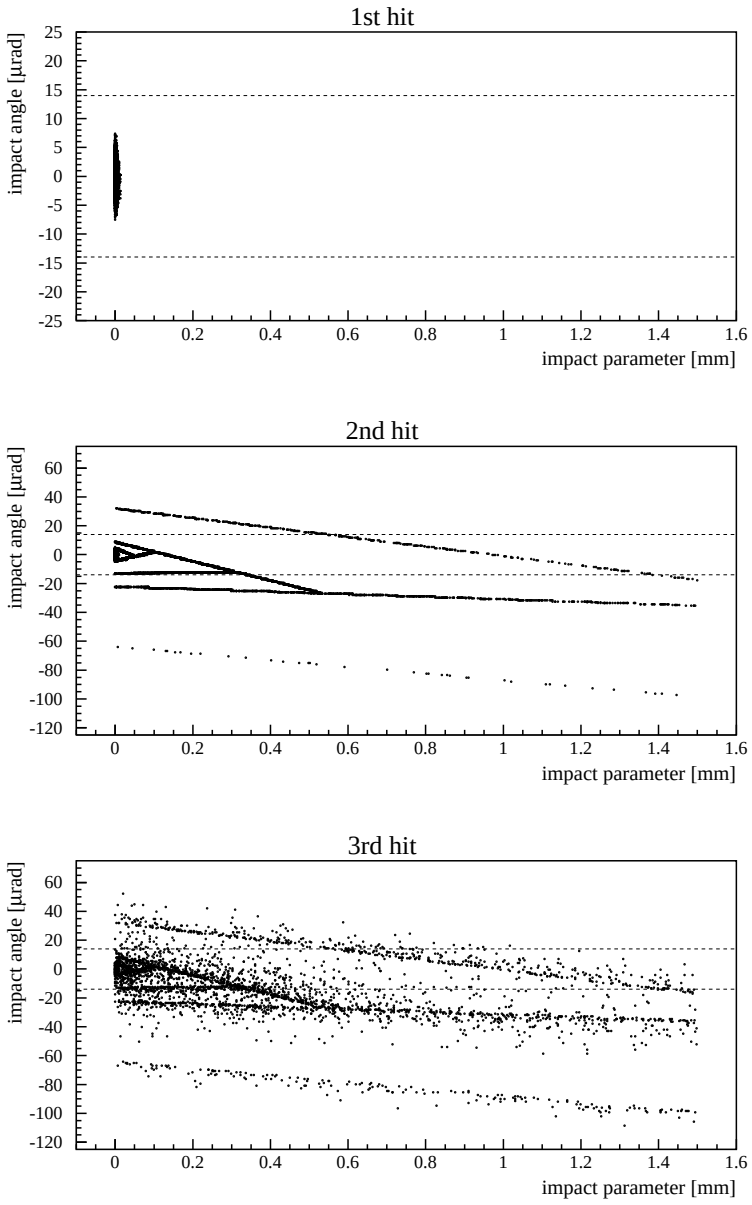

Figure 6.4: Phase space configurations for particles hitting the crystal (at the crystal entrance face). The first figure shows the initial phase space that results from the diffusion process (corresponds to Fig. 6.1). The second and third figures show the particles when they hit the crystal for the second and third times. The width of critical angle of channeling is indicated with the dashed lines. Notice the different angular scale in the first figure.

are scattered, causing an angular spread (a vertical 'line' in the phase space). These lines in the phase space are caused by multiple Coulomb scattering, and therefore the

particle density along such a line has a Gaussian distribution. Since the accelerator is linear, these lines remain straight when they are transported around the accelerator

The second part of Fig. 6.5 shows how, after a certain number of turns in the accelerator, the scattered protons arrive again at the crystal for the second hit. Betatron motion in the accelerator has transformed the angular spread into a tilted line in the phase space. The angle of the line for the second hit depends on the tune. It is a combination of these 'lines' caused by scattering in the crystal that gives rise to the line structure in the phase space and the peak structure in the impact angle distribution for the second hit in the crystal. The different lines correspond to different numbers of turns in the accelerator needed to reach the crystal again. For the third hit, the peak structure is less clearly visible because particles are scattered during the second hit from a larger phase space area than during the first hit when the phase space region occupied by the protons is almost point-like.

In the simulation that produced the impact parameters and angles in Figs. 6.3 and 6.4, the tune spread was set to zero. In the presence of tune spread, the peak structure for the second hit in Fig. 6.3 would be less clearly visible.

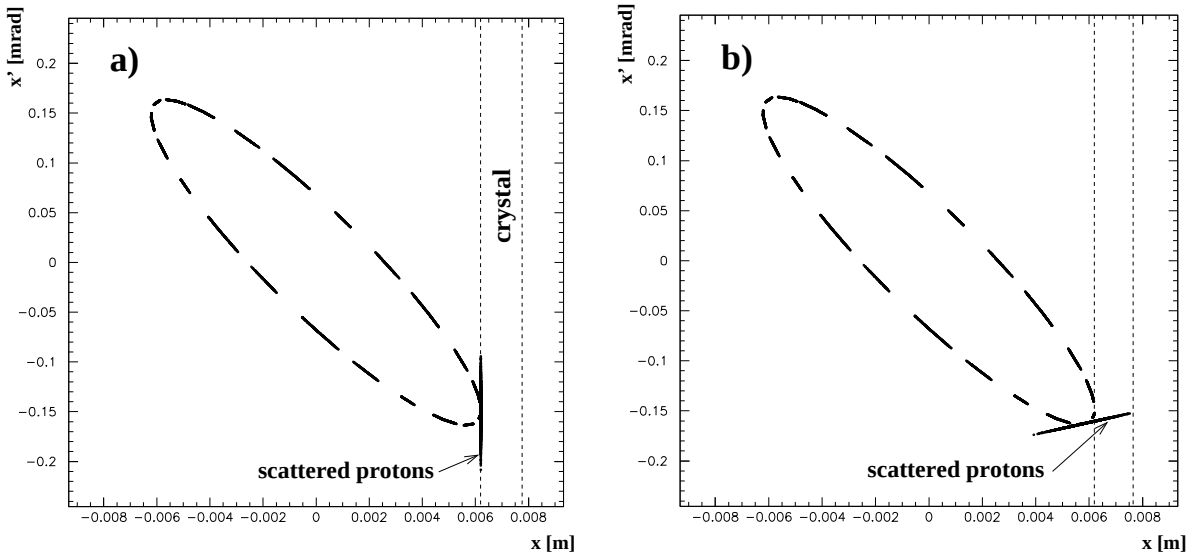

Figure 6.5: Illustration of how scattered protons arrive at the crystal for later passes. Part a) shows how scattering in the crystal causes angular spread of protons. In part b) the scattered protons arrive at the crystal again. The ellipse shows the contour of the SPS beam in (x,x') phase space and the vertical lines indicate the position of the crystal (for more details see text).

The size and shape of the phase space area occupied by the particles arriving at the crystal for the second or later hit depends, in addition to the scattering in the crystal, on the way the accelerator transports the scattered particles again to the crystal. As already shown in Ref. [67], the tune and the β-function at the crystal location affect

the extraction efficiency.

The simulated extraction efficiency is plotted against the value of β-function in Fig. 6.6. It can be seen that the efficiency has a maximum for a certain value of the β-function. The value of β that gives the largest efficiency depends on the exact parameters of the extraction set-up such as the tune and the inefficient layer thickness, but Fig. 6.6 indicates that in the case of the SPS a lower value of the β-function would give a higher extraction efficiency.

The dependence of multi-pass extraction efficiency on the β-function can be understood by considering the phase space area in which extraction is possible. To be extracted, the particles have to hit the crystal within the critical channeling angle and within the thickness of the crystal (see Fig. 6.4). With small values of β, the angular distribution of particles at the crystal entrance face gets larger, which increases losses due to the critical angle. Similarly, with large values of β, the particle distribution gets wider in the horizontal direction and the losses due to the limited thickness of the crystal are increased [67]. In addition to this, the losses with large values of β in multi-pass extraction mode are increased because of large deflections experienced by the particles (see Eq. (2.26)). The large deflections increase the angular divergence of the particles at the crystal for the second and later hits, which decreases the extraction efficiency.

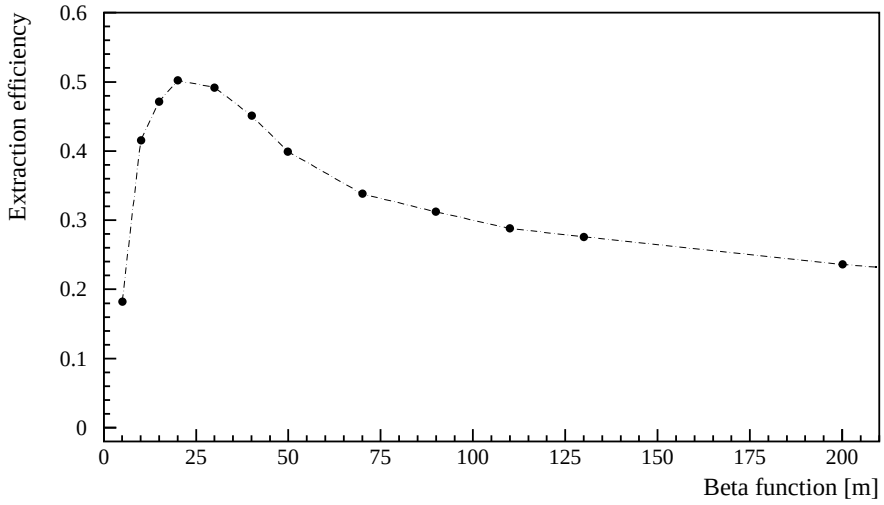

Figure 6.6: Simulated extraction efficiency plotted against the value of the β-function.

With single-pass extraction, it is possible to obtain a high extraction efficiency, depending on the deflection efficiency of the crystal, but the situation is very dependent on the initial impact parameters and angles at the crystal. The single-pass extraction efficiency also depends on the exact operating conditions of the accelerator. In the

case of multi-pass extraction, it is possible to optimize, for example, the extraction efficiency, extracted beam sizes and divergences as a function of parameters such as the tune, β-function, crystal material and crystal length. These parameters determine how the particles arrive at the crystal for the second and later hits and, together with deflection efficiency, define the efficiency of the whole extraction process. By the optimization of multi-pass extraction, it is possible to build a more robust extraction set-up than could be achieved by relying on single-pass extraction alone.

Chapter 7

Experimental results and comparison with simulations

In this chapter, the results of the crystal extraction experiment at the SPS are presented. The presentation follows the evolution of the experiment; the results obtained with different types of crystals are shown in chronological order. This approach makes it possible to show increased understanding obtained at each phase, and it shows how unexpected results motivated new measurements and developments.

The crystal extraction experiments were started in 1992 using crystals bent in 'bridge'-type bending devices. The results of these initial experiments are shown in Section 7.1.

After the initial results, one of the main questions was whether the protons were extracted at the first or at a later hit on the crystal. This question was studied by using a crystal that does not allow extraction at first pass. The results obtained with this 'amorphous-layer' crystal are shown in Section 7.2.

The main results presented in this thesis were obtained by using U-shaped crystals that have an improved geometry compared to the first crystals. Many measurements of angular scans, extracted beam profiles and extraction efficiencies have been performed and the results are shown in Section 7.3.

In most of the computer simulations extraction with U-shaped crystals has been simulated. Simulation results and a comparison with experimental results are presented in Section 7.4.

After that, results with different beam energies (Section 7.5) and results with another beam excitation method (Section 7.6) are shown.

All of the experimental results were obtained with an SPS beam energy of 120 GeV and with transverse noise excitation, unless otherwise mentioned.

The results reported here were obtained when the SPS accelerator was in a good state. In the case of problems with the SPS, e.g. when the SPS beam is not stable, there can be big fluctuations in the extracted beam intensity observed with the scintillators and especially with the scintillating screen. Under such conditions, worse results (lower extraction efficiencies, wider angular scans) can be obtained. Similar results can be obtained when the SPS is being set up for the measurements, i.e. when the SPS beam is blown up and before steady beam conditions are reached.

7.1 Initial measurements

7.1.1 Measurements in kick mode

An extracted beam was first observed in the kick mode (see Section 5.3.1). A clear signal of an extracted beam was seen by comparing two scintillators: one positioned inside the SPS ring to measure the extracted particles and the other outside of the SPS to monitor background. The inside scintillator measured a time structure synchronized with the kick and with the betatron motion of the beam. The results obtained in kick mode are shown in Refs. [76] and [77].

Experiments with the kick mode demonstrated that crystal assisted extraction works and that the crystal can be aligned with the circulating beam. However, owing to the disadvantages mentioned in Section 5.3.1, kick mode was used only in the early phase of the experiment; since then the measurements have been carried out in diffusion mode.

7.1.2 Results with first crystals

The first measurements with noise-induced beam diffusion were carried out with crystals bent in bridge-type benders (crystals ST1 and ST2 in Table 5.2).

A typical angular scan with the first crystals in shown in Fig. 7.1. The estimated error in the counting rate is indicated by the point in the top right-hand corner of the figure.

The full width at half maximum (FWHM) of the angular scans is typically about 200 μrad. The width of the scans is much larger than was expected by considering the narrow impact angle distributions (a few μrads) and two times the critical angle of channeling (about $2 \times 14\,\mu\text{rad} = 28\,\mu\text{rad}$ at 120 GeV).

Horizontal and vertical extracted beam profiles measured with the hodoscope are shown in Fig. 7.2. In the first case, the profiles were measured with a crystal that was about 100 μrad away from the optimal alignment. In this case two peaks can be seen in the profiles, and the scintillating screen showed two separate extracted beams. In the second case the profiles were measured with a crystal at the optimal alignment, i.e. at the peak of the angular scan. With an optimally aligned crystal there is only one peak in the profiles.

The large width of the angular scans and the double peaks in the extracted beam profiles can be understood by considering the anticlastic bending of the first crystals (see Section 5.4.2). Owing to the anticlastic bending, the orientation of the crystal planes varies depending on vertical position, which allows extraction in a larger range of angles for a beam with a large vertical size. The vertical size of the SPS beam hitting the crystal can get larger because the protons may hit the crystal several times before they are extracted (multi-pass extraction).

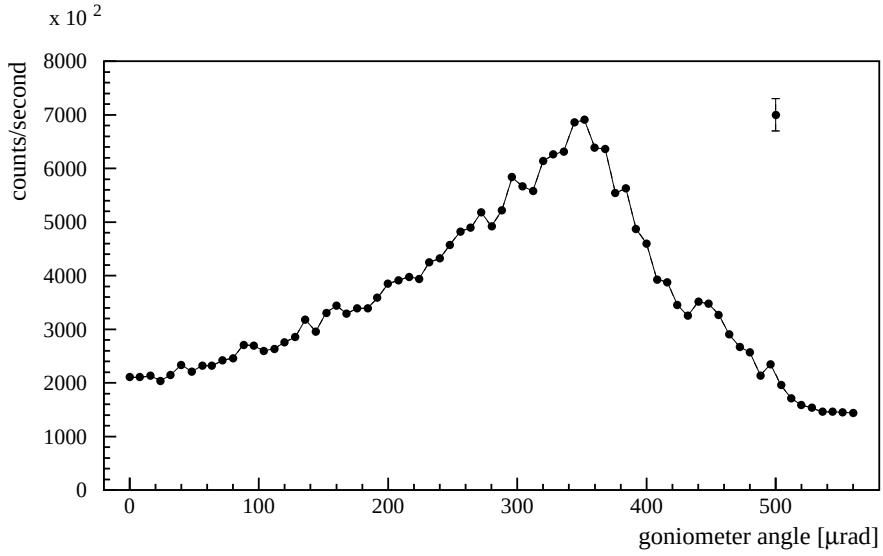

Figure 7.1: A typical angular scan measured with the first crystals.

The double peaks in the extracted beam profiles can also be explained by the anticlastic bending. For a crystal that is not at optimal alignment, the alignment between the incoming beam and the crystal planes can be exact at two separate vertical positions on the crystal entrance face. This reason for the double peaks has been shown in earlier simulations [78].

The anticlastic bending of the first crystals was directly measured in the SPS using the circulating proton beam. In this experiment, the total vertical height of the SPS beam was kept small (about 1 mm) by collimation. The beam was moved to different vertical positions in the crystal entrance face by local orbit bumps. An angular scan was made at each vertical position and the angular position where the crystal was optimally aligned with the SPS beam was recorded. The result is shown in Fig. 7.3, which indicates that the alignment of the crystal planes as a function of vertical coordinate can be parametrized by a parabola. A similar result was obtained with laser scans on the crystal surface (Fig. 5.7).

Extraction efficiencies measured with the first crystals are shown in Table 7.1. The low value for detection efficiency is due to the fact that the anti-coincidence with scintillator S3 was included in the trigger (see Section 5.5.4). The errors shown in Table 7.1 are systematic uncertainties of the different measurements.

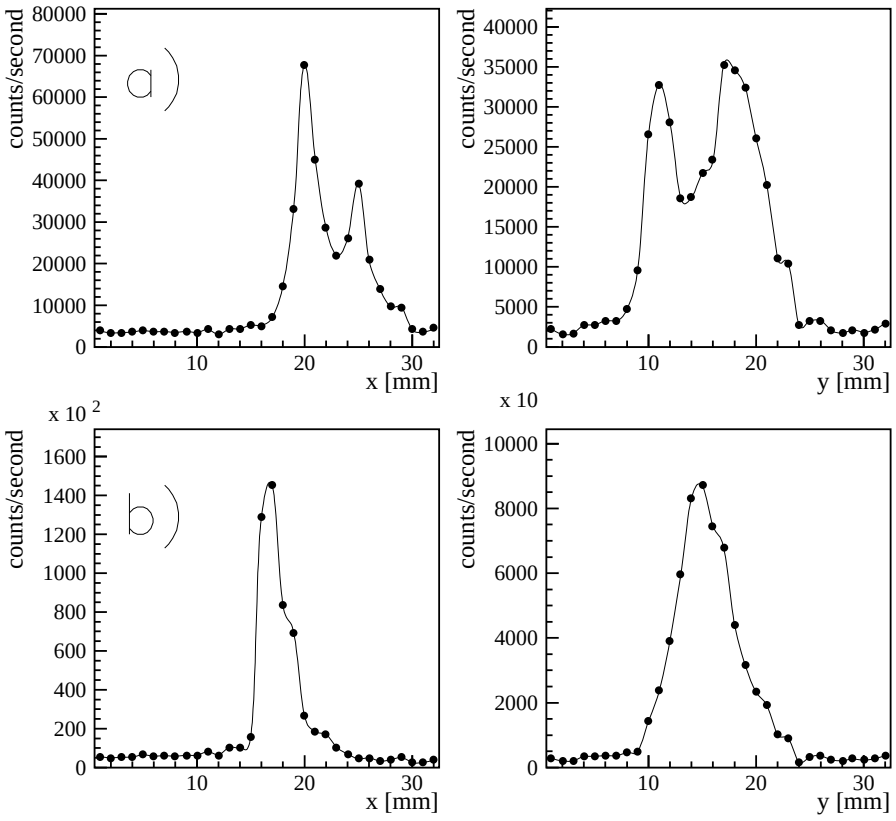

Figure 7.2: Horizontal and vertical hodoscope profiles measured using a crystal in a bridge-type bender: (a) when the crystal was not at optimal alignment; and (b) with a well-aligned crystal.

7.2 Study of multi-pass extraction

One of the main questions in the crystal extraction experiment has been whether the protons arriving at the crystal are extracted when they hit the crystal for the first time (single-pass extraction, see Section 4.2) or at a later pass (multi-pass extraction).

Some experimental results such as the large widths of the angular scans are best understood by assuming that the protons are extracted through multi-pass extraction. On the other hand, a clear observation of single-pass extraction and its separation from multi-pass extraction is difficult. Pure single-pass extraction should manifest itself as a narrow peak, twice the critical angle folded with the angular width of the incoming beam, in the angular scans. However, no such observation has been made.

As observing and proving a clear signal for single-pass extraction is difficult, a different approach was chosen by preparing a crystal that would only allow multi-pass

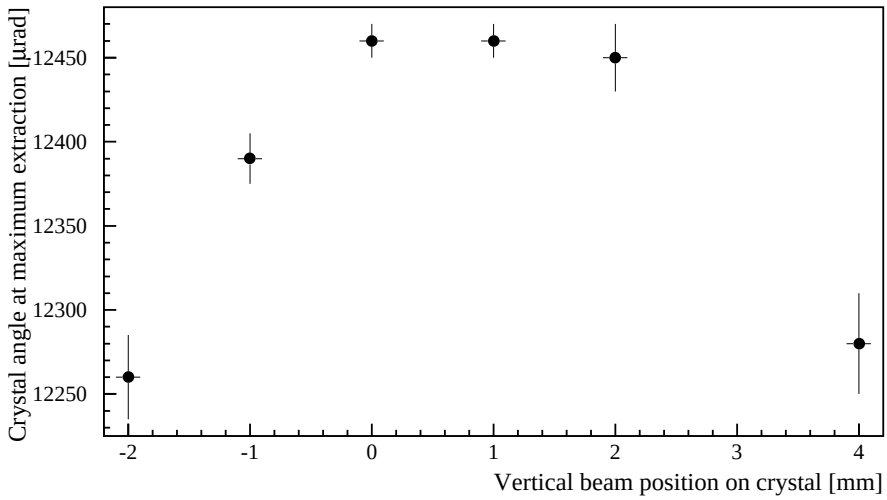

Figure 7.3: Orientation of crystal planes as a function of vertical position on the crystal entrance face (anticlastic bending). For details see text.

Table 7.1: Extraction efficiencies measured with the first crystals [79].

	Crystal 1	Crystal 2
SPS intensity [10^{11} p]	7.0 ± 0.1	3.7 ± 0.1
Beam lifetime [hours]	20 ± 2	12 ± 1
Extracted rate [10^5 p/s]	5.6	6.6
Background [%]	5	2
Detection efficiency [%]	78 ± 12	78 ± 12
Extraction efficiency [%]	10.2 ± 1.7	9.3 ± 1.6

extraction. For this purpose, one of the first crystals was covered with an amorphous layer of silicon oxide [80]. The thickness of this amorphous layer was 30 μm. This crystal (ST3 in Table 5.2) is called 'the amorphous-layer crystal'.

The thickness of the amorphous layer was chosen by considering the expected impact parameters at first and later hits in the crystal. The initial impact parameters obtained from simulations are very small. Simulations with a large kick strength compared with the ones used in the experiments (Fig. 6.1) give an average impact parameter of about 2 μm. For typical kick strengths used in the experiments the initial impact parameters

are of the order of 50 nm – 1 μm. On the other hand, the simulations show that during the second or third hit in the crystal the average impact parameters are already much larger than the thickness of the amorphous layer. This means that the layer prevents practically completely single-pass extraction, but allows extraction at later passes.

7.2.1 Results with the amorphous-layer crystal

When the amorphous-layer crystal was first used in the experiments, an extracted beam was immediately seen, providing clear evidence for multi-pass extraction. The extracted beam profiles measured with the hodoscope are shown in Fig. 7.4.

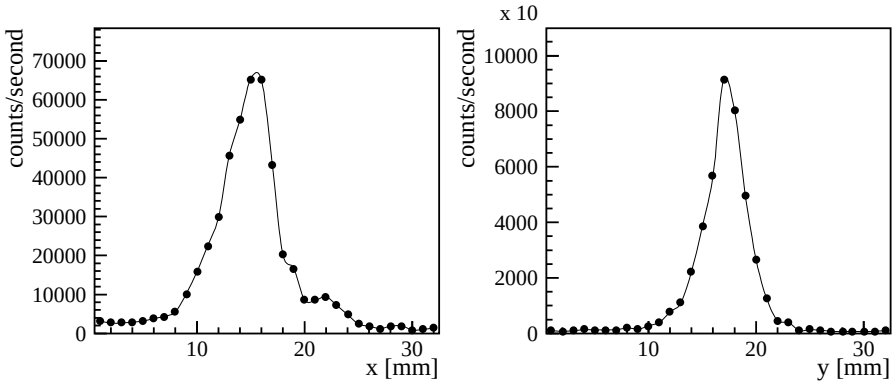

Figure 7.4: Extracted beam profiles with the amorphous-layer crystal.

An angular scan with the amorphous-layer crystal is shown in Fig. 7.5. The width of the scan is about 300 μrad. The amorphous-layer crystal is bent in a bridge-type bending device, which means that it suffers from anticlastic bending like the other crystals bent in that way. The large width of the scan is mainly due to anticlastic bending, and the contribution of the amorphous layer to the width of the scan has been shown to be small by simulations.

Extraction efficiencies measured with the amorphous layer crystal are shown in Table 7.2. The highest efficiencies are about 7%, comparable to the results obtained with the same crystal before the amorphous layer was added. However, the background in the extracted beam is higher than before. The background is calculated from the hodoscope profiles by comparing the counting rates in the hodoscope channels which detect the extracted beam with those which measure the background. The higher background can be explained by the fact that with the amorphous layer the protons need more passes in the crystal before they can be extracted, and therefore there is a larger probability of nuclear reactions in the crystal or in the bending device.

The fact that a beam could be extracted with the amorphous-layer crystal is

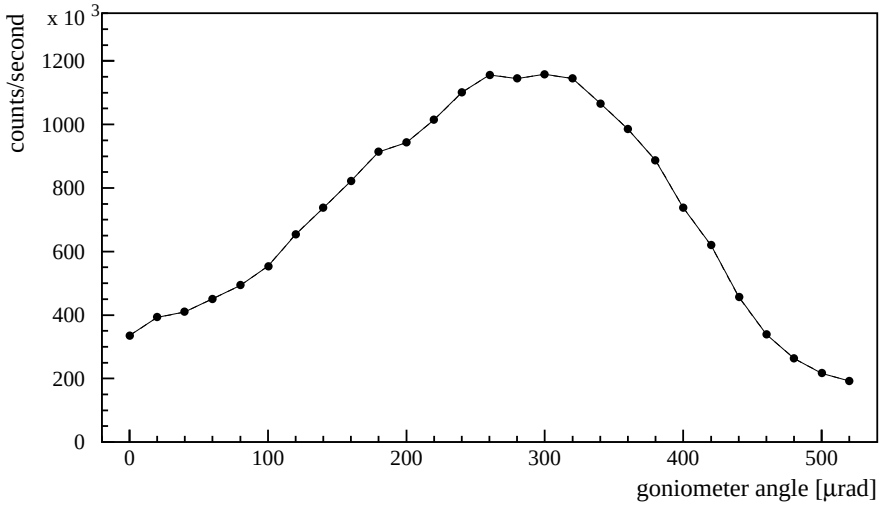

Figure 7.5: Angular scan with the amorphous-layer crystal.

Table 7.2: Extraction efficiencies measured with the amorphous-layer crystal.

SPS intensity [10^{11} p]	Lifetime [hours]	Extraction rate [10^5 counts/s]	Background [%]	Extr. efficiency [%]
5.9	33 ± 2	2.07 ± 0.02	13.9	3.6 ± 0.4
5.8	43 ± 10	1.54 ± 0.05	15.2	3.7 ± 0.8
4.4	28 ± 2	2.38 ± 0.03	13.0	4.8 ± 0.5
1.9	5.1 ± 0.2	8.78 ± 0.04	13.8	7.6 ± 0.8
0.6	1.8 ± 2	7.27 ± 0.05	13.3	7.4 ± 0.8

clear evidence of multi-pass extraction. Furthermore, all results obtained with the amorphous-layer crystal (profiles, scans, efficiencies) are comparable to the results without the layer, which indicates that multi-pass extraction is an important process and that it strongly contributes to extraction even for crystals that do not have an intentional inefficient layer.

The demonstration of the importance of multi-pass extraction has significant consequences for the design of future extraction schemes. This point will be discussed in Section 8.2.

7.3 Results with U-shaped crystals

The U-shaped crystals were prepared to eliminate the anticlastic bending of the first crystals (see Section 5.4.3). Most of the results shown here were obtained with a 1.5-mm-thick U-shaped crystal (GR2 in Table 5.2). Results with the other U-shaped crystals (GR3, GR4 and GR5) are shown in later sections.

7.3.1 Angular scans and extracted beam profiles

An angular scan with the U-shaped crystals is shown in Fig. 7.6. The widths of the scans with U-shaped crystals are typically 70–150 μrad, smaller than those measured with the first crystals. This indicates that the almost complete elimination of the anticlastic bending has reduced the angular acceptance of the U-shaped crystals in crystal assisted extraction.

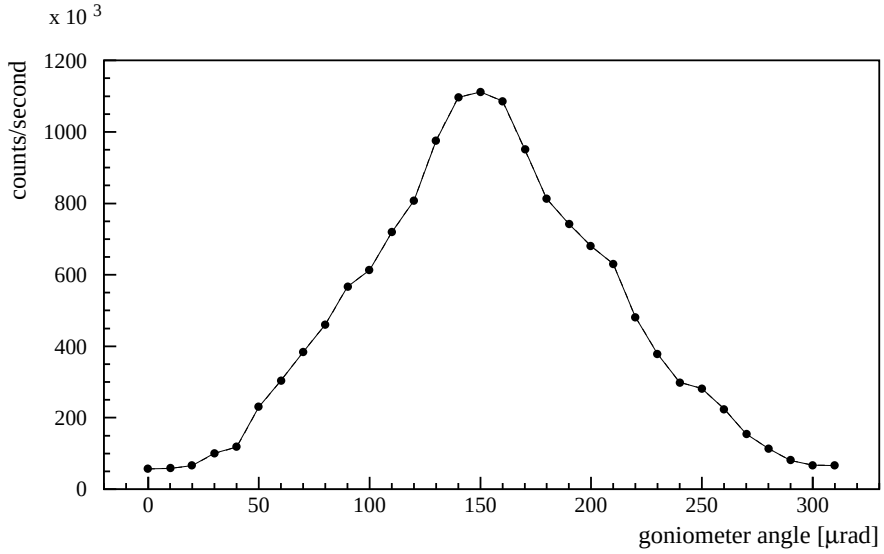

Figure 7.6: Angular scan with the U-shaped crystals.

Extracted beam profiles measured with the hodoscope are shown in Fig. 7.7. In this case there are no double peaks for a crystal that is away from the optimal alignment because of the elimination of anticlastic bending. The horizontal profiles are narrower compared with the first crystals and close to the resolution of the hodoscope. A very interesting property of the vertical profile is that its width changes as a function of the crystal angle, i.e. it is narrower when the crystal is well aligned.

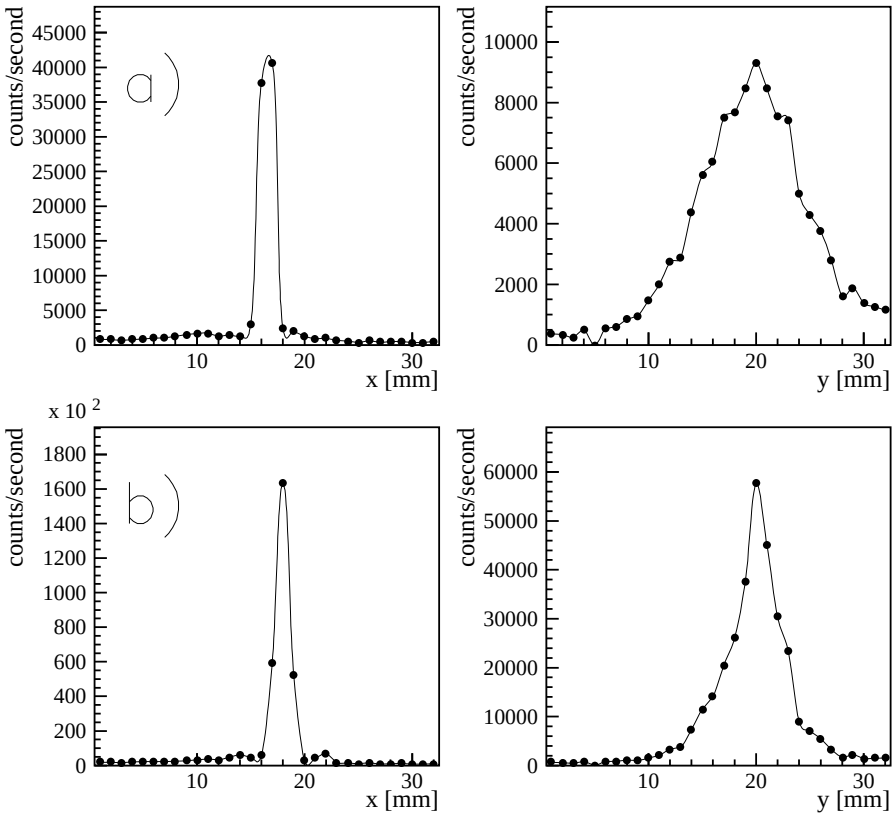

Figure 7.7: Horizontal and vertical hodoscope profiles measured using a U-shaped crystal: (a) when the crystal was not at optimal alignment; and (b) with a well-aligned crystal.

7.3.2 Vertical profile sizes

Extracted beam profiles obtained with a U-shaped crystal (GR2) are shown in Fig. 7.7. The width of the vertical profile clearly changes between the cases where the crystal is well aligned and where it is out of optimal alignment. The width of the vertical profile during an angular scan, i.e. as a function of crystal alignment, is shown in Fig. 7.8. It can be seen that the vertical profile is narrowest when the crystal is well aligned with the SPS beam. The vertical profile widths shown are obtained by calculating the RMS width of the profiles using all the 32 hodoscope strips and therefore cannot be directly compared with the widths where background has been subtracted.

The change in the vertical profile width can be understood by considering the number of passes in the crystal that are necessary for the protons to be channeled and extracted. At each pass through the crystal that does not lead to extraction, the

angular distribution of the protons gets wider in both horizontal and vertical planes because of multiple scattering in the crystal material. With a well-aligned crystal, fewer passes are needed and the width of the vertical profile suffers less from multiple scattering. More details are given with the simulation results in Section 7.4.3.

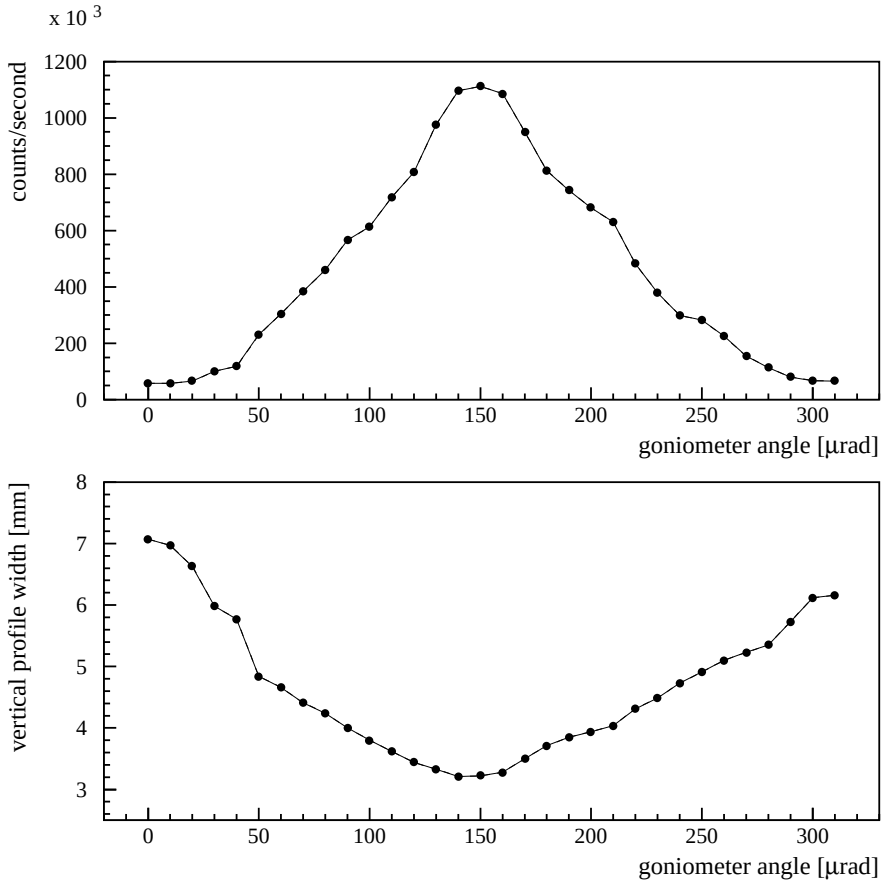

Figure 7.8: Vertical profile width during an angular scan.

7.3.3 Extraction efficiency measurements

Extraction efficiency measurements with a U-shaped crystal (GR2) are shown in Table 7.3. The extraction efficiency is defined in Eq. (4.1) as the ratio of the number of extracted particles to the number of particles lost from the SPS per second.

The extraction rate can be measured with the threefold scintillator coincidence S1×S2×S3 or with the hodoscope. The number of protons lost from the SPS is obtained from the lifetime measurement (see Section 5.7). The errors on the extraction efficiencies are dominated by the uncertainties in the measurement of SPS beam intensity and lifetime.

Table 7.3: Extraction efficiencies measured with the U-shaped crystals.

SPS intensity [10^{11} p]	Lifetime [hours]	Extraction rate [10^5 counts/s]	Background [%]	Extr. efficiency [%]
4.9	44 ± 8	3.45 ± 0.06	3.2	10.6 ± 2.6
0.13	0.7 ± 0.1	7.88 ± 0.07	4.0	15.4 ± 2.2
0.07	0.9 ± 0.1	2.67 ± 0.04	3.2	12.4 ± 1.4
0.16	0.6 ± 0.1	9.48 ± 0.06	3.1	13.0 ± 2.2

The background in the extracted beam is estimated from the hodoscope profiles. The profiles show a narrow peak on a fairly flat background which makes it possible to deduce the fraction of the background in the measured beam.

The detector efficiencies ϵ_d are high, $\epsilon_d > 99\%$ for the individual scintillators and $\epsilon_d \sim 98\%$ for the hodoscope [81]. Because of these high efficiencies and the difficulty in measuring the exact values, the detector efficiencies are not taken into account in the extraction efficiency calculation. Correction by the detector efficiencies would make the extraction efficiencies slightly higher, so the values shown in Table 7.3 can be seen as lower limits although they are very close to the correct values.

Repeated measurements of extraction efficiencies and angular scans have allowed the reproducibility of the results to be studied. Generally, when well-defined beam conditions have been achieved, the results are well reproducible. There are, however, some variations in the widths and shapes of the angular scans, and in the extraction efficiency values measured. No clear correlation of these variations with parameters related to the state of the accelerator or to the measurement procedure has been found.

7.3.4 Results with modified U-shaped crystals

Results with thicker crystals

Two 3.5-mm-thick U-shaped crystals have been used in the SPS experiments (GR3 and GR4 in Table 5.2). They were prepared because the simulations show that protons can have larger impact parameters than 1.5 mm (thickness of the other crystals) owing to multiple passes in the crystal, and as a result the efficiency should be slightly higher with thicker crystals. Another reason for the thicker crystals was the preparation for measurements with an additional scatterer that would give higher impact parameters on the crystal. However, the use of a scatterer is not reported in this thesis.

A comparison of the extraction efficiencies measured with 1.5 mm (crystal GR2) and 3.5 mm (crystal GR4) thick crystals is given in Ref. [87]. The comparison was

made by first measuring the efficiency with one of the crystals, and then bringing the other crystal towards the beam until a small drop in the SPS beam intensity could be measured. This meant that the second crystal had come out of the 'shadow' created by the first crystal, and the two crystals were at the same relative position with respect to the SPS beam, thus making it possible to compare the two crystals in similar conditions. The result of the comparison shows that the two crystals give almost the same extraction efficiency. The relative increase in the efficiency with the thicker crystal predicted by the simulation is only 5%, i.e. the expected difference is smaller than the measurement error.

Table 7.4: Extraction efficiency comparison with the 3.5-mm-thick U-shaped crystals.

Crystal	SPS intensity [10^{11} p]	Lifetime [hours]	Extraction rate [10^5 counts/s]	Extr. efficiency [%]
GR2	0.96	6.7 ± 0.4	5.06 ± 0.04	12.8 ± 1.3
GR4	1.01	8.0 ± 0.5	4.44 ± 0.04	12.7 ± 1.4

The angular scans with the thicker crystals are also similar to the scans with the thinner U-shaped crystals. However, a clear difference between the thicker and thinner crystals can be seen by looking at the extracted beam profiles measured with thicker crystals. The horizontal profiles shown in Fig. 7.9 have a 'shoulder' to the right. The shape and size of the shoulder vary depending on experimental conditions. The shoulder corresponds to particles that have been deflected more than average, and therefore cannot be due to dechanneled particles. The shoulder was observed with both 3.5-mm-thick crystals, but no such observation has been made with the 1.5-mm-thick crystals.

The shoulder in the horizontal profile can be caused by the increased width of the crystal. In the horizontal plane, the extracted beam exits the crystal within the critical channeling angle (about $2 \times 14\,\mu\text{rad} = 28\,\mu\text{rad}$ at 120 GeV). The horizontal size of the extracted beam at the hodoscope location (about 22 m downstream of the crystal) can therefore be significantly increased because of the thicker crystal if there are particles over the whole crystal thickness. Owing to multiple passes in the crystal, the particles can have large impact parameters (cf. Fig. 6.3) up to several millimetres. The horizontal size of the extracted beam when it exits the crystal can therefore depend on the crystal thickness. In addition to this, the bending of a thicker crystal may cause unwanted twists at the crystal exit face, which can lead to increased divergence of the extracted beam in the horizontal plane. However, no such observation was made when the crystal bending was studied [50].

The fraction of the extracted beam in the shoulder is larger when the crystal is not at optimal alignment [87], i.e. when the contribution of multi-pass extraction is increased. This corroborates the idea that the shoulder is caused by the increased size

of the extracted beam (because of the crystal thickness) at the crystal exit face. Also when simulations are made in pure multi-pass mode (cf. Section 7.4), an extracted beam obtained with a 3.5-mm-thick crystal has more protons towards the right of the beam, i.e. a shoulder, than an extracted beam obtained with a 1.5-mm-thick crystal.

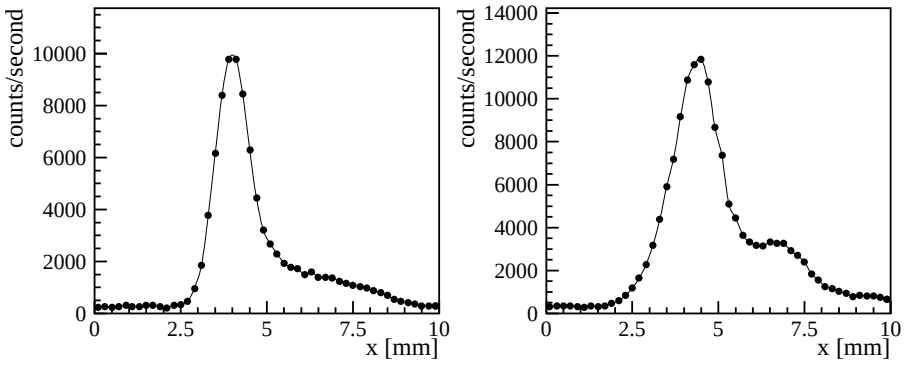

Figure 7.9: Two horizontal extracted beam profiles measured with the FISC when the beam was extracted using 3.5-mm-thick U-shaped crystals.

Crystal with a known miscut

The efficiency of crystal assisted extraction, especially for single-pass extraction, depends on the quality of the crystal surface. The inefficient layer on the surface should be as thin as possible. One of the reasons that can cause an inefficient range of impact parameters is a negative miscut angle (cf. Section 5.4.1). The miscut angles of the U-shaped crystals are small, less than 100 μrad (corresponding to a 4 μm inefficient layer), but their directions are not known. A negative miscut angle could explain the fact that no clear sign of single-pass extraction has been observed and that the extraction efficiency is lower than could be expected.

To study the effect of the miscut angle, a crystal (GR5 in Table 5.2) with a known positive miscut angle was prepared.

The extraction efficiency measurements made with the GR5 crystal are reported in Ref. [89]. The efficiency measurements, including a direct comparison with crystal GR2 in a method explained in Section 7.3.4, do not show any clear difference between crystals GR2 and GR5. Based on these results, it can be concluded that the crystal miscut has not played a significant role in the earlier measurements made with other U-shaped crystals. The fact that the experimental results do not strongly depend on the miscut angle is another indication of the importance of multi-pass extraction.

7.3.5 Crystal induced background

When 15% of the protons hitting the crystal are extracted, the rest of the protons are lost somewhere along the SPS ring. The simulations indicate that a large fraction of the losses occur at the crystal location. The background created by the lost particles has been monitored by two scintillators, one located far away from the crystals in the SPS ring (in LSS1), and the other located downstream of the crystals in LSS5, but on the opposite side of the SPS vacuum pipe from the extracted beam line. This scintillator, called S5, is about the same distance from the crystals as the scintillator S2 in Fig. 5.2, but is positioned on the other side of the beam pipe.

The scintillator far away from the crystal records only few counts during extraction, which means that few particles are lost at that location in the SPS. Therefore this scintillator is not very useful for background studies. However, the scintillator S5 close to the crystal counts many more background particles. The counting rate of the S5 during an angular scan is shown in Fig. 7.10. The upper part of the figure shows the extracted beam intensity as a function of crystal angle, and the lower part shows the counting rate of the S5 scintillator during the angular scan. This particular scan was recorded at 270 GeV (cf. Section 7.5). When the crystal is well aligned with the SPS beam and the extracted beam intensity is high, there is a 'dip' in the counting rate of the S5 as already shown in Ref. [59]. With a well-aligned crystal, some of the protons that arrive on the crystal are channeled and extracted so that less background is created.

The size of the background dip, i.e. the reduction in S5 counting rate, depends on the experimental conditions and varies for different angular scans.

There is, however, a reduction in the background created by a well-aligned crystal compared to a crystal that is not in perfect alignment, or compared to an amorphous piece of material positioned in the beam halo. This indicates that a crystal, by extracting a fraction of the particles incident on it, could be a more efficient collimation device than the ordinary collimators that use blocks of amorphous material. The crystal can also be easily aligned with respect to the particles incident on it by using the extracted beam intensity during an angular scan.

7.4 Simulation results

The main experimental results (extraction efficiency, angular scans, extracted beam profiles) measured using the U-shaped crystal GR2 are compared in this section with the simulation results obtained by using the simulation model described in Chapter 6. The crystal model used in the simulations is the 1.5-mm-thick U-shaped crystal.

At the end of this section, the general functioning of the simulation is presented to demonstrate how the simulation program obtains the results shown and in order to give more insight into the extraction process.

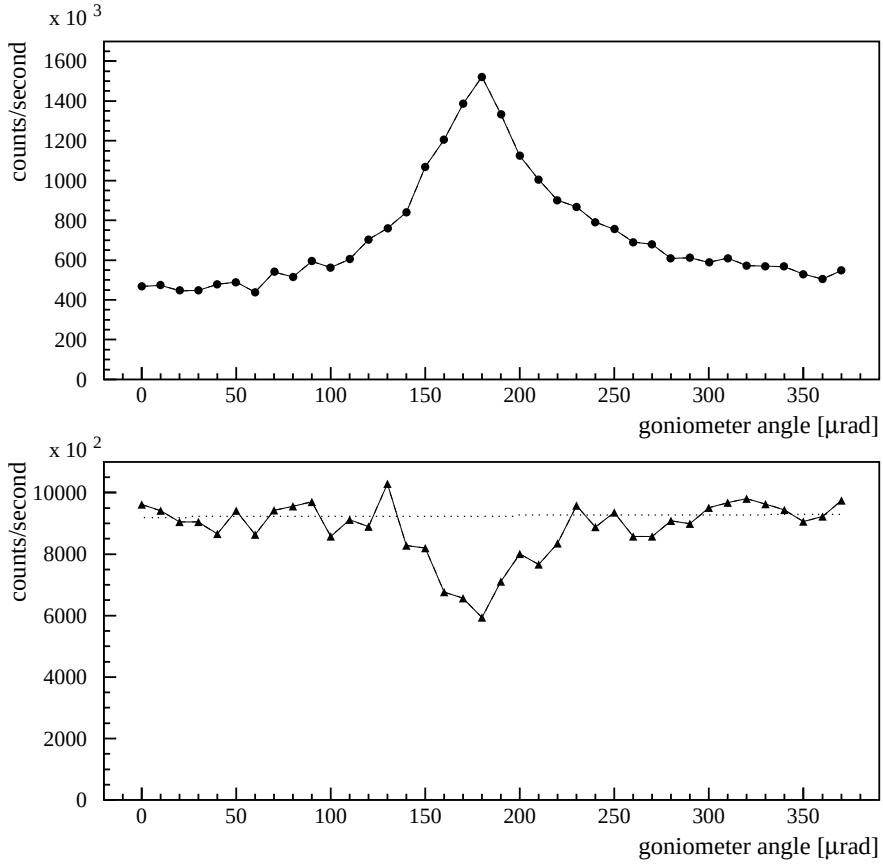

Figure 7.10: Reduction in the background created in the crystal when the crystal is well aligned with the SPS beam (see text). The extracted beam intensity is shown in the upper part and the background at the crystal location in the lower part.

7.4.1 Extraction efficiency

Extraction efficiency is a combined result of many different factors such as the beam diffusion process (initial impact parameters and angles), channeling probabilities, interactions in the crystal and the different particle loss mechanisms. Some of these factors, such as the thickness of the inefficient layer on the crystal surface, are not precisely known. Simulated extraction efficiency is plotted as a function of the inefficient-layer thickness in Fig. 7.11. The figure shows that efficiency is reduced by a large factor between layer thicknesses of 0 μm and 10 μm. This is due to the fact that the impact parameters are in this range so that single-pass extraction is possible. Above 10 μm, only multi-pass extraction is possible and the efficiency goes down slowly as a function of layer thickness. Fig. 7.11 also shows that the efficiencies obtained by the simulations using thin surface layers are higher than those measured in the experiments.

The agreement between simulations and measurements is better in the region where particles are extracted through multi-pass extraction.

Other simulation models also predict higher extraction efficiencies than are measured. In these simulations a satisfactory agreement between simulation and measurement results is found only when the surface layer is assumed to be thick enough for single-pass extraction not to be possible [19].

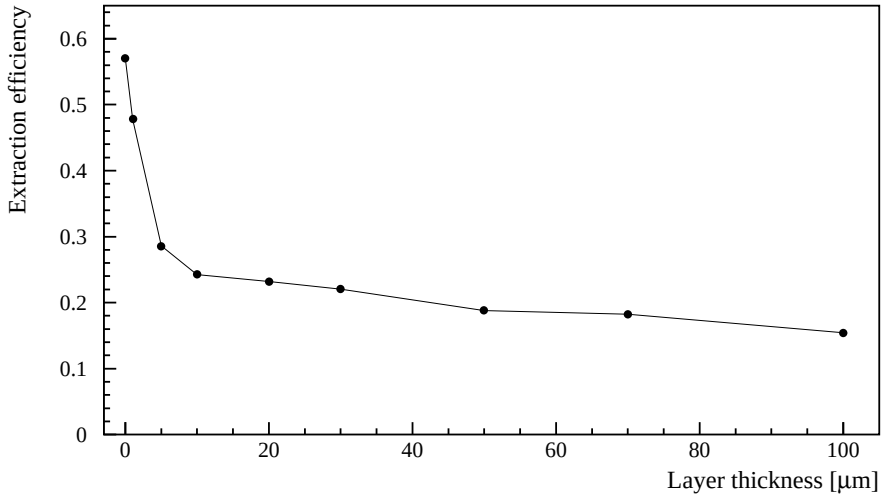

Figure 7.11: Simulated extraction efficiency plotted against inefficient-layer thickness.

It has to be also noted that in the simulation model a 'perfect' crystal (although the inefficient layer is included) and a 'perfect' (completely linear) accelerator are used. In reality, in the operation of the accelerator, there are unwanted imperfections such as power supply ripple in the bending and focusing magnets, residual nonlinearities, etc. that affect the beam behaviour. The effects are difficult to measure and include in the simulations, but they have an effect that in most cases would decrease the extraction efficiency.

The agreement between simulation and measurement results is best if the simulations are made in such a way that the particles are extracted through multi-pass extraction. The initial impact parameter distribution used in the simulations is shown in Fig. 6.1. This distribution, obtained with a large kick strength compared with what is used in the experiments (cf. Section 5.3.2), extends up to 10 μm. To make the simulations in the multi-pass mode, a surface-layer thickness of 10 μm was used to obtain the results presented in this section.

7.4.2 Angular scans

An angular scan can be simulated by varying the crystal angle in the simulation program, running the full simulation for each crystal angle and recording the resulting extraction efficiency. A simulated angular scan is shown in Fig. 7.12. The FWHM of the scan is about 50 μrad, somewhat narrower than the narrowest measured angular scans, which have a width of about 70 μrad.

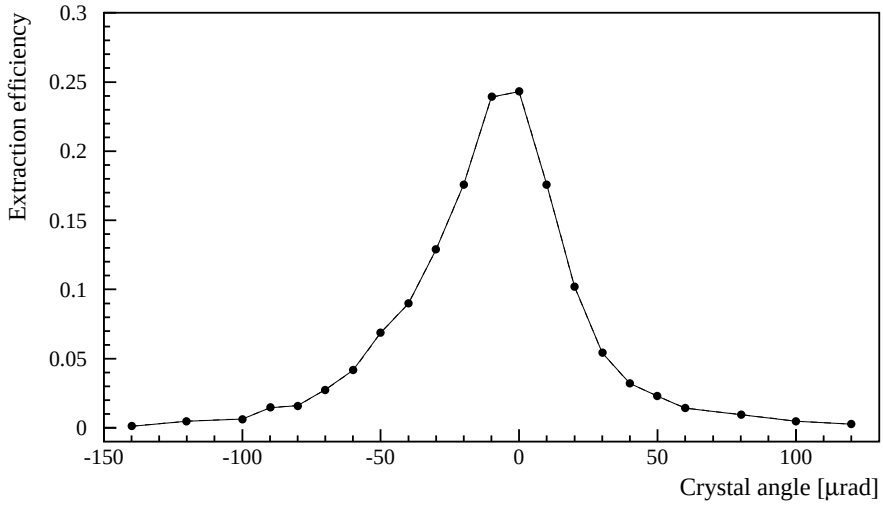

Figure 7.12: Simulated angular scan

7.4.3 Extracted beam profiles

Simulated extracted beam profiles are shown in Fig. 7.13. The RMS widths of the horizontal and vertical profiles are 0.66 mm and 2.4 mm, respectively. These RMS widths are obtained after background subtraction using 1 mm bin width to make them comparable with the hodoscope profile widths where the scintillator thickness is 1 mm. The profiles are shown as they would appear at the hodoscope location, i.e. the particles are transported through all the material in the extracted beam line. The size of the horizontal profile is determined by the size of the beam coming out of the crystal, and by scattering in the extracted beam line. In the horizontal plane, the channeled particles leave the crystal within the critical channeling angle. Therefore, the width of the horizontal profile does not depend much on multiple passes and scattering in the crystal. The situation is different for the vertical profile because in the vertical plane there is no limitation imposed by the critical angle, and all the scattering during multiple passes in the crystal can increase the size of the vertical profile. The scattering

in the extracted beam line naturally increases the size and divergence of the extracted beam by the same amount in both horizontal and vertical planes.

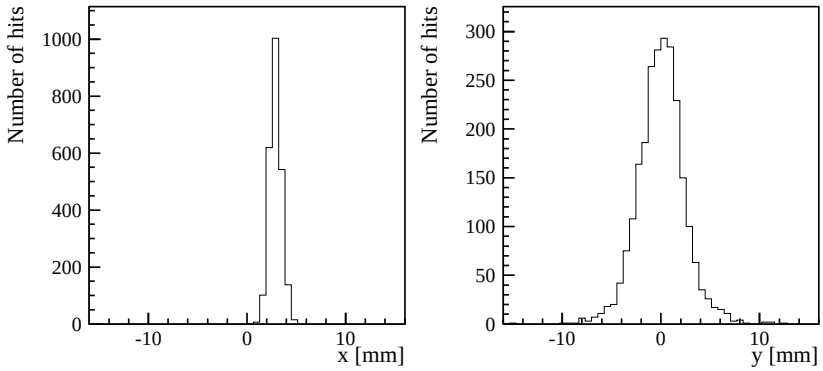

Figure 7.13: Simulated horizontal and vertical extracted beam profiles.

The simulated divergences of the extracted beam are shown in Fig. 7.14. The RMS divergences of the horizontal and vertical beams at the location of the hodoscope are 52 μrad and 79 μrad, respectively.

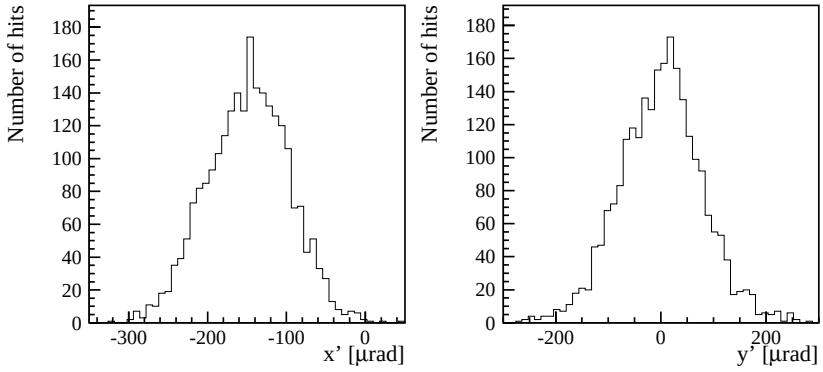

Figure 7.14: Simulated horizontal and vertical divergence of the extracted beam at the hodoscope location.

The vertical profile widths for a simulated angular scan are shown in Fig. 7.15. The width of the vertical profile changes as a function of the crystal angle so that the narrowest profiles are obtained when the crystal is well aligned with the incoming beam. Similar behaviour of the vertical profile width has been observed during experiments

(cf. Fig. 7.8). Also the simulated divergence of the vertical profile changes so that the smallest divergences are found at good crystal alignment.

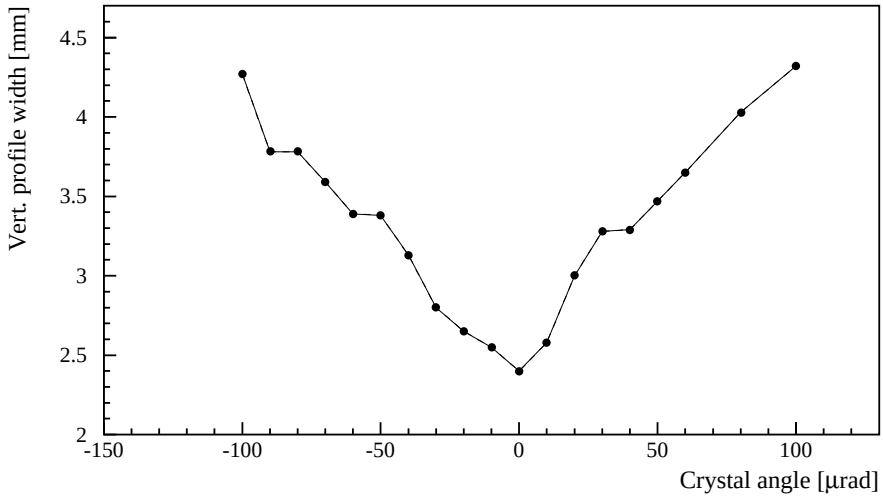

Figure 7.15: Simulated vertical profile RMS widths as a function of crystal angle.

The reason for the changing width of the vertical profiles can be seen in Fig. 7.16, which shows how many hits in the crystal are needed on average before the particles are extracted. For a well-aligned crystal, the number of hits needed is smaller than when the crystal is not well aligned with the incoming beam. The number of hits in the crystal is proportional to the integrated multiple scattering that the particles experience before extraction. The integrated multiple scattering in the crystal determines the vertical size and divergence of the extracted beam at the crystal location. The width of the vertical profile at the hodoscope location, i.e. the quantity that can be measured, depends on both the size and divergence of the extracted beam when it exits the crystal.

The divergence of the extracted beam in the horizontal plane is limited by the critical channeling angle, and therefore the width of the horizontal profile does not change in the same way as the vertical profile width changes.

7.4.4 General functioning of the simulation

The simulations are typically made with 10 000 or 100 000 protons randomly chosen from the initial impact parameter distribution. The number of particles kept in the simulation as a function of the number of hits made in the crystal is shown in Fig. 7.17. In the simulation, started with 10 000 protons, the number of protons left decreases, but there are still some protons left after nine hits in the crystal. The number of protons channeled is shown by the solid line in Fig. 7.17. During the first hit, channeling is not

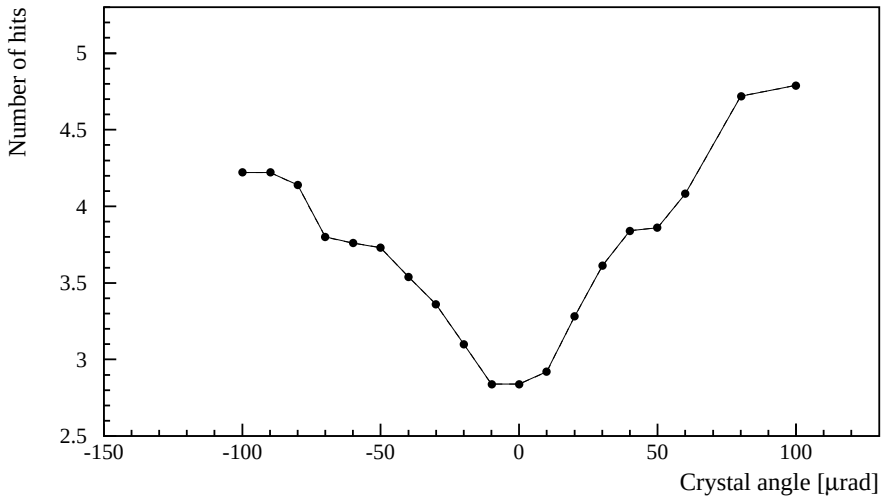

Figure 7.16: Number of hits in the crystal before extraction for a simulated angular scan.

possible because of the surface layer. Most protons are channeled during the second, third and fourth hits because their angular divergence is not too large compared with the critical channeling angle. For the fifth and later hits, protons are still channeled but the probability of channeling is lower because of the increased angular divergence. On average, the protons hit the crystal about three times.

The different mechanisms through which the protons can be lost were explained in Section 6.3.4. The contribution of the different loss mechanisms is shown in Table 7.5. Most of the protons are lost from the simulation because their horizontal amplitude at the crystal location is larger than the crystal external-edge position. Nuclear interactions and energy losses are further important reasons for losses. Only a few protons are lost because of the number of turns or because of an aperture limitation other than the crystal.

There are several reasons why the protons incident on the crystal may not be channeled and extracted. The protons may hit the inefficient surface layer, have an impact angle larger than the critical channeling angle, be dechanneled in the crystal, or be prevented from entering the crystal in channeling mode because of surface transmission. The contributions of these different mechanisms that can prevent extraction are shown in Table 7.6 for a typical simulation. For the first hit in the crystal, most protons hit the surface layer. For the second and later hits, the most important reason for not channeling is the large impact angle. For the protons that hit the good part (not the surface layer) of the crystal within the critical angle, surface transmission and dechanneling are both significant factors preventing extraction.

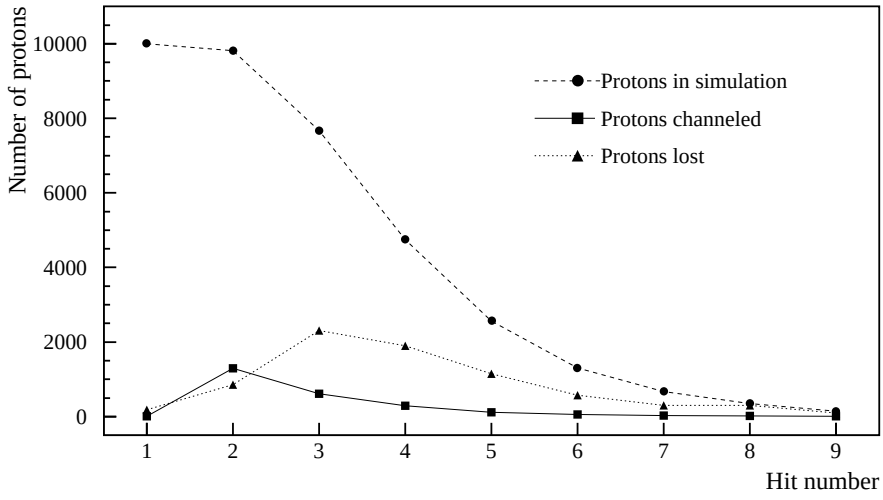

Figure 7.17: Number of protons left in the simulation, number of protons channeled (and extracted) and number of protons lost for each hit in the crystal. The simulation was started with 10 000 protons, and the figure shows that some of them hit the crystal up to nine times.

Table 7.5: Contribution of different proton loss mechanisms.

Loss mechanism	Contribution
Amplitude at crystal	77.6%
Nuclear interaction	17.4%
Energy loss	4.4%
Number of turns	0.1%
Betatron oscillation amplitude (horiz.)	0.5%

Table 7.6: Contribution of different mechanisms due to which particles that hit the crystal are not channeled and extracted successfully.

Reason	Contribution **120 GeV**	Contribution 14 GeV	Contribution 270 GeV
Impact angle larger than critical angle	61.3%	37.1%	61.7%
Surface transmission due to position	9.1%	11.7%	8.7%
Surface transmission due to angle	7.6%	7.1%	7.3%
Dechanneling in the crystal	22.0%	44.1%	22.3%

7.5 Energy dependence of beam extraction with a crystal

Beam extraction with a bent crystal depends on parameters that change as a function of beam energy. Beam diffusion and the resulting impact parameters and angles depend on the beam energy and on the excitation that is used to make the beam particles hit the crystal. When the particles enter the crystal, their interactions are energy dependent. Multiple scattering angles, critical channeling angle, dechanneling fraction and dechanneling length in straight and bent parts of the crystal change as a function of beam energy. Consequently, the extraction efficiency for a given extraction set-up depends strongly on the energy of the particles.

The experiment at the SPS was designed to study extraction at a beam energy of 120 GeV. For this reason, crystal parameters such as length and bending radius were originally optimized for this energy.

All of the experimental results shown up to this point were obtained at 120 GeV. In order to study energy dependence of crystal extraction, experiments were carried out at two new beam energies: 14 GeV and 270 GeV. The new energies were chosen to cover as wide an energy range as possible in the SPS. By performing experiments at 14 GeV and 270 GeV the lowest and highest energies for which a coasting beam can be stored in the SPS are exploited, and a large energy range, with a factor of almost twenty between highest and lowest energies, is obtained. At both of the new beam energies a beam could be extracted with a good signal-to-background ratio and extraction efficiencies, extracted beam sizes and angular scan widths could be measured.

Information about the preparation of the SPS for the different beam energies can be found in Ref. [90].

The results obtained at 120 GeV are shown in previous sections. In this section, results obtained at 14 GeV and 270 GeV are presented and a comparison of the results at the three different energies is made.

7.5.1 Beam excitation at different energies

When the circulating beam is excited with transverse noise, the emittance growth and the resulting impact parameters depend on the kick strength and on the beam energy. The emittance growth rate is given by Eq. (5.4). The emittance growth for a given kick strength is inversely proportional to the square of the beam energy.

In the experiments at the SPS, in the energy range used it was possible to adjust the voltage between the deflector plates so that the desired beam lifetime could be obtained. During measurements at 14 GeV, there was enough natural diffusion for additional beam excitation with noise not to be necessary.

7.5.2 Measurements at 14 GeV

During the measurements at 14 GeV, the SPS beam lifetime was typically between 0.1 and 2 hours when the crystal was in the beam halo and 4 hours without the crystal. These lifetimes are much lower than during experiments at other energies when the lifetime without a crystal was usually more than 100 hours.

In the efficiency measurements at 14 GeV a correction has to be made because of low lifetimes without a crystal in the beam. At other energies the extraction efficiency is defined according to Eq. (4.1) assuming an infinite lifetime without a crystal. At 14 GeV, the SPS beam lifetime τ is calculated using the lifetime due to crystal τ_{crystal} and the lifetime due to other loss mechanisms τ_{loss}:

$$\frac{1}{\tau} = \frac{1}{\tau_{\mathrm{loss}}} + \frac{1}{\tau_{\mathrm{crystal}}}. \tag{7.1}$$

The lifetime without crystal τ_{loss} is measured by taking the crystal out after each efficiency measurement. The lifetime due to crystal can then be calculated from Eq. (7.1). The (corrected) extraction efficiency at 14 GeV is obtained from Eq. (4.1) where the loss rate is calculated by using τ_{crystal}.

Extraction efficiency measurements made at 14 GeV are shown in Table 7.7. In the calculation of the extraction efficiency the low beam lifetime without a crystal is taken into account. The error in the efficiency is larger than at other energies because of additional uncertainties related to the lifetime correction. The efficiencies at 14 GeV are clearly lower than the efficiencies at 120 GeV which were typically close to 15% in similar conditions. The background fractions in the extracted beam are larger than at 120 GeV.

Table 7.7: Extraction efficiency measurements at 14 GeV. The last column shows the corrected extraction efficiency (see text).

Crystal	SPS intensity [10^{11} p]	Lifetime [hours]	Extr. rate [10^5 counts/s]	Background [%]	Extr. efficiency [%]
GR2	0.76	0.7 ± 0.1	0.67 ± 0.05	11.3	0.25 ± 0.12
GR5	0.31	0.7 ± 0.1	0.60 ± 0.04	5.3	0.55 ± 0.30
GR2	0.29	0.2 ± 0.1	1.24 ± 0.03	10.5	0.38 ± 0.17

Extracted beam profiles measured at 14 GeV are shown in Fig. 7.18. Owing to the larger multiple scattering angles at the lower beam energy, the profiles are clearly wider than at 120 GeV. The RMS widths of the horizontal and vertical profiles are 5.4 mm and 6.3 mm, respectively. These values are obtained after background subtraction.

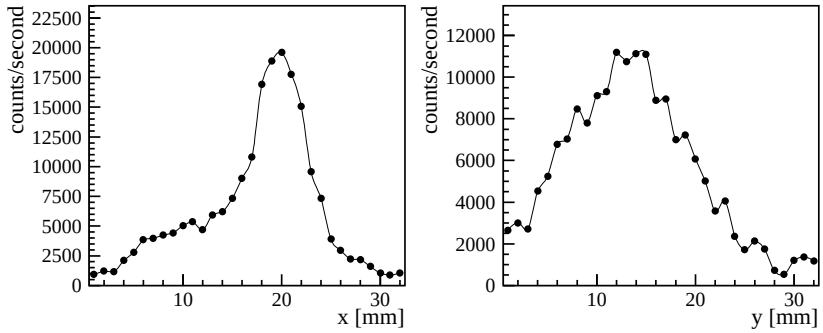

Figure 7.18: Horizontal and vertical extracted beam profiles at 14 GeV.

Simulated extracted beam profiles are shown in Fig. 7.19. The RMS widths of the simulated horizontal and vertical profiles are 4.2 mm and 6.0 mm, respectively. Also the simulated profiles are wider than the profiles at 120 GeV, and comparable with the measured profiles.

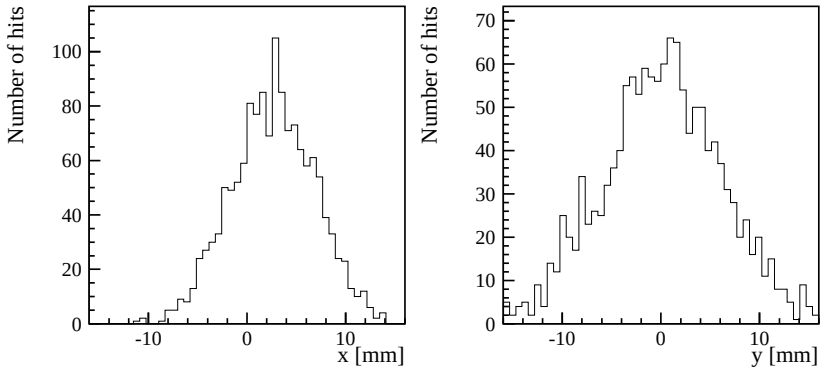

Figure 7.19: Simulated horizontal and vertical extracted beam profiles at 14 GeV.

An example of an angular scan at 14 GeV and the vertical profile width during the scan are shown in Fig. 7.20. The width (FWHM) of this scan is about 90 μrad. The widths shown are obtained by calculating the RMS width of the vertical profiles using all the 32 hodoscope strips and therefore cannot be directly compared with the widths where background has been subtracted. Because of the low beam lifetime, the SPS beam intensity changed by such a large factor (about 1.4) during the scan that a correction was applied to the shown extracted beam intensity to account for the intensity loss.

During the angular scan, fluctuations can be seen in the extracted beam intensity. These fluctuations are less visible in the width of the vertical profile. The change of vertical profile width is clearly visible (cf. Section 7.3.2).

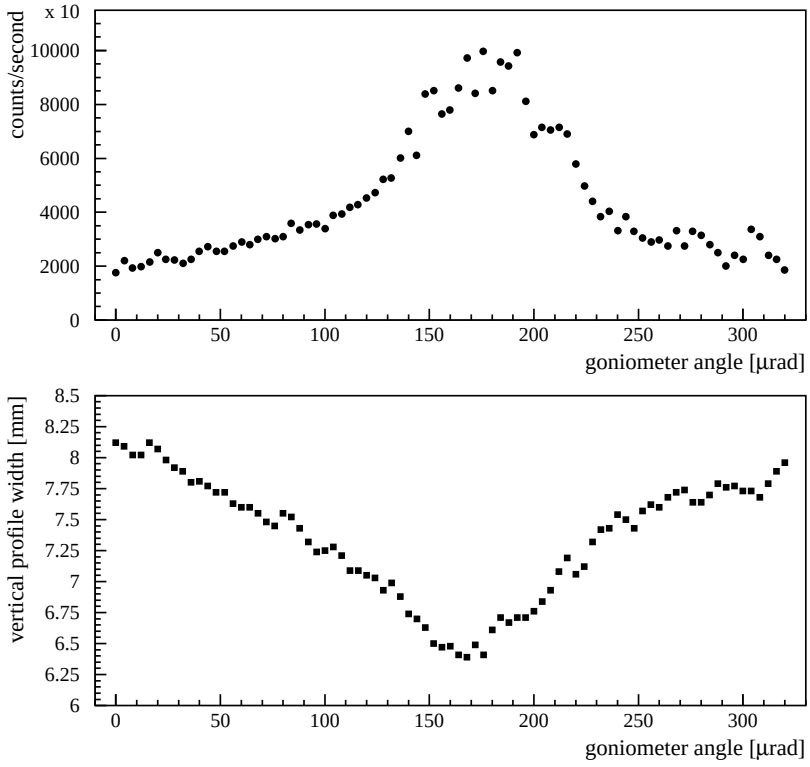

Figure 7.20: Angular scan and vertical profile width during the scan at 14 GeV.

7.5.3 Measurements at 270 GeV

Extraction efficiency measurements made at 270 GeV are shown in Table 7.8. The efficiencies are higher than those measured at lower energies, reaching values up to 18.6%. The background in the extracted beam is lower than at 14 GeV, and similar to the values measured at 120 GeV. The difference in background values shown in Tables 7.3 and 7.8 cannot be regarded as significant because the background levels depend on the beam conditions during the measurements.

Extracted beam profiles recorded at 270 GeV are shown in Fig. 7.21. Owing to smaller multiple scattering angles, the profiles are narrower than those measured at lower energies. The RMS widths of the horizontal and vertical profiles are 0.54 mm and 1.8 mm, respectively. These values are obtained after background subtraction.

Table 7.8: Extraction efficiency measurements at 270 GeV.

Crystal	SPS intensity [10^{11} p]	Lifetime [hours]	Extraction rate [10^5 counts/s]	Background [%]	Extr. efficiency [%]
GR2	3.3	20 ± 2	7.28 ± 0.07	2.4	16.0 ± 1.7
GR5	3.1	11 ± 1	1.04 ± 0.07	2.3	13.6 ± 1.5
GR5	2.5	17 ± 2	6.84 ± 0.09	1.7	16.0 ± 2.0
GR5	2.5	20 ± 3	6.58 ± 0.08	1.7	18.6 ± 2.7

Simulated extracted beam profiles are shown in Fig. 7.22. The RMS widths of the simulated horizontal and vertical profiles are 0.47 mm and 1.6 mm, respectively. The simulated profiles are slightly narrower but very well comparable with the measured ones.

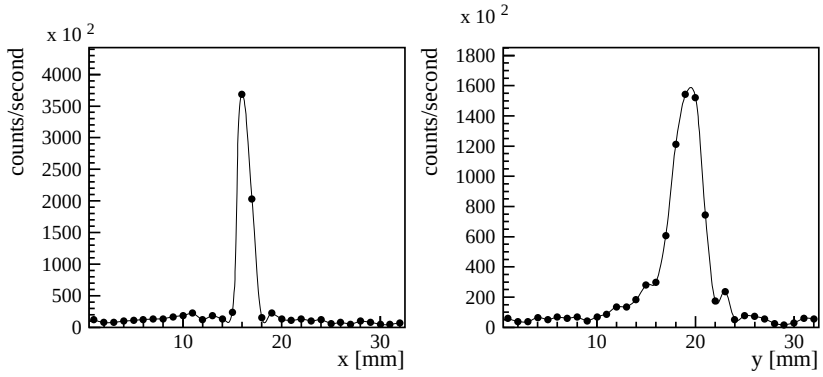

Figure 7.21: Extracted beam profiles at 270 GeV.

An example of an angular scan at 270 GeV and vertical profile width during the scan are shown in Fig. 7.23. The width (FWHM) of this particular scan is about 80 μrad. The widths shown are obtained by calculating the RMS width of the profiles using all the 32 hodoscope strips and therefore cannot be directly compared with the widths where background has been subtracted.

7.5.4 Comparison of results at different energies

Examples of angular scans measured at different energies are shown in Figs. 7.6, 7.20 and 7.23. The angular scans at each energy have different widths and shapes depending

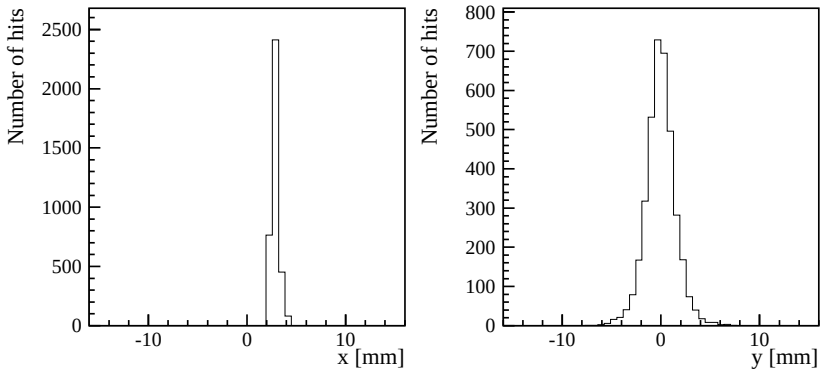

Figure 7.22: Simulated horizontal and vertical extracted beam profiles at 270 GeV.

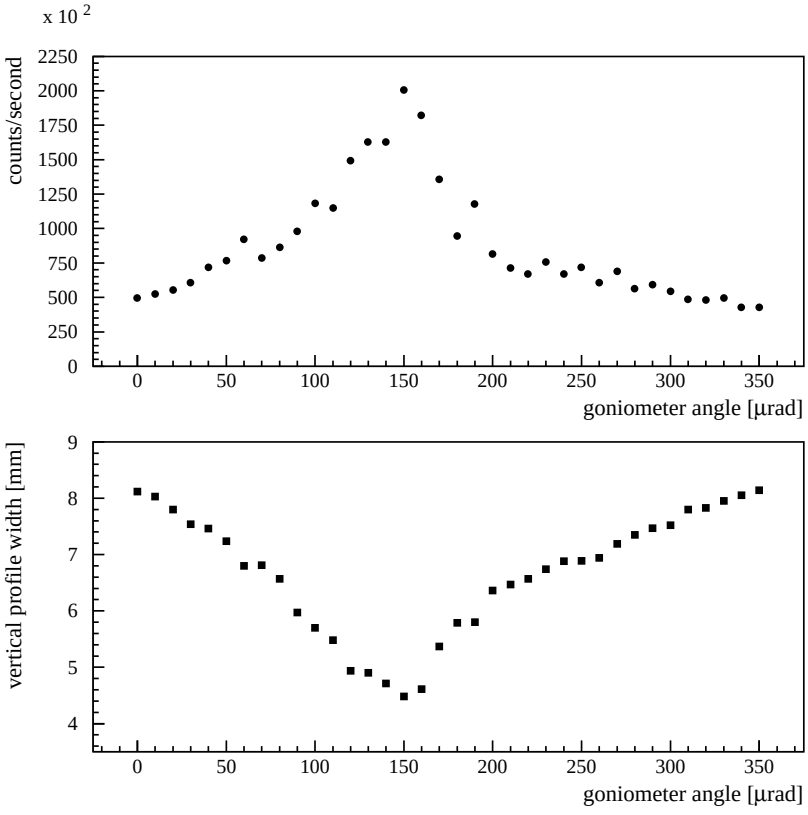

Figure 7.23: Angular scan and vertical profile width during the scan at 270 GeV.

on the exact experimental conditions during the time when the scan was made. At all the energies, the narrowest scan widths measured were about 70–80 μrad. At each

energy, scan widths up to 150 μrad were measured. Because of the large variation in the scan widths and shapes, a direct comparison of angular scan widths at different energies is not possible. However, at all three energies and in all beam conditions, angular scans can be performed, i.e. there are no problems aligning the crystal. The behaviour of the vertical profile width is also very consistent. In all cases, the vertical profile is narrowest when the crystal is well aligned.

The measured and simulated RMS widths for the horizontal and vertical extracted beam profiles at the three beam energies are shown in Table 7.9. The widths for simulated profiles are obtained using 1 mm bin width to make them comparable with the measured hodoscope profile widths where the scintillator thickness is 1 mm. The background in the measured profiles has been subtracted.

Table 7.9: Measured and simulated RMS widths for the horizontal and vertical extracted beam profiles.

SPS beam energy [GeV]	Measured horiz. width [mm]	Simulated horiz. width [mm]	Measured vert. width [mm]	Simulated vert. width [mm]
14	5.4 ± 0.4	4.2 ± 0.2	6.3 ± 0.4	6.0 ± 0.3
120	0.69 ± 0.20	0.66 ± 0.10	2.6 ± 0.3	2.4 ± 0.2
270	0.54 ± 0.20	0.47 ± 0.10	1.8 ± 0.3	1.6 ± 0.2

The measured profile widths, especially of the vertical profile, depend on the experimental conditions and therefore vary between different measurements. Nevertheless, a good agreement between the measured and simulated profile widths is found.

The highest extraction efficiencies measured at the three beam energies are shown in Table 7.10. The measured extraction efficiency is compared with the efficiency obtained from simulations (1 μm inefficient layer used). To show the energy dependence more clearly, the simulated values shown in Table 7.10 are normalized to the measured values at 120 GeV. Very good agreement is found between the measured and simulated energy dependence.

The main reasons why the efficiency at 14 GeV is much lower are multiple scattering and dechanneling. Because of large multiple scattering angles at low energy, the divergence of the beam incident on the crystal grows rapidly during multiple passes through the crystal. Furthermore, on average the particles make fewer passes through the crystal and therefore have smaller probability of being extracted. The dechanneling length at 14 GeV is much shorter than at higher energies, which also reduces the deflection and extraction efficiencies by a large factor.

The ('single-pass') deflection efficiencies are shown in Table 7.10 as well. The deflection efficiency is higher at 120 GeV than at 270 GeV, but in the case of extraction,

Table 7.10: Measured and simulated extraction efficiencies and calculated deflection efficiencies at three different beam energies. The simulated efficiencies, marked with an asterisk, are normalized to match the experimental value at 120 GeV.

SPS beam energy [GeV]	Extraction efficiency [%]	Simulated extr. efficiency [%]	Deflection efficiency [%]
14	0.55 ± 0.3	0.48^*	1.6
120	15.4 ± 2.2	15.4^*	31.8
270	18.6 ± 2.7	18.0^*	27.2

the efficiencies are higher at 270 GeV. This is due to the fact that at higher energy multiple scattering angles are smaller and more passes through the crystal are possible.

On the whole, the energy dependence of crystal assisted extraction is well understood from the computer simulations.

7.6 Beam excitation with nonlinearities

In order to obtain larger impact parameters than can be achieved with transverse noise excitation, and possibly to obtain a larger contribution from single-pass extraction, beam excitation with nonlinearities (see Section 5.3.3) has been tried. In this mode, strong nonlinearities are introduced in the accelerator by means of sextupole magnets and at the same time the tune is modulated with a quadrupole magnet. A similar mode of operation has been used to study the dynamic aperture in the SPS [94, 95].

In future superconducting accelerators such as the LHC, there will be unwanted nonlinear fields in the magnets and tune modulation will be caused by, for example, power supply ripple. By trying to re-create in the SPS the conditions in the superconducting accelerators, it is possible to study how crystal extraction would work in these accelerators.

A description of the experimental conditions can be found in Ref. [94]. During the experiments, the beam lifetime was very low, typically 0.5–2 hours. The measured beam lifetime did not change when the crystal was brought towards the beam, and therefore a measurement of the extraction efficiency was not possible.

During the measurements, crystal position and tune modulation depth were varied and several angular scans were performed [86]. One of the angular scans, measured when the crystal was 26 mm from the closed orbit, is shown in Fig. 7.24. This scan clearly shows three separate peaks. Some of the other angular scans also have more than one peak, and in some cases there appear to be overlapping peaks. The scan shown in Fig. 7.24 was repeated three times with different step sizes and the same structure with three peaks was always measured. When the crystal was moved to a different distance from the closed orbit, the number and position of the peaks changes, i.e. the shape of the angular scan became completely different [86].

A comparison between beam excitation with nonlinearities and beam excitation with transverse noise has been made [87]. For the comparison, the crystal was positioned at a large distance from the closed orbit (about 27 mm) and an angular scan was performed with nonlinear beam excitation. Afterwards the scan was repeated with transverse noise excitation. The first scan had more than one peak whereas the second had exactly one peak as measured before. This comparison demonstrates that the multiple peaks in angular scans are linked to the excitation with nonlinearities.

In addition to the angular scans, the vertical extracted beam profile also had a double peak at some crystal positions. An example of extracted beam profiles is shown in Fig. 7.25. The measurements with nonlinear beam excitation were carried out with U-shaped crystals, which means that the double peak in the vertical profile cannot be explained by anticlastic bending of the crystal.

Under the combined effect of strong nonlinearities and tune modulation, the motion of protons at large transverse amplitudes can be chaotic, and therefore it is difficult to obtain a detailed understanding of the results. The angular scans with multiple peaks may reflect the structure of the horizontal phase space of the SPS beam at large

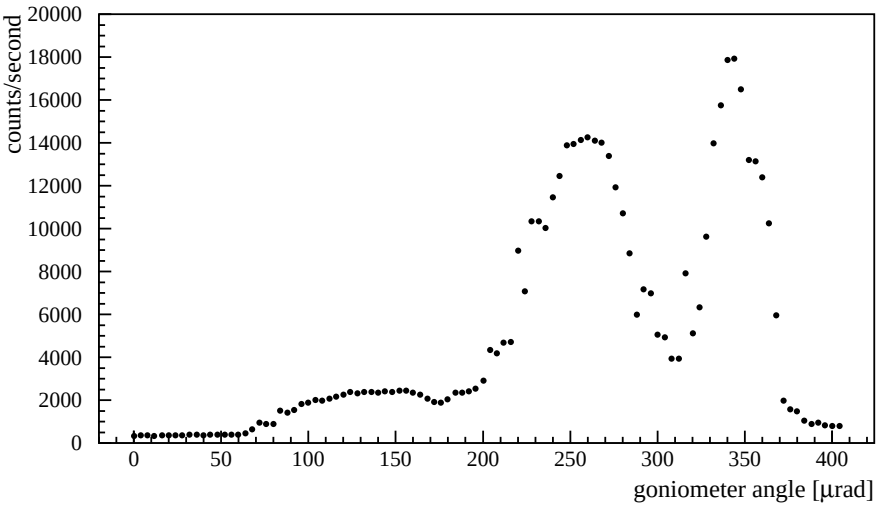

Figure 7.24: Angular scan measured when the SPS beam was excited with nonlinearities.

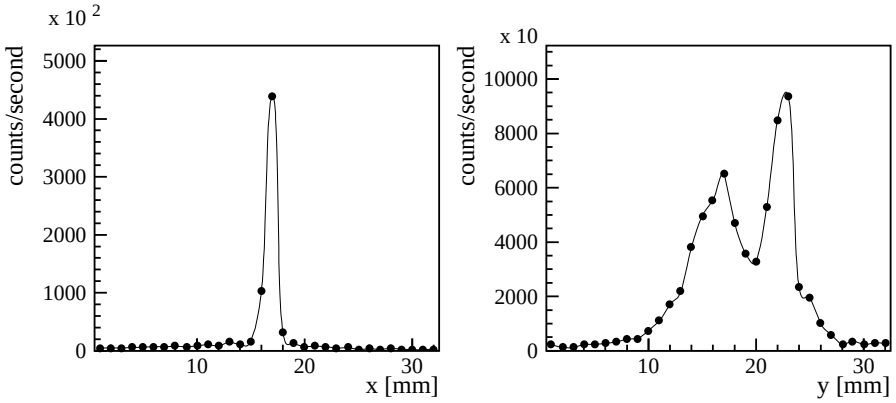

Figure 7.25: Horizontal and vertical extracted beam profiles measured when the SPS beam was excited with nonlinearities.

horizontal amplitudes.

Another reason for the multi-peak structure in the angular scans may be the multi-pass behaviour of the protons. Because of the nonlinearities, the diffusion speeds of the protons in the beam halo are high. Owing to fast diffusion, for each particle only a limited number of hits in the crystal, or turns in the accelerator after hitting the crystal for the first time, are possible before the particle is lost.

The impact angle distributions on the crystal (Fig. 6.3) can have many peaks especially for the second or the third hit in the crystal. Performing an angular scan corresponds to sliding an 'acceptance window' with a width of the critical channeling angle over the impact angle distribution. When the 'acceptance window' of a crystal has the same angle as a peak in the impact angle distribution, more particles are extracted, which causes a peak in the angular scan (i.e. in the recorded extracted beam intensity versus crystal angle). On the whole, if multi-pass extraction is limited to only few hits in the crystal or turns in the accelerator, the impact angle distribution may have a peak structure (cf. second and third hits in Fig. 6.3), which can be transferred into the shape of the angular scan.

The simulation of the extraction process under the conditions when the beam is excited with nonlinearities is not possible as reliably as it is with transverse noise excitation. Furthermore, it is difficult to estimate the extraction efficiency. However, it has been shown that with nonlinearities and tune modulation significant effects can be expected for beam extraction with a bent crystal. A possible application is the use of a beam extracted with a crystal to study the phase space structure of the circulating beam.

Chapter 8

Possible improvements and applications

In this chapter, as a possible improvement to the extraction experiment at the SPS and as another way of testing the extraction models, the dependence of extraction efficiency on the crystal length is demonstrated. After that, the possible application of crystal assisted extraction at the LHC is discussed.

8.1 Crystal length at the SPS

As already pointed out in Ref. [78], the extraction efficiency could be improved by changing the crystal length.

The simulated extraction efficiency is shown as a function of crystal length in Fig. 8.1. In this simulation, the crystal is assumed to have a uniform curvature over its whole length, i.e. there are no straight parts in the ends of the crystal. A value of 10 μm is used for the thickness of the inefficient surface layer, i.e. the simulation is done in a multi-pass mode. The simulation results show that with multi-pass extraction at 120 GeV the optimal crystal length is below 2 cm. As a comparison, the deflection efficiency is shown with a dashed line in Fig. 8.1. It can be seen that the highest extraction efficiency is obtained with a shorter crystal than the highest deflection efficiency. The reason for this is that with a shorter crystal, the nonchanneled particles experience smaller multiple scattering angles, and therefore can make more passes through the crystal. When the crystal length is 1.5 cm, the average number of hits in the crystal is almost four. The average number of hits decreases with the crystal length, and is about three with a 4-cm-long crystal. In addition to this, during second or later hits in the crystal the angular divergence of the particles is smaller with shorter crystals.

The crystal length at the SPS was originally optimized for single-pass extraction. Therefore, and also because of mechanical considerations related to crystal bending, 3-cm- and 4-cm-long crystals were prepared. In practice, the U-shaped crystals have legs, and with a bending angle of 8.5 mrad required at the SPS, it is no trivial matter to prepare a much shorter crystal.

The improvement in the simulated extraction efficiency due to a shorter crystal depends on parameters such as surface-layer thickness and crystal bending that are

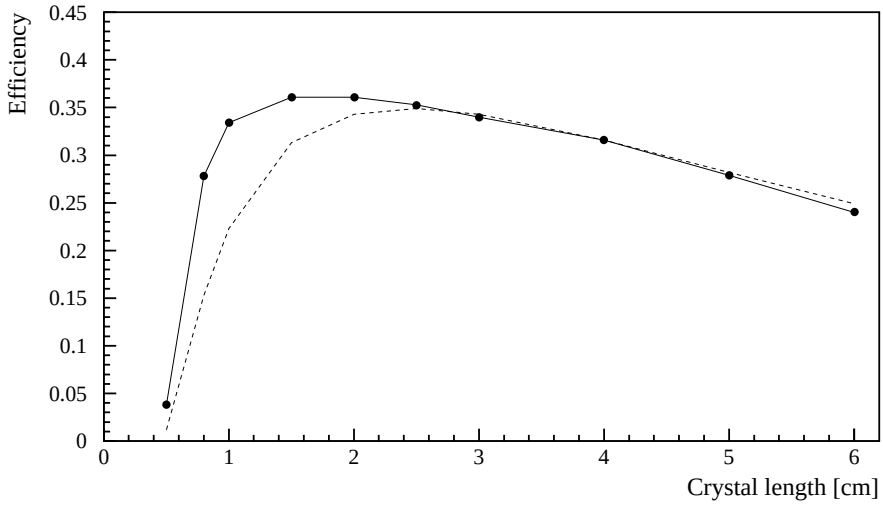

Figure 8.1: Simulated extraction efficiency as a function of crystal length (solid line). The dashed line shows the (single-pass) deflection efficiency.

used in the simulation. In the case shown in Fig. 8.1, the relative improvement is rather small, about 15% between 2-cm- and 4-cm-long crystals.

8.2 Large Hadron Collider

The subject of this thesis is crystal assisted extraction at the SPS. However, based on the experience gained in this experiment, a few general comments can be made regarding possible application of the method at the LHC.

One of the advantages at higher beam energy is the fact that the multiple Coulomb scattering angle is proportional to $1/E$ whereas the critical channeling angle is proportional to $1/\sqrt{E}$. At 120 GeV, the multiple scattering angle given by a 4-cm-long silicon crystal is about 72 μrad, and the critical angle ψ_{crit} is 14 μrad. At the LHC beam energy of 7 TeV, the multiple scattering angle is only 1.2 μrad and by using Eq. (3.9) the critical angle ψ_{crit} is 1.9 μrad. Therefore, at high energy the angular divergence of the beam grows more slowly compared with the critical angle during the multi-pass process than at low energy, and the extraction efficiency reduction due to scattering during multiple passes in the crystal is less severe.

The importance of multi-pass extraction has been demonstrated at the SPS (cf. Section 7.2). It is difficult to accurately estimate the initial impact parameters and angles that will be obtained at the LHC. The impact parameters are also dependent on the operating conditions of the machine. With multi-pass extraction, the initial

impact parameters are less crucial since the impact parameters for second and later hits are mainly determined by scattering in the crystal. Even with an inefficient surface layer, multi-pass extraction is expected to work. In addition, in multi-pass extraction mode it is possible to optimize crystal and accelerator parameters, such as the value of the β-function at the crystal location, to achieve a higher extraction efficiency (cf. Section 6.3.6).

At the LHC, a very efficient beam cleaning system is needed to protect the superconducting magnets from particle losses [1, 2]. A crystal positioned in the beam halo would have to be considered as the primary collimator of a multi-stage collimation scheme. With multi-pass extraction, the position of the secondary collimators will have to be optimized to allow multiple passes in the crystal and to ensure efficient collimation. The space required for multi-pass extraction, i.e. the smallest allowable distance of the secondary collimators from the beam centre, can be estimated by multi-pass simulation (cf. Section 6.3).

Based on the SPS results, enough information about the extraction process has been obtained so that, if required, the design of a crystal assisted extraction set-up for the LHC can be started.

Chapter 9

Summary and outlook

Extraction with a bent crystal seems to be the only feasible option for providing the possibility for a fixed-target facility at future high-energy hadron colliders such as the LHC. If the extraction set-up is carefully designed and integrated with the beam cleaning system, a crystal could be used in a parasitic mode, i.e. without disturbing the collider experiments and using only particles that would be lost otherwise.

In the studies of crystal assisted extraction at the SPS, significant progress has been made in the understanding of the extraction process. This thesis provides a comprehensive summary of the studies at the SPS, including theoretical background, general principles of crystal assisted extraction and presentation of both simulation and experimental results.

The experiments at the SPS were started using crystals bent in 'bridge'-type bending devices. Extraction was first observed in kick mode, but all subsequent measurements have been performed in diffusion mode. The most commonly used method of creating beam diffusion has been excitation with transverse noise. The first measurements gave unexpected results such as wide angular scans and double peaks in the extracted beam profiles. These results were due to the bending technique used, and therefore a new crystal design, the U-shaped crystal, was developed.

Most of the measurements have been made with U-shaped crystals. The improved bending technique eliminated the unwanted twist, and narrower angular scans (down to about 70 μrad) have been measured. At the usual beam energy of 120 GeV, extraction efficiencies of about 15% have been measured.

Different U-shaped crystals, modified to have an increased thickness or a known positive miscut angle, have been used. However, the results obtained with these crystals have not been significantly different from those obtained with the first U-shaped crystal.

The existence of multi-pass extraction has been demonstrated with a crystal that does not allow single-pass extraction. The results obtained with this crystal show that multi-pass extraction is very important for the extraction process. In multi-pass extraction, the initial impact parameters and exact operating conditions of an accelerator are less critical, and therefore it is possible to design a robust extraction set-up. With multi-pass extraction, it is also possible to optimize crystal and accelerator parameters in order to, for example, increase the extraction efficiency.

The energy dependence of crystal extraction has been studied by using three en-

ergies: 14 GeV, 120 GeV and 270 GeV. Extracted beam profiles, angular scans and extraction efficiencies could be measured at all these energies. The measured energy dependence of extraction efficiency is in very good agreement with the expectations.

It has been shown that the procedure for setting up extraction with a crystal is fast and easy, and once the extraction has been set up, an intensive beam can be provided to an external target. The stability of the position and intensity of the extracted beam has been very good for the duration of the measurements, i.e. up to several hours.

Improvements have been made with regard to crystal bending, installation and alignment techniques, and in this respect future extraction seems perfectly feasible.

A simulation model has been developed to describe the extraction process. The simulation reproduces well the qualitative features of the experimental results such as the behaviour of the vertical profile as a function of the crystal angle. The prediction of the exact quantitative values such as the extraction efficiency is more difficult since some of the parameters that affect the efficiency are not known precisely. By assuming that only multi-pass extraction is possible, a satisfactory agreement between simulation and experimental results can be achieved. The simulated energy dependence of extraction efficiency and of extracted beam profiles is in very good agreement with measurements.

After the long series of measurements performed with different crystals and with different beam excitation methods, a considerably increased understanding of the extraction process has been achieved.

Most of the measurements have been carried out with proton beams, but recently the possibility of extracting high-energy (22 TeV) fully stripped lead ions has been demonstrated with high efficiency. These results are not reported in this thesis, but they show that crystal assisted extraction is also possible at high-energy heavy-ion accelerators.

After the comprehensive studies of crystal assisted extraction at the SPS, the extraction of both protons and lead ions from the LHC seems feasible. The main issues with regard to the possible design of an extraction set-up are interface with the beam cleaning system and optimization of the extraction efficiency.

Bibliography

[1] LHC study group, Design study of the Large Hadron Collider (LHC), CERN 91-03, (CERN, Geneva, 1991).

[2] LHC study group, The Large Hadron Collider: conceptual design, CERN/AC/DI 95-05 (LHC), (CERN, Geneva, 1995).

[3] CMS collaboration, CMS technical proposal, CERN/LHCC 94-38, LHCC/P1, (CERN, Geneva, 1994).

[4] ATLAS collaboration, ATLAS technical proposal, CERN/LHCC 94-43, LHCC/P2, (CERN, Geneva, 1994).

[5] ALICE collaboration, ALICE technical proposal, CERN/LHCC 95-71, LHCC/P3, (CERN, Geneva, 1995).

[6] COBEX collaboration, Collider beauty experiment at the Large Hadron Collider at CERN: letter of intent, CERN/LHCC 93-50, LHCC/I6, (CERN, Geneva, 1993).

[7] GAJET collaboration, Study of CP violation in B-meson decays using an internal gas jet target at the LHC: letter of intent, CERN/LHCC 93-54, LHCC/I7, (CERN, Geneva, 1993).

[8] LHB collaboration, Measurement of CP violation in B meson decays with an extracted LHC beam: letter of intent, CERN/LHCC 93-45, LHCC/I5, (CERN, Geneva, 1993).

[9] RD22 collaboration, B.N. Jensen et al., A proposal to test beam extraction by bent crystal channeling at the SPS: a first step towards a LHC extracted beam, CERN/DRDC 91-25, DRDC/P29, (CERN, Geneva, 1991).

[10] LHC-B collaboration, LHC-B: Dedicated LHC collider beauty experiment for precision measurements of CP-violation: letter of intent, CERN/LHCC 95-5, LHCC/I8, (CERN, Geneva, 1995).

[11] J. Rossbach and P. Schmüser, Proc. Fifth General CERN Accelerator Physics Course in Jyväskylä, Finland, CERN 94-01, (CERN, Geneva, 1994).

[12] H. Wiedemann, Particle accelerator physics (Springer Verlag, Berlin, 1993).

[13] D.A. Edwards and M.J. Syphers, An introduction to the physics of high energy accelerators (Wiley-Interscience, New York, 1993).

[14] R.Q. Twiss and N.H. Frank, Rev. Sci. Instrum. **20** (1949) 1.

[15] E.D. Courant, M.S. Livingston and H.S. Snyder, Phys. Rev. **88** (1952) 1190.

[16] E.D. Courant and H.S. Snyder, Ann. Phys. **3** (1958) 1.

[17] S.P. Møller, CERN 94-05 (1994).

[18] H.H. Andersen, R.E. Carrigan and E. Uggerhøj (eds.), Channeling and other crystal effects at relativistic energy, Nucl. Instrum. Methods. **B119** (1996), topical issue.

[19] V. Biryukov, Y.A. Chesnokov and V.I. Kotov, Crystal channeling and its application at high-energy accelerators (Springer Verlag, Berlin, 1997).

[20] R.A. Carrigan jr. and J.A. Ellison (editors), Relativistic channeling, NATO ASI Vol. 165 (Plenum Press, New York, 1987).

[21] D.S. Gemmel, Revs. Mod. Phys. **46** (1974) 129.

[22] J. Stark, Physik. Zeitsch. **13** (1912) 973.

[23] G.R. Piercy, F. Brown, J.A. Davies and M. McCargo, Phys. Rev. Lett. **10** (1963) 399.

[24] M.T. Robinson and O.S. Oen, Phys. Rev. **132** (1963) 2385.

[25] J. Lindhard, Kgl. Danske Videnskap Selsk. Mat. Fys. Medd. 34, No. 14 (1965); Phys. Lett. **12** (1964) 126.

[26] P.A. Doyle and P.S. Turner, Acta Cryst. **A24** (1968) 390.

[27] J.S. Forster et al., Nucl. Phys. **B318** (1989) 301.

[28] V. Biryukov, V.I. Kotov and Yu.A. Chesnokov, Physics-Uspekhi **37** (1994) 937.

[29] E.N. Tsyganov, Fermilab reports TM-682, TM-684 (1976), unpublished.

[30] L. Gatignon (CERN, Geneva, Switzerland), Private communication.

[31] A. Elishev et al., Phys. Lett. **B88** (1979) 387.

[32] J. Bak et al., Phys. Lett. **B93** (1980) 505.

[33] S.P. Møller et al., Phys. Lett. **B256** (1991) 91.

[34] A. Baurichter et al., Nucl. Instrum. Methods **B119** (1996) 172.

[35] C. Biino et al., Phys. Lett. **B403** (1997) 163; CERN/SL 97-05 (EA).

[36] U. Mikkelsen, Experimental investigations of the interaction of multi-GeV particles and photons with strong crystalline fields in view of applications in high energy beamlines, Ph.D. thesis, University of Århus, Denmark (1997).

[37] C. Biino et al., The influence of radiation damage on the deflection high energy beams in bent silicon crystals, Proc. Fifth European Particle Accelerator Conference (1996); CERN/SL 96-30 (EA).

[38] B.S. Newberger, H.J. Shih and J.A. Ellison, Nucl. Instrum. Methods **A325** (1993) 9.

[39] W.E. Gabella, J. Rosenzweig, R. Kick and S. Peggs, Particle accelerators **42** (1993) 235.

[40] V.V. Avdeichikov et al., JINR Communications N1-84, Dubna (1984). English translation: Fermilab report 80/45 (1980), unpublished.

[41] A.A. Asseev et al., Nucl. Instrum. Methods **A309** (1991) 1.

[42] A.A. Asseev et al., Nucl. Instrum. Methods **A324** (1993) 31.

[43] C.T. Murphy et al., Nucl. Instrum. Methods **B119** (1996) 231.

[44] W. Herr, CERN/SL 92-53 (AP).

[45] W. Höfle and R. Louwerse (CERN, Geneva, Switzerland), Private communication.

[46] M.Gyr et al, Analysis and calibration of the noise voltage between the damper plates used for beam diffusion in the crystal extraction experiment, CERN/SL MD Note 176 (1995), unpublished.

[47] H.G. Hereward, CERN/MPS/DL 69-15 (1969).

[48] C. Sparks et al., Nucl. Instrum. Methods **A195** (1982) 73.

[49] M. Krisch et al., Nucl. Instrum. Methods **A308** (1991) 378.

[50] J. Klem and U. Mikkelsen, Study of the crystal surface and bending for the crystal extraction experiment, CERN/SL MD Note 171 (1995), unpublished.

[51] A. Freund (ESRF, Grenoble, France), Private communication.

[52] R. Hustache (ESRF, Grenoble, France), Private communication.

[53] A. Paul (ESRF, Grenoble, France), Private communication.

[54] B. Jensen and S.P. Møller, Laser system for crystal alignment and test (SPS extraction experiment), note attached to the 11th meeting on crystal extraction (CERN/SL/BT/Min/CE 92-11), unpublished.

[55] M. Gyr, CERN/SL Note 92-55 (BT).

[56] G. Ferioli (CERN, Geneva, Switzerland), Private communication.

[57] G. Fidecaro (CERN, Geneva, Switzerland), Private communication.

[58] G. Vuagnin, Measurement of the extraction efficiency of a proton beam from the SPS by means of a bent crystal, INFN-AE-94-09 (Thesis, Trieste University, 1994).

[59] J. Klem, Instrumentation for crystal extraction experiment at the CERN-SPS, Master's thesis, Helsinki University of Technology (1994).

[60] Bernd Vettermann, 2. Praxissemesterbericht (CERN, Geneva, 1992), unpublished.

[61] W. Herr and R. Schmidt, CERN/SPS 88-44 (AMS).

[62] W. Herr, CERN/SPS 88-43 (AMS).

[63] H. Akbari, J. Klem, R. Schmidt and B. Vettermann, Crystal extraction data acquisition (CERN, Geneva, 1994), unpublished.

[64] A. Burns et al., CERN/SL 90-68 (AP).

[65] I. Milstead, SPS BOSC System User Guide (CERN, Geneva, 1992), unpublished.

[66] H. Jakob (CERN, Geneva, Switzerland), Private communication.

[67] S. Bardin, CERN/SL Note 92-52 (AP)

[68] G. Vuagnin, CERN/SL Note 95-24 (AP).

[69] W. Herr, J. Klem and G. Vuagnin, Simulation of the Crystal Extraction Experiment at the CERN SPS, to be published.

[70] V. Biryukov, Phys. Rev. **E51** (1995) 3522.

[71] A.M. Taratin, Nucl. Instrum. Methods **B119** (1996) 156.

[72] S.A. Bogacz, D.B. Cline, S. Ramachandran, Nucl. Instrum. Methods **B111** (1996) 244.

[73] H. Grote, F.C. Iselin, CERN/SL 90-13 (AP).

[74] Particle Data Group, Phys. Rev. **D54** (1996), part I.

[75] M.Gyr, CERN/SL Note 93-72 (BT).

[76] RD22 collaboration, Status report on RD22: crystal extraction at the SPS, CERN/DRDC 92-51 (CERN, Geneva, 1992).

[77] S. Weisz and the RD22 collaboration, Proton extraction from the CERN SPS by a bent crystal, Proc. of the 1993 IEEE Particle Accelerator Conference, Washington D.C. (ISBN 0 7803-1203-1); CERN/SL 93-28 (DI).

[78] V. Biryukov, CERN/SL Note 93-78 (AP).

[79] H. Akbari et al., Phys. Lett. **B313** (1993) 491.

[80] E. M. Hansen (Tech. Univ. Lyngby, Denmark), Private communication.

[81] RD22 collaboration, Second status report on RD22: crystal extraction at the SPS, CERN/DRDC 94-11 (CERN, Geneva, 1994).

[82] K. Elsener and the RD22 collaboration, Results on proton extraction from the CERN-SPS with a bent crystal, Proc. Fourth European Particle Accelerator Conference, London, 1994 (ISBN 981-02-2991-7); CERN/SL 94-27 (DI).

[83] X. Altuna et al., Phys. Lett. **B357** (1995) 671; CERN/SL 95-41 (DI).

[84] Crystal extraction collaboration reported by J. Klem, Crystal extraction MD results, CERN/SL MD Note 170 (1995), unpublished.

[85] B. Dehning et al., Experimental evidence for multi-pass extraction with a bent crystal, Proc. 1995 IEEE Particle Accelerator Conference, Dallas; CERN/SL 95-36 AP.

[86] Crystal extraction collaboration reported by J. Klem, Crystal extraction results in 1995, CERN/SL MD Note 204 (1996), unpublished.

[87] Crystal extraction collaboration reported by J. Klem, Crystal extraction MD results in May and June 1996, CERN/SL MD Note 212 (1996), unpublished.

[88] K. Elsener et al., Nucl. Instrum. Methods **B119** (1996) 215; CERN/SL 95-88 (AP).

[89] Crystal extraction collaboration reported by J. Klem, Crystal extraction MD results, CERN/SL MD Note 223 (1996), unpublished.

[90] G. Arduini et al., Energy dependence of crystal assisted extraction at the CERN SPS, Proc. 1997 Particle Accelerator Conference, Vancouver; CERN/SL 97-31 (AP).

[91] G. Arduini et al., Extraction of 22 TeV/c lead ions from the CERN SPS using a bent silicon crystal, Proceedings of 1997 Particle Accelerator Conference in Vancouver; CERN/SL 97-36 (AP).

[92] K. Elsener, W. Herr and J. Klem, Proton and Pb ion beam extraction experiments with bent crystals at the CERN-SPS, Proceedings of the International Symposium on Near Beam Physics, Fermi National Laboratory (1997); CERN/SL 97-73 (EA).

[93] G. Arduini et al., Phys. Rev. Lett. **79**, No 21 (1997); CERN/SL 97-43 (DI).

[94] W. Fischer, "An experimental study on the long-term stability of particle motion in hadron storage rings", Ph.D. thesis, Hamburg University, Germany (1995); CERN SL/96-10 (AP).

[95] W. Fischer, M. Giovannozzi and F. Schmidt, Phys. Rev. **E55** (1997); CERN/SL 95-96 (AP).